

**Application and quality of X-Ray Fluorescence core scanning in
reconstructing late Pleistocene NW African continental margin
sedimentation patterns and paleoclimate variations**

Dissertation zur Erlangung des Doktorgrades am Fachbereich Geowissenschaften der
Universität Bremen

vorgelegt von
Rik Tjallingii
Bremen, Dezember 2006

Tag des Kolloquiums:

12.02.2007

Gutachter:

Prof Dr. G. Wefer
Prof Dr. R. Stein

Prüfer:

Prof. Dr. R. Henrich
Dr. T. Bickert

Acknowledgements

I owe many thanks to Prof. Dr. Gerold Wefer who gave me the opportunity to do this PhD project, and for all his support. Furthermore, Prof. Dr. Gerold Wefer and Prof. Dr. Rüdiger Stein are thanked for their compassion and effort evaluating this thesis.

I thank Dr. Torsten Bickert and Dr. Ursula Röhl in particular. I am very thankful for your supervision, scientific experiences, advices, and support that greatly improved this PhD project. Thank you both for the nice time.

Of course thank all my colleagues at the research center and the department of geosciences at the University of Bremen who directly or indirectly contributed to this work and the good working atmosphere. I thank Jan-Berend Stuu especially for all his support and motivation along the way. Also, Jens Grützner, Holger Kuhlmann, Thomas, Westerhold, Helge Meggers, Lydie Dupont, Thomas Felis, Stephan Mulitza, Oscar Romero, Enno Schefuß, Christian Winter, Martin Kölling, Matthias Zabel, Matthias Prange, Xavier Giraud are thanked for all the helpful discussions and suggestions. I enjoyed working with Heike Pflutschinger, Vera Lukies, Alex Wülbers, and Walter Hale, and thank them for all their support with scanners and cores. Hella Buschoff, Marco Klann, and Monica Segl are thanked for their support with all the laboratory work. I really enjoyed the participation of Meteor cruise M58-2 and M65-1, and like to thank their captain, crew, and participants.

It has been a very nice experience to meet so many inspiring people over the last years. It was a great pleasure for me to work with Martin Claussen, Jens Fohlmeister, and Alexandra Jahn. Also, I very much enjoyed and appreciated the co-operation with Maarten Prins. Helge Arz, Frank Lamy, and Jérôme Kaiser are thanked for their efforts to put things in perspective over a glass of beer.

I want to thank all my friends from Bremen that I met over the last years. Thank you for the nice time, the good company, and teaching me a more proper German. I thank Jérôme, Marius, and Xavier especially for their support with all my problems that did not regard scientific work.. Patri, thanks for the music! Cécile, ma cheri!

Natuurlijk maak ik van de gelegenheid gebruik om al mijn matties uit NL te bedanken omdat ze er altijd voor me zijn. Met name de leden 'van club der vernieling' en 'de possie' waren altijd weer instaat een avond in goede banen te leiden. Lukas, homies-4-life!

Ik heb erg genoten (en hoop dat nog vaker te doen) van de wekelijkse warme hap bij Jan-Berend, Meta, Mathilde, Britte, en Nynke. Dank jullie wel voor jullie gastvrijheid en alle gezelligheid!

Cor, Fred, Siets en Eric; bedankt voor alle ondersteuning en jullie interesse in mij en mijn werk. Jullie zijn de liefste!

Table of Contents

Abstract	7
1. Introduction	11
1.1 Late Pleistocene climate variations	11
1.2 Objectives and approach	14
1.3 Northwest African regional settings.....	17
1.3.1 Northwest African climate	17
1.3.2 Marine productivity and oceanography off Northwest Africa	21
2. Methods.....	27
2.1 X-ray fluorescence spectrometry	27
2.1.1 Principles of fluorescence spectrometry and XRF Core Scanners.....	27
2.1.2 Comparison of XRF Core Scanner I and II.....	34
2.1.3 Precision of XRF Core Scanner II.....	37
2.1.4 Influence of physical properties	38
2.1.5 Spectro Xepos EDPXRF analyzes	41
2.2 Grain size analysis and the End-Member Modeling Algorithm	42
2.3 Analyses of carbonate, organic carbon, opal, and terrigenous matter.....	43
2.4 Physical properties	44
2.5 Stable isotope stratigraphy	44
3. Manuscript # 1	47
Influence of the water content on X-ray fluorescence core scanning measurements in soft marine sediments	
<i>Rik Tjallingii, Ursula Röhl, Martin Kölling, and Torsten Bickert</i>	
4. Manuscript # 2	65
Sedimentation processes and marine productivity off Cape Blanc (NW Africa) during the last glacial-interglacial cycle	
<i>Rik Tjallingii, Jan-Berend Stuut, Torsten Bickert, Ursula Röhl, Maarten Prins</i>	
5. Manuscript # 3	87
Continental humidity in Northwest Africa on orbital and sub-orbital time scales	
<i>Rik Tjallingii, Martin Claussen, Jens Fohlmeister, Alexandra Jahn, Jan-Berend W. Stuut, Torsten Bickert, Frank Lamy, Ursula Röhl</i>	
6. Outlook and perspectives	101
References	105

Abstract

Paleoclimate records from ice-cores and marine and terrestrial sediments indicate abrupt climate changes during the last glacial-interglacial cycle known as Dansgaard-Oeschger (D-O) oscillations. Although, it is evident that these climate changes are most severe in the North Atlantic realm, the forcing of the D-O climate oscillations is still controversial. Low-latitude climate zones are thought to play a major role in the global moisture balance, but little is known about their potential to force high-latitude climate changes. Feedback mechanisms between ocean heat transport, atmospheric circulation, and low latitude vegetation changes are thought to play an important role in the amplification, continuation and possibly initiation of D-O climate oscillations. Since subtropical regions are influenced by both high- and low latitude climate variability, they are of great interest for providing possible answers to the role of high- and low-latitude climate variations.

The aim of this PHD thesis is to document and understand the causal relationship of millennial-scale changes in the eastern sub-tropical Atlantic realm. The study focuses on the improvement of X-ray fluorescence (XRF) core scanning measurements, which are a valuable tool for obtaining high-resolution sediment archive analyses in a non-destructive way. Additionally, special attention is paid to the role of bulk sediment chemical analyses as possible tools in a multi-proxy paleoceanographic reconstruction off Cape Blanc, Northwest Africa, during the last glacial-interglacial cycle. Finally, the geological climate records are compared with model simulation. The results of the presented PhD project are documented in three manuscripts. One of these manuscripts is accepted for publication in *Geochemistry, Geophysics, Geosystems* (Chapter 3), whereas the two others are to be submitted to *Paleoceanography* (Chapter 4), and *Nature* (Chapter 5).

The first manuscript (Chapter 3) deals with a thorough study after the quality of the XRF core scanner data that are operational at the MARUM institute, University of Bremen, and the potential disturbing effects of changing physical properties on XRF core scanner data. XRF core scanning is a widely accepted method to obtain high-resolution bulk chemical analyses directly at the split core sediment surface. The XRF core scanner analyses only the very upper sediment layer, which is much smaller compared to the large volume of homogenized sample material that is used for chemical analyses on discrete samples. The quality of XRF core scanner measurements depends on the hardware components of the XRF scanner, the sample material, and the quality of sample preparation. However, little is known about the effects of changing physical properties such as grain-size, density, and water content in the scanned sediment core on the quality of the XRF core scanner data. XRF measurements

of artificially made sediment samples with different grain-size fractions indicate that radiation dispersion effects are only minor for fine-grained sediments. In addition, the relatively small density variations in soft marine sediments seem to have only minor influence on the XRF measurements as well. However, comparison of XRF scanner measurements of dry powder samples and measurements performed at the split-core sediment surface of soft marine sediments in core GeoB7920 indicate strongly reduced element intensities for the lighter elements Al and Si. Cohesive and adhesive properties of water form a water film directly under the foil that covers the split core sediment cores during XRF analyses. The artificial water film directly under the foil affects the sample volume analyzed by the XRF core scanner and strongly reduces the element intensities of the lighter elements Al and Si that emit relatively weak fluorescence energies. Pooling of interstitial seawater directly under the foil is indicated by elevated Cl intensities of measurements taken at the split core surface. Therefore, the Cl intensities were used to estimate the water content in the sample volume analyzed by the XRF core scanner in order to correct for the intensity loss of the elements Al and Si. Application of the correction equations obtained from core GeoB7920 to other XRF data measured on various sediment cores off Northwest Africa, suggest that these functions can be used as a general correction model to compensate for the intensity loss of the light elements Al and Si due to water absorption effects.

The second manuscript (Chapter 4) describes the application of the end-member modeling algorithm of Weltje (1997) to terrigenous grain-size distributions of samples from sediment core GeoB7920. The end-member model distinguished a sand-sized end member, a silt-sized end member, and a mud-sized end member. These end members were interpreted as proximal eolian end member, distal eolian end member, and hemipelagic mud associated with river run off, respectively. Proportional variations of the sand-sized end member correlate with Zr-Rb ratios obtained with XRF core scanner measurements used to indicate paleo-wind strength that seems to be strongly related to the global ice volume. Although the region off Cape Blanc is strongly influenced by coastal upwelling, opal concentrations are relatively low in the sediments of core GeoB7920. In fact, the bulk sediment Si concentrations reflect predominantly quartz transported from the North African continent by the prevailing wind systems. Pale quartz grains are transported by the northeast trade winds from more regional coastal areas, whereas iron-stained quartz grains originate from the southern Sahara and the northern Sahel region. The terrigenous grain-size fraction, the Zr-Rb ratio, and the Si-Fe ratios indicate strongly enhanced atmospheric circulation and increased eolian input from coastal sources during the maxim glacial conditions of MIS 2 and MIS 4, and D-O stadial

events. However, marine productivity and upwelling intensities are low during MIS 2 and MIS 4, which is most likely related to increased zonality of the trade winds during maximum glacial conditions. D-O stadial events indicate enhanced coastal upwelling although marine productivity remains low, whereas D-O interstadial events indicate high marine productivity in combination with relatively weak coastal upwelling. Most likely, cold and relatively fresh water introduced by the eastern boundary current caused stratification of the surface waters off Northwest Africa, which prohibited open-ocean deep-mixing essential for the winter-bloom. Marine productivity off Cape Blanc changes only little during interglacials, although upwelling intensities are related with the position of the ITCZ and the strength of the African monsoon.

In chapter 5, it is discussed how variations of the hemipelagic end member can be used as an indicator of the continental hydrological balance. Variations of the hemipelagic end member increase with increasing river run off, or due to extension of the continental vegetation cover reducing the eolian input. Moreover, the paleo-continental hydrological-balance variations indicated by the proportional variations of the hemipelagic end member are highly coherent with global ocean-atmosphere-vegetation model simulations. The model data indicates that precessional forced variations of the low-latitude summer insolation causes strong variations in the strength of the African monsoon during interglacial conditions. However, the relatively humid conditions associated with glacial D-O interstadial events seem to be related to North Atlantic SSTs rather than insolation-forced variations of the African monsoon. Moreover, both the geological records and modeling results show strong aridification of the Northwest African continent associated to D-O stadial events and Heinrich ice-rafting events.

The results presented in this thesis provide evidence that sub-tropical Northwest African climate is highly sensible to both low-latitude and high-latitude climate changes. Additionally, they show that marine productivity and coastal upwelling in the region off Cape Blanc are closely related to surface trade-wind circulation and Atlantic Ocean surface circulation. Despite the highly regional character of upwelling areas the results reported here are consistent with other continental margin studies under direct influence of the Atlantic eastern boundary current system.

- 1. Introduction -

1.1 Late Pleistocene climate variations

Paleoclimate records obtained from ice-cores (Dansgaard, 1993; NGRIP-members, 2004; Petit et al., 1999) and marine sediment cores (Bond et al., 1992; Broecker et al., 1992; Heinrich, 1988b) of the last glacial-interglacial cycle (the past ~ 125 ka) demonstrate abrupt millennial-scale climate variations. These rapid climate variations, called Dansgaard-Oeschger (D-O) oscillations (Dansgaard et al., 1984) and Heinrich events (Heinrich, 1988b), are especially prominent in the North Atlantic realm. D-O cycles show abrupt temperature jumps at the Greenland ice surface of up to one-half of the glacial-interglacial temperature amplitude in a few decades (Figure 1) (Alley, 1998). D-O stadial conditions and Heinrich events are related to cold, dry, and windy conditions in the North Atlantic region, whereas D-O interstadial conditions are related to relatively mild and humid conditions over this region (Alley et al., 2003). Heinrich events are widespread ice-rafted debris layers found in marine sediments throughout the North Atlantic related to severe cold events (for a review see (Hemming, 2004)). The forcing of these events is still controversial and has been related to insolation forcing (Clemens, 2005; Heinrich, 1988a; McIntyre and Molino, 1996), binge-purge modes of large continental ice sheets (MacAyeal, 1995; MacAyeal, 1993) and solar variability (Bond et al., 1993; Bond et al., 2001) that may include stochastic resonance of coupled ocean-atmosphere system (Ganopolski and Rahmstorf, 2002).

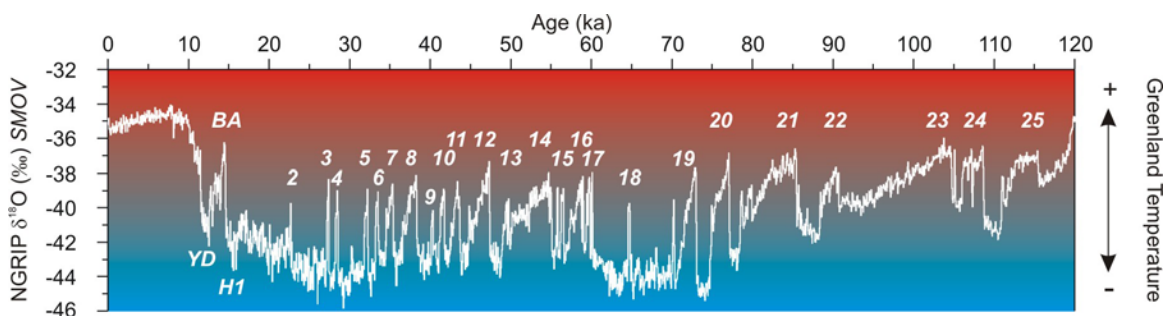


Figure 1. Stable isotope stratigraphy ($\delta^{18}\text{O}$) of the North Greenland Ice Core Project (NGRIP; 75.10 °N and 42.32 °W) which is directly related to the Greenland ice surface temperature (NGRIP-members, 2004). The numbers show the relatively warm D-O interstadial periods (Dansgaard, 1993). The Bølling-Allerød (BA) warm event and the Younger Dryas (YD) cold events are the last D-O like events during the last deglaciation.

Independent of their ultimate cause, D-O stadials and Heinrich events are associated with the discharge of melt water in the North Atlantic that strongly influenced the global thermohaline circulation. The global thermohaline circulation plays an important role in the

teleconnection between the northern and southern hemispheres and the global heat distribution (Broecker et al., 1985; Rahmstorf, 2002). At present, evaporation and cooling of relatively warm surface waters introduced in the North Atlantic by the Gulf Stream and the North Atlantic Drift cause down welling of North Atlantic Deep Water (NADW) (Figure 2a). NADW formation, and to a lesser extent formation of Antarctic Bottom Water (ABW) in the Southern Ocean, are the major driving forces of the global thermohaline circulation (Rahmstorf, 2002). Fresh water discharges in the North Atlantic linked to D-O stadials and Heinrich events lower the sea surface salinity (SSS) and subsequently cease the formation of NADW (Figure 2b). During these periods formation of AABW in the Southern Ocean becomes the major driving force of the thermohaline circulation, which reverses the thermohaline circulation and AABW fills the deep Atlantic basin from the South (Rahmstorf, 2002; Skinner et al., 2003). In addition, modeling studies show a reversed heat flux from tropical Atlantic towards the south (Knutti et al., 2004; Rahmstorf, 2002) causing extreme cooling of the North Atlantic (Bond et al., 1992). Subsequently, cold North Atlantic

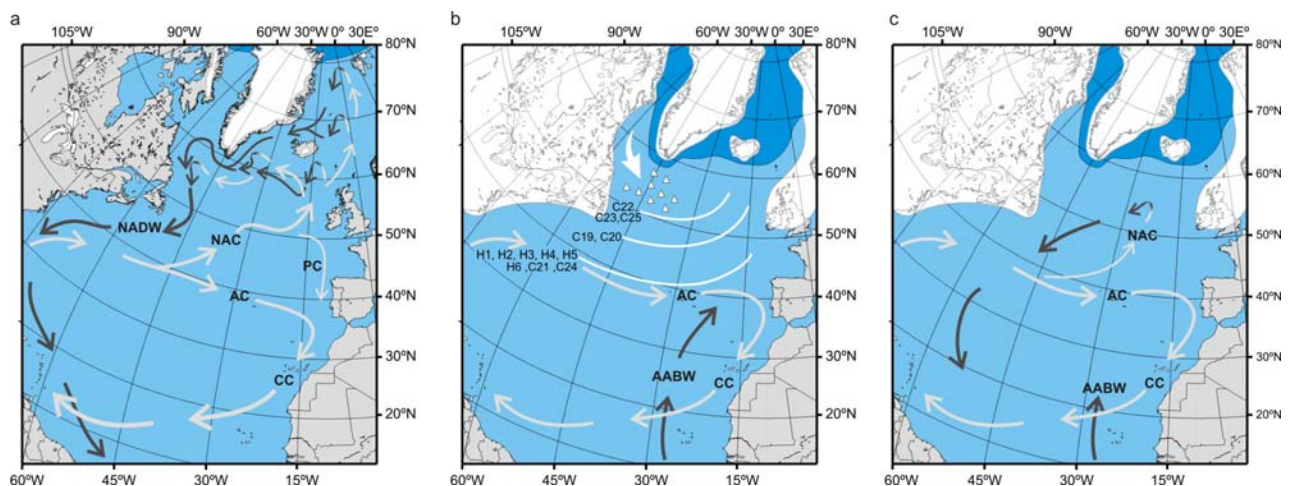


Figure 2. North Atlantic surface currents (light arrows), deepwater circulation (dark arrows), and the Northern Hemisphere ice cover. a) During interglacial conditions, the North Atlantic Current (NAC) transports warm and saline waters into the North Atlantic where it cools and forms North Atlantic Deep Water (NADW). The Azores Current (AC) forms the northern boundary of the subtropical Atlantic gyre that continues as the Canary Current (CC) whereas the Portugal Current (PC) forms the northern branch of the eastern boundary current. b) During glacial stadial and Heinrich events the formation of NADW is ceased and Antarctic Bottom Water (AABW) formed in the Southern Ocean fills the deep North Atlantic basin. Icebergs cover large parts of the North Atlantic as indicate by distinct ice rafting debris layers in marine sediments (white lines). c) During glacial stadials NADW formation initiated again but occurred in the North Atlantic open ocean reducing the influence of AABW in the Northern Atlantic Basin. The surface currents and deep circulation are modified after Rahmstorf (2002), Robinson et al. (1995), and Skinner et al. (2003), the glacial ice cover was redrawn after Clark and Mix (2002) and Peltier (1994), and the southern limits of ice-rafting events are indicated after Chapman and Maslin (1999) and Hemming (2000).

SST are transmitted by the Canary Current to the subtropical eastern Atlantic (Chapman et al., 2000; Pailler and Bard, 2002; Zhao et al., 1995) and the Mediterranean region (Cacho et al., 1999; Martrat et al., 2004). In addition, SST records from the western tropical and subtropical Atlantic suggest warmer and more saline surface water conditions during high-latitude D-O stadial and Heinrich events (Arz et al., 2001; Grimm et al., 1993; Schmidt et al., 2006). NADW formation partly restored during the much milder D-O interstadial conditions and occurred in the Atlantic open ocean south of Iceland (Rahmstorf, 2002) (Figure 2c). As a result of the relatively warm North Atlantic SSTs, the North Atlantic Westerlies carry moist air to Southern Europe and the Mediterranean Region resulting in relatively humid conditions (Allen et al., 1999; Moreno et al., 2005).

Although D-O events are most prominent in the North Atlantic, millennial-scale climate variations associated with D-O oscillations and Heinrich events are found in many paleoclimate archives all over the world (Leuschner and Sirocko, 2000; Voelker, 2002). Southern hemisphere climate records suggest relatively cold and windy conditions in combination with increased ice rafted sediments between 41°S and 53°S, during periods of active NADW formation in the Northern Hemisphere (Kanfoush et al., 2000; Kanfoush et al., 2002). Contrary, relatively warm SST in the south Atlantic (Little, 1997) correspond with Northern Hemisphere cold conditions prior and during Heinrich events. Such an asynchronous climate behavior between the Northern and Southern Hemisphere is similar to that found in the Greenland and Antarctic ice cores (Blunier, 1998; Blunier and Brook, 2001). Large-scale rearrangement of the global thermohaline circulation and inter-hemispheric heat distribution is a generally accepted explanation for global distribution of abrupt D-O climate changes (Knutti et al., 2004; Stocker and Wright, 1991). However, low-latitude paleoclimate records suggest that low-latitudes play a major role in millennial-scale oscillations as well (Dannenmann, 2003; Ivanochko et al., 2005; Peterson et al., 2000). Transmission, amplification, or event forcing of D-O climate variations by low-latitude mechanisms may include strong ocean-atmosphere feedbacks such equivalent to long-term El Niño-Southern oscillations (ENSO), shifts in the Inter Tropical Convergence Zone (ITCZ) or monsoon variability (Stott et al., 2002; Turney et al., 2004). In addition, variations of the atmospheric greenhouse gases (CO₂, CH₄, N₂O) are linked to tropical and subtropical vegetation changes and, hence, to the low latitude moist balance (Ivanochko et al., 2005; Ruddiman and Raymo, 2003; Stott et al., 2002). Detailed information of millennial-scale ocean-, atmosphere-, and continental climate variations at low-latitudes is crucial for better understanding of the underlying causes of rapid climate change and global climate dynamics.

1.2 Objectives and approach

The growing interest for millennial, centennial, decadal, and annual scale climate variations in paleoceanographic studies causes an increasing demand for high-resolution sediment analysis. Non-destructive X-ray Fluorescence Core Scanner measurements fulfill the present demand for high-resolution sediment archive analyses directly from the split core sediment surface, which enables fast analyses of the chemical sediment composition. Although XRF core scanner data are already widely accepted in paleoceanographic studies, there is little known about the influence down-core variation physical parameters on the XRF scanner data, such as density or water content. The first objective of this study concerns the quality of XRF Core Scanner data, to indicate which physical properties influence XRF Core Scanner data, and to correct for these influences. The second objective of this study is to compare and apply geochemical and sedimentological sediment analyses to reconstruct Late Pleistocene sedimentation patterns in the sub-tropical region off Northwest Africa. Additionally, this study focuses on the associated links and feedbacks between ocean, atmosphere, and continental climate as a result of high- and low-latitude climate forcing by comparison of geological proxy data and model simulations.

Five sediment cores GeoB4216-1, GeoB7919-5, GeoB7920, GeoB8630-9, and GeoB8509-2 (Figure 3) from the region off Northwest Africa that cover various deep-sea sediment lithologies were used for XRF Core Scanner study. The scanner analytical precision of the XRF core scanner was indicated by scanner data of cores GeoB7919-5, GeoB7920, GeoB8509-2, and GeoB8630-9. Sediment cores GeoB7919-5, GeoB7920, and GeoB8630-9 form a distal-to-proximal transect over the slope off Cape Blanc and contain increasing amounts and coarser terrigenous matter respectively. Sediment core GeoB8509-2 contains numerous turbidite sequences and pelagic sediment intervals that reflect a mixture of both deep and shallow marine sediment with different chemical compositions and physical properties. Sediment cores GeoB4216-1 and GeoB7919-5 were analyzed with two different types of XRF core scanners in order to compare the two scanners. These two cores contain quite different sediment compositions, which are considered typical deep marine sediments in the regions of recovery (Figure 3). XRF measurements on split core sediments and dry powder sediments of sediment core GeoB7920 were used to quantify and correct for the major influence of physical properties on XRF core scanner data. The correction functions defined for core GeoB7920 were applied on sediment cores GeoB7919-5 and GeoB8630-9 located off Cape Blanc as well.

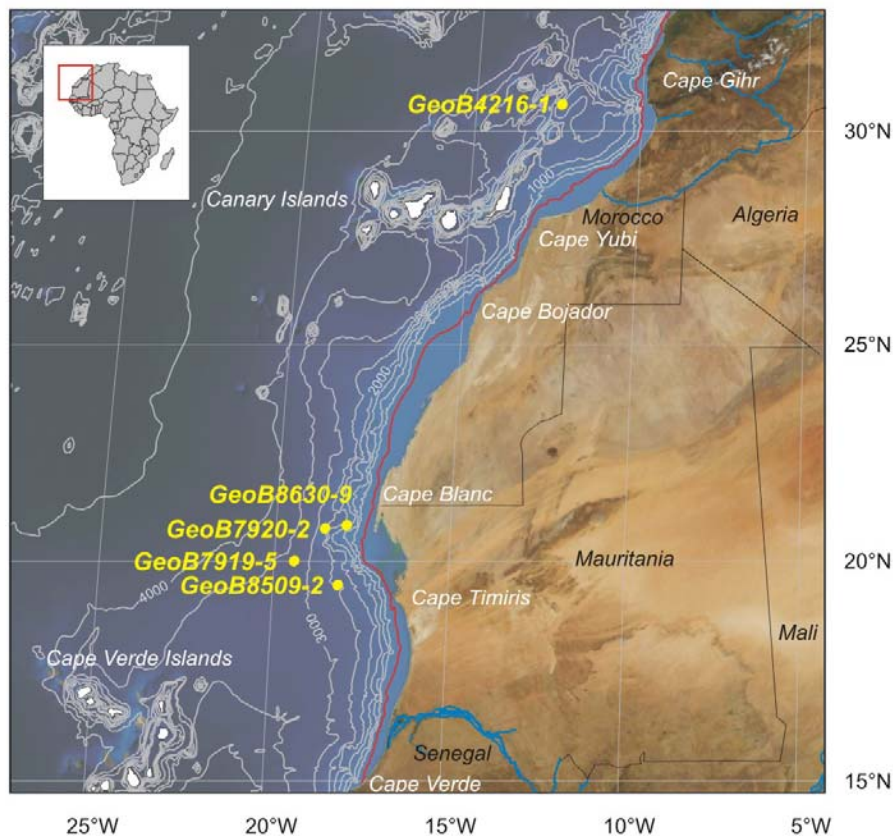


Figure 3 Map of study area and core locations. The red bathymetry line (100 m depth) indicates the coastline during the Last Glacial Maximum.

The paleoceanographic study focuses on sediment core GeoB7920 (20.45 °N, 18.35 °W, 2278m water depth) located off Cape Blanc (Figure 3). High marine productivity as a result of coastal upwelling, high supply of eolian dust from the adjacent African continent, and its location with respect to the ITCZ and the ocean surface circulation make the region off Cape Blanc ideally situated to study ocean, atmosphere, and continent variations. We used a multi proxy approach of detailed XRF core scanning measurements, organic carbon and opal analyses, grain-size analyses of the terrigenous fraction, and stable isotope stratigraphy to reconstruction of the late Pleistocene climate variations on and off the Northwestern African continent. These reconstructions provide new and valuable information about the role of subtropical regions during the last glacial interglacial cycle.

The results of this study are presented in the three following manuscripts:

Rik Tjallingii, Ursula Röhl, Martin Kölling, and Torsten Bickert: “Influence of the water content on X-ray fluorescence core scanning measurements in soft marine sediments.”
Published in *Geochemistry, Geophysics, Geosystems*

Rik Tjallingii, Jan-Berend Stuut, Torsten Bickert, Ursula Röhl, and Maarten Prins :

“Sedimentation processes and marine productivity off Cape Blanc (NW Africa) during the last glacial-interglacial cycle.“

To be submitted to *Paleoceanography*

Rik Tjallingii, Martin Claussen, Jens Fohlmeister, Alexandra Jahn, Jan-Berend W. Stuut, Torsten Bickert, Frank Lamy, and Ursula Röhl: “ Continental humidity in Northwest Africa on orbital and sub-orbital time scales.“

To be submitted to *Nature*

1.3 Northwest African regional settings

1.3.1 Northwest African climate

Northwest Africa is located between cooler temperate and sub-polar water masses and the warm tropical waters of the Equatorial Atlantic (Figure 4) that both influence the climate over this part of the African continent. The most important atmospheric feature of the Northwest African climate is the ITCZ (Nicholson, 2000) indicated as the geographical position where the northeastern trade winds meet the southeastern trade winds (Figure 4). The surface trade wind systems migrate seasonally along with the position of the ITCZ between approximately 20°N and 5°N. The ITCZ reaches its northern most position during boreal summer that causes the southeastern trade winds to bend in a southwestern direction over the African continent as a humid monsoon flow (Nicholson, 2000). The low-level monsoonal flow delivers moist from the southern sub-tropical Atlantic into Northwestern Africa the during the monsoon season. Precipitation in the Northern Sahel region and the Southern Sahara is linked to heavy precipitation from westward moving disturbances, or squall lines, forced by mid-tropospheric easterly jets which form during boreal summer (Nicholson, 2000). The monsoonal flow over this region ceases during boreal winter when the ITCZ reaches its southern most position. Moreover, storm tracks of the equatorial displaced mid-latitude westerlies supply winter rainfall in the North African Mediterranean zone (north of 24°N) (Nicholson, 2000). Precipitation in the hyperarid Saharan Desert that stretches roughly between 32°N and 20°N is low and irregular (Nicholson, 2000).

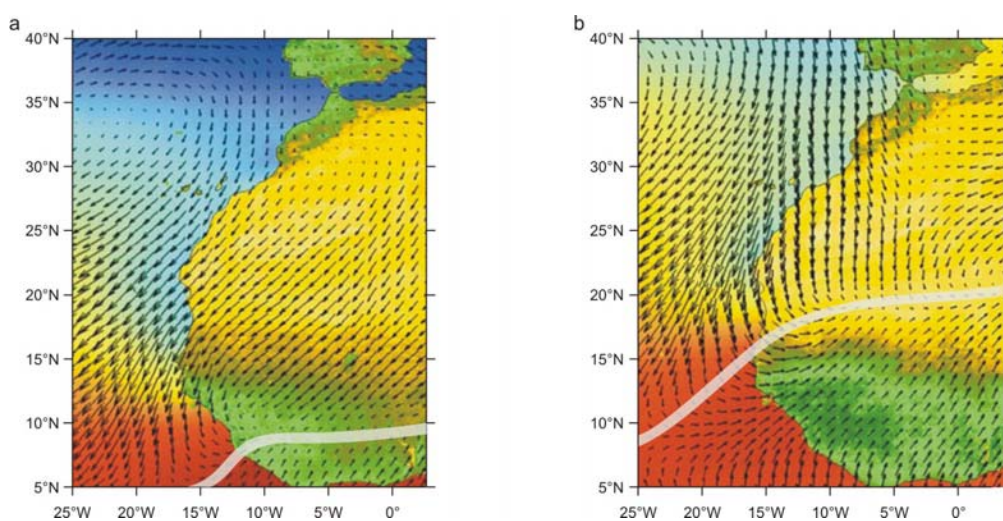


Figure 4 Map of the present-day Northwest African surface wind systems (black arrows), continental vegetation cover (green), and sea surface temperatures after *Adkins et al.* (2006). a) Winter conditions (December, January, February) when the ITCZ (white zone) at its southern most position. b) Summer conditions (June, July, August). Modified after *Adkins et al* (2006).

The hyper arid Sahara Desert is the largest global producer of eolian mineral dust. The global distribution of eolian dust from this region occurs predominantly during boreal summer by the mid-tropospheric easterly jet stream, known as the Saharan Air Layer (Prospero and Lamb, 2003; Stuut et al., 2005). The major uptake process that elevates eolian dust to mid-troposphere levels is related to dust storms that move ahead from the westward moving squall lines. However, by far the largest amount of silt-sized eolian dust is transported by the northeast trade wind system into the Eastern Atlantic off Northwest Africa (Stuut et al., 2005; Swap et al., 1996). Such dust outbreaks (Figure 5) are more common during boreal winter when the trade wind intensities and zonality increase due to the southern position of the ITCZ (Bertrand et al., 1996; Stuut et al., 2005). Additionally, the Harmattan wind system, which is a particular expression of the Northeast trade winds with highest intensities during boreal winter, transports eolian dust from the central Sahara mainly into the equatorial Atlantic (Stuut et al., 2005). As shown in Figure 6, surface sediments from the Northwest African margin indicate relatively high proportions of coarse-grained silt in the coastal regions and especially off Cape Blanc where the Northeast trade winds are active year-round. Finer-grained eolian transported material found in more distal surface sediments has been related to down-wind depletion of the silt-sized eolian dust load (Holz et al., 2005; Sarnthein and Koopmann, 1980; Weltje and Prins, 2003). Present-day aerosol samples collected off Northwest Africa indicate that proximal silt-sized eolian dust is transported predominantly by the surface trade winds (Stuut et al., 2005). Off Northwest Africa, downwind depletion of silt-sized grains, which are mainly quartz, cause a downwind enrichment of fine-grained clay minerals (Glaccum and Prospero, 1980; Parkin and Shackleton, 1973). Moreover, pale quartz grains originate from local coastal dust sources whereas iron-stained quartz grains are derived from the southern Sahara and the northern Sahel region (Koopmann, 1979; Sarnthein and Koopmann, 1980) providing additional information on the source area of the eolian material transported to the proximal northwestern African margin. The clay to fine-silt sized terrigenous sediment fraction is interpreted as hemipelagic mud associated with fluvial supply (Holz et al., 2004; Sarnthein and Koopmann, 1980; Weltje and Prins, 2003). The hemipelagic end member is most abundant north of Cape Yubi (Figure 6c), where rivers from the Atlas Mountains discharge. In addition, abundant fluvial derived sediments are also found in surface sediments off the Sengal River that discharges at ~17 °N (Sarnthein and Koopmann, 1980).

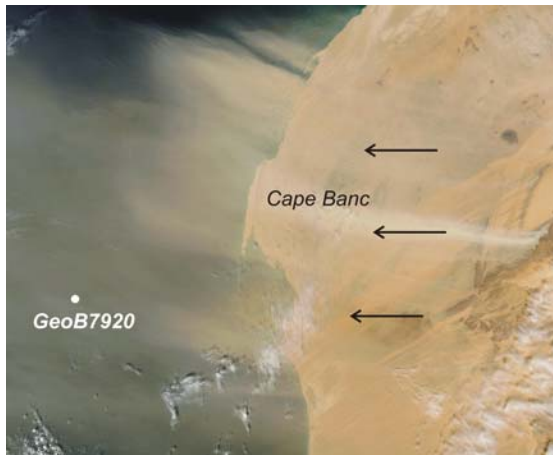


Figure 5. Satellite image of dust storm in the Cape Blanc region at February 2003 (<http://visibleearth.nasa.gov/>). The Northeast trade winds (black arrows) are the major dust carrier to the proximal regions of the continental margin off Northwestern Africa.

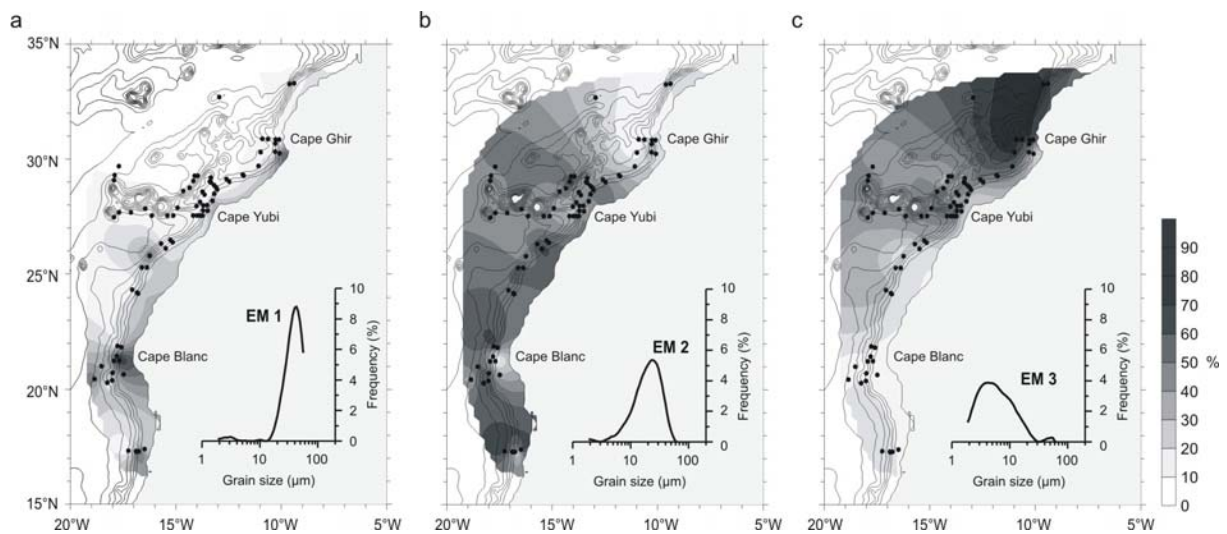


Figure 6. Spatial distribution of the dominant terrigenous grain-size distributions obtained from surface sediment samples off Northwestern Africa, modified after *Holz et al.*, (2005). a) Proportional distribution of the coarse-grained (proximal) eolian terrigenous sediment fraction. b) Proportional distribution of the fine-grained (distal) eolian terrigenous sediment fraction. c) Proportional distribution of the clay to fine-silt sized fluvial sediment fraction.

Despite the present-day hyperarid conditions, Holocene climate reconstructions indicate humid conditions with extended grasslands and numerous lakes that covered the now hyperarid Sahara desert during the early Holocene (Gasse, 2000; Jolly et al., 1998; Prentice et al., 2000). The early Holocene African humid conditions are associated with optimum low latitude summer insolation increasing the land-sea thermal gradient and enhancing the strength of the African monsoon system (Kutzbach and Liu, 1997; Kutzbach and Street-Perrott, 1985). However, pollen and microfossil plant data from the northern Sahara, and paleoclimate reconstructions of the northern Red Sea area suggest additional contributions of Mediterranean precipitation and vegetation during the early Holocene African humid period (Arz et al., 2003; Prentice et al., 2000). Modeling studies indicate that progressive feedbacks

between regional precipitation, vegetation cover, and vegetation albedo effects played a crucial role in developing such humid conditions (Brovkin et al., 1998). These biophysical feedback mechanisms are highly non-linear and cause relatively rapid shifts from a humid state into a arid desert state climate and vice versa (Claussen et al., 1999; Renssen et al., 2006). In addition, these climate models suggest that Holocene North African climate changes is primarily forced by insolation (Claussen et al., 1999; Renssen et al., 2003) and atmospheric greenhouse gasses (Renssen et al., 2003; Renssen et al., 2006). During these humid conditions, the Sahara region was a habitat for savannah fauna such as antelope, giraffe, elephant, hippopotamus, crocodiles and human populations. Archeological evidence indicates that human populations were able to accomplish cultivation of bananas, rice, and different kinds of cereals. Expansion of the vegetation cover strongly reduced the input of eolian dust to the adjacent Atlantic Ocean, which in turn strongly reduced the terrigenous input off Northwest Africa (deMenocal et al., 2000a). Moreover, a large and well-developed submarine canyon system incising the slope off Mauritania at 20 °N suggests active river discharge of a large river system during past humid conditions. Active river discharge in the region during humid condition is further supported by drainage basin model results indicating by a large paleoriver system that drained the Western Sahara during more humid conditions (Vörösmarty et al., 2000).

Over geological time scales, variations in the subtropical African hydrological balance are recorded by variations in the eolian dust load in marine sediments (deMenocal, 1995; Parkin and Shackleton, 1973; Rea, 1994; Tiedemann et al., 1994; Tiedemann et al., 1989). Eolian dust loads increase when dry conditions reduce the vegetation cover and dry soil surfaces are exposed to wind deflation (Parkin and Shackleton, 1973; Pye, 1987). The paleowind wind intensity can be estimated from grain-size data of eolian transported material (Parkin and Shackleton, 1973; Sarnthein et al., 1981) and the heavy mineral fraction related with the proportion Zircon (Matthewson et al., 1995). Northwest African dust records show periodic variations coherent with high-latitude ice volume variations related with increased continental aridity during glacial conditions during the Pleistocene (deMenocal, 1995; Tiedemann et al., 1994). Expansion of high-latitude ice sheets during the latest Pleistocene last glacial maximum forced an equatorward migration of the polar front increasing the meridional pressure gradient that increased the continental aridity and intensified atmospheric circulations over Northwest Africa (Pokras and Mix, 1985; Sarnthein et al., 1981; Street-Perrott and Perrott, 1990). However, aridity variations over Northwest Africa closely correspond to variations of the northern hemisphere summer insolation and the strength of the

African monsoonal system (e.g. Abrantes, 2003; Pokras and Mix, 1985). The eolian dust record off Cape Blanc indicates that sub-tropical northern Africa also corresponds to monsoonal variations during the Holocene interglacial conditions (deMenocal et al., 2000a). Additionally, marine sediments records and paleolake levels of the last deglaciation indicated coherent high- and low-latitude climate variability over Northwest Africa (deMenocal et al., 2000b; Gasse et al., 1990). Strongly reduced North Atlantic SSTs attributed to Heinrich event H1 and the Younger Dryas were transmitted southward with the eastern boundary current into the subtropical Atlantic off NW Africa (Chapman, 1996; Zhao et al., 1995) and the Mediterranean region (Cacho et al., 1999; Martrat et al., 2004). Prolonged droughts during the last deglaciation and Holocene documented by subtropical African paleolakes were coincident with high-latitude fresh water input events (Gasse, 2002; Street-Perrott and Perrott, 1990). Additionally, abruptly increasing eolian dust input recorded in marine sediments off Northwest Africa indicate increased Northwest African aridity during the Younger Dryas (deMenocal et al., 2000a).

1.3.2 Marine productivity and oceanography off Northwest Africa

Primary production in surface waters off Northwest Africa depends on the nutrient supply of the upwelling water masses and fertilization of eolian mineral dust of fluvial supply (e.g. Zhao et al., 2006, and references therein). At present, the Northeast trade wind system controls the westward-directed Ekman transport of near surface waters resulting in upwelling of nutrient-rich subsurface water masses (Helmke et al., 2005; Wefer and Fischer, 1993). Wind induced upwelling occurs over the continental shelf between 20° and 32°N during boreal summer, and between 10° and 25°N during boreal winter (Figure 7). The seasonal shift of the upwelling region is related to the seasonal migration of the ITCZ and the Northeastern trade winds (Helmke et al., 2005; Wefer and Fischer, 1993). Upwelling and trade winds are a year-round phenomenon in the region off Cape Blanc and form large filaments that extend several hundreds of kilometers off the coast (e.g. Helmke et al., 2005, and references therein). In the region north of Cape Blanc, the southward flowing oxygen-rich and relatively low-nutrient North Atlantic Central Water (NACW) underlies the surface waters of the Canary Current (Hagen, 2001; Siedler and Onken, 1996). South of Cape Blanc, surface waters are underlain by the northward flowing low oxygen and nutrient-rich South Atlantic Central Waters (SACW) (Figure 8). The Canary Current detaches off shore in a westward direction at ~ 22°N (Figure 2 a) forming a boundary follows southern boundary of the Canary Current. This boundary separates coastal upwelling from open ocean productivity off Cape Blanc

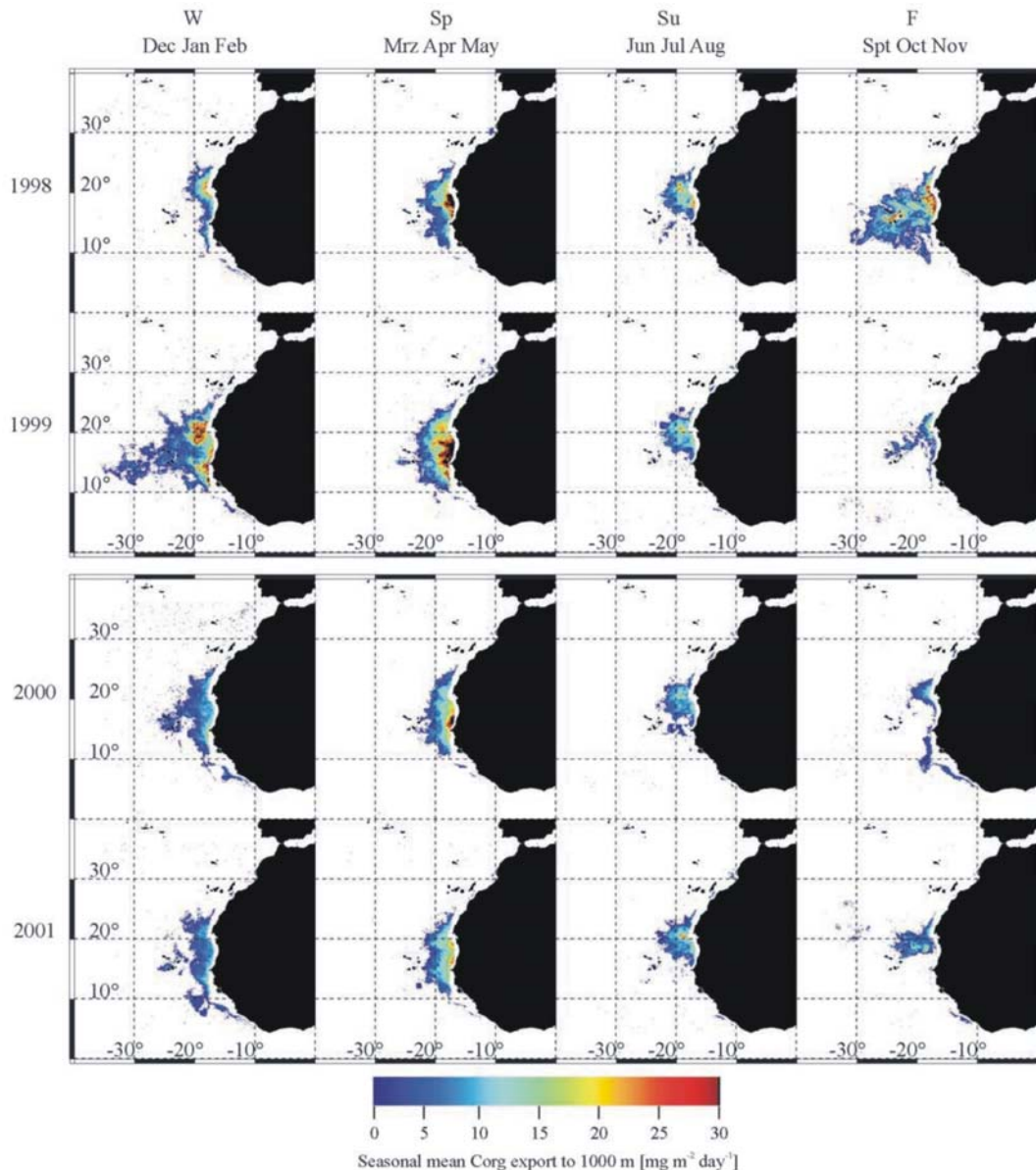


Figure 7. Seasonal averaged transport of organic carbon from the surface waters to 1000 m water depths off Northwest Africa between 1998 and 2001 as calculated from sediment trap data and satellite-derived sea surface chlorophyll (Helmke et al., 2005).

(Hagen, 2001; Mittelstaedt, 1991) and causes eddy-type mixing between the NACW and the SACW (Barton, 1998; Hagen, 2001). Moreover, the westward bending Canary Current forces the poleward flowing SACW to form an under current at depth (Mittelstaedt, 1991). The exceptional high productivity between fall 1998 and spring 1999 (Figure 7) followed after a strongly increased El Niño-Southern Oscillation (ENSO) index in the previous year (Helmke et al., 2005). In addition, present-day oceanographic studies suggest that productivity variations depend on the supply of SACW from the equatorial Atlantic into the region off Northwest Africa, which can be influenced by ENSO or North Atlantic Oscillation (NAO) variations (Hagen, 2001).

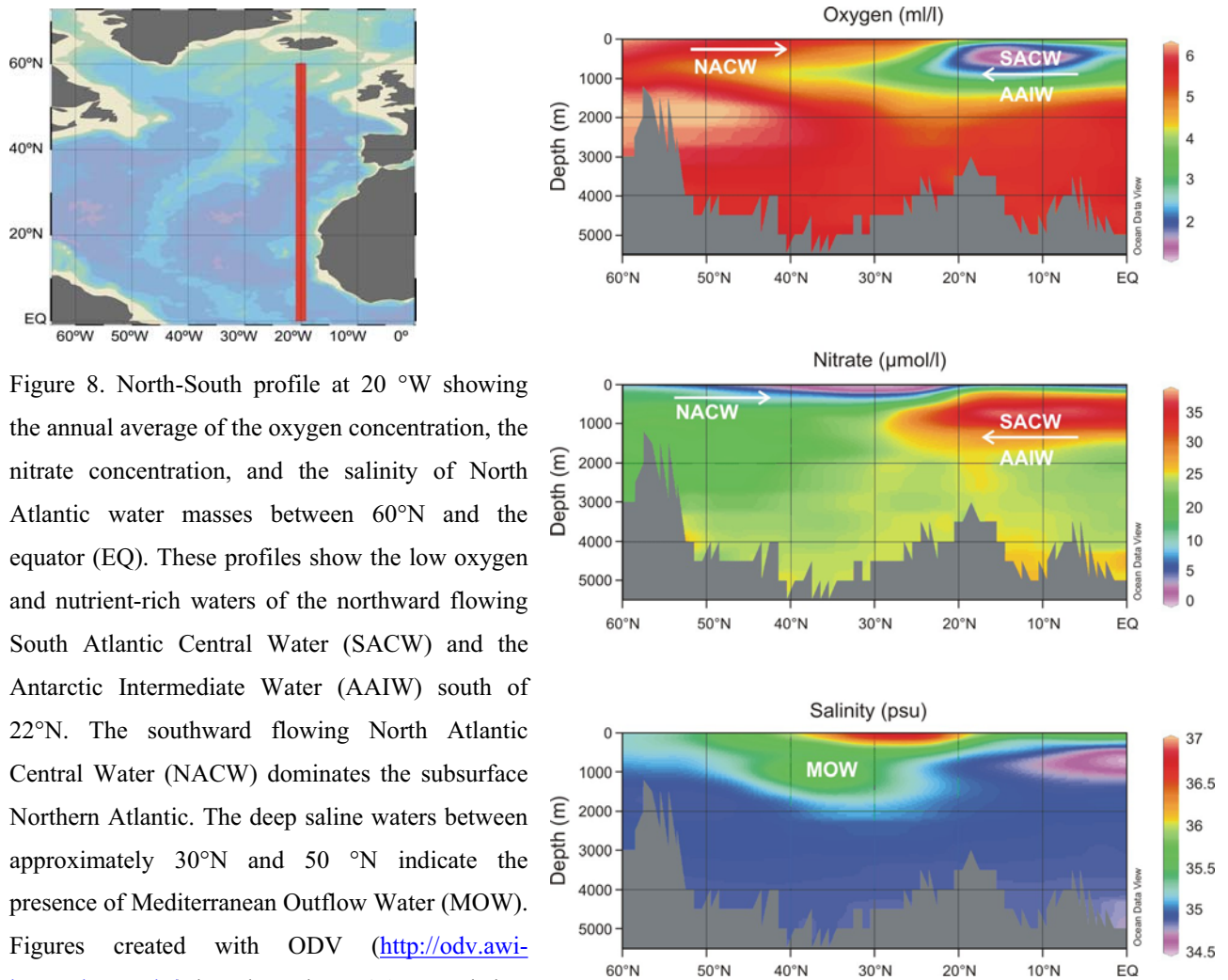


Figure 8. North-South profile at 20 °W showing the annual average of the oxygen concentration, the nitrate concentration, and the salinity of North Atlantic water masses between 60°N and the equator (EQ). These profiles show the low oxygen and nutrient-rich waters of the northward flowing South Atlantic Central Water (SACW) and the Antarctic Intermediate Water (AAIW) south of 22°N. The southward flowing North Atlantic Central Water (NACW) dominates the subsurface Northern Atlantic. The deep saline waters between approximately 30°N and 50 °N indicate the presence of Mediterranean Outflow Water (MOW). Figures created with ODV (<http://odv.awi-bremerhaven.de/>) based on the WOA annual data (Conkright et al., 2002).

The organic carbon in marine sediments off Cape Blanc originates mainly from marine primary producers such as marine diatoms, coccolithophorids, and dinoflagellates (Harris et al., 1996; Martinez et al., 1996; Stein et al., 1989). In general, paleoproductivity records indicate higher primary productivity in the eastern Atlantic boundary current system off Portugal and off Northwest Africa during glacial conditions (Freudenthal et al., 2002; Pailler and Bard, 2002). Increased productivity off Northwest Africa during glacial conditions has been related to the increased trade wind intensities on one hand, but also to migration zonal migration of the productivity regions forced by sea level change (Bertrand et al., 2000; Bertrand et al., 1996; Freudenthal et al., 2002). However, millennial-scale productivity variations off Portugal indicate that upwelling completely ceased during glacial Heinrich events due to the introduction of melt water from the North Atlantic and possibly increased zonality of the upwelling favorable wind system (Bard et al., 2000; Pailler and Bard, 2002). Additionally, modeling results and productivity records off Morocco indicate reduced

productivity during Heinrich events related to surface water stratification and stronger seasonality (Meggers et al., *unpublished*). Strongly reduced productivity off Cape Blanc during the last glacial maximum (Bertrand et al., 1996; Harris et al., 1996; Martinez et al., 1999; Zhao et al., 2006) have been related to the exposure of the continental shelf that inhibited lateral advection of nutrients over the shelf (Bertrand et al., 1996; Martinez et al., 1999). Migration of coastal upwelling centers induced by sea level variations has been suggested as major forcing factor for these strong regional differences (Bertrand et al., 1996; Freudenthal et al., 2002; Martinez et al., 1999). In addition, reduced upwelling intensities off Cape Blanc during the windy glacial conditions have been related to an increased zonality of the glacial trade winds that reduced the Ekman transport and the coastal upwelling (Bertrand et al., 1996; Martinez et al., 1999). Late Pleistocene productivity records indicate high productivity in the complete eastern Atlantic boundary current system from the Portuguese margin down to Cape Blanc during the last deglaciation (Freudenthal et al., 2002; Harris et al., 1996; Moreno et al., 2002; Paillet and Bard, 2002). The increased productivity during the last deglaciation has been related to large-scale reorganization of the oceanic and atmospheric circulation changes in this region associated with the major melting phase of the high-latitude ice volume (Harris et al., 1996; Martinez et al., 1999; Moreno et al., 2002; Tiedemann et al., 1989; Zhao et al., 2006). Alternatively, Bertrand et al (2000) couple the increased productivity of the last deglaciation in marginal sediment cores off Northwest Africa to transgressional erosion of shelf sediments resulting and consequently redistribution of nutrients. Detailed reconstruction of Holocene opal accumulation rates suggest that upwelling intensities off Cape Blanc are closely related to the position of the ITCZ and the trade wind intensities and therefore reduced during periods of enhanced African humidity (Adkins et al., 2006).

- 2. Methods -

2.1 X-ray fluorescence spectrometry

2.1.1 Principles of fluorescence spectrometry and XRF Core Scanners

The X-ray fluorescence (XRF) core scanner is a computer-controlled core-scanning tool that analyzes the chemical composition of sediments directly at the surface of a split sediment core (Figure 1). Therefore, XRF core scanner measurements are non-destructive, consumable costs are relatively low, and sample preparation is minimized compared to conventional chemical analysis on discrete samples. The high sampling resolution of the XRF core scanner (down to 2 mm) provides nearly continuous information about the chemical composition of the sediment and meets the growing demand on high-resolution sedimentary records. Detailed XRF core scans have already successfully been used for high-resolution time-series studies, stratigraphic correlations, and detailed sedimentary and climatic reconstructions on various time scales (e.g. Bahr et al., 2005; Grützner et al., 2005; Haug et al., 2001; Hepp et al., 2006; Jaccard et al., 2005; Kuhlmann et al., 2004; Lamy et al., 2001; Röhl et al., 2001; Westerhold et al., 2005).

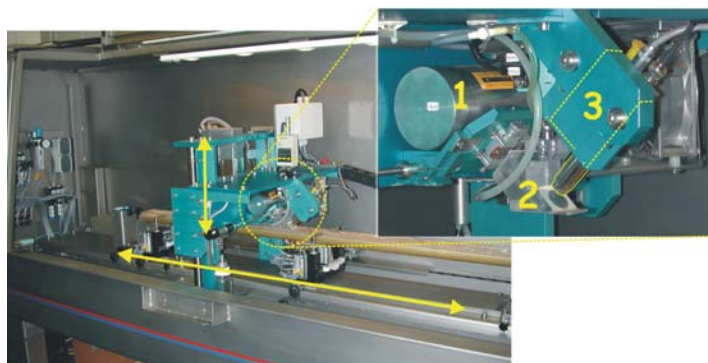


Figure 1. View on the inside of the XRF core scanner II at the MARUM institute, University of Bremen. The measurement unit with the X-ray source (1), the He flushed prism (2), and the detector (3) moves horizontally over the split sediment core and can touch the sediment surface at any given sample position.

X-ray fluorescence spectrometry uses an X-ray beam to ionize the atoms in the sample material by ejecting a K-shell electron. Subsequently, an electron from a higher L or M shell fills the vacancy of the inner electron shell emitting the element characteristic surplus energy as a K_{α} or K_{β} X-ray fluorescence photon or emission line (Figure 2). The element characteristic photon energy (E) with a particular frequency (f) and an associated wavelength (λ) can be expressed as electromagnetic energy according to:

$$E = hf = hc / \lambda \quad c \sim 3.0 \cdot 10^8 \text{ m/s (speed of light)} \quad (1)$$

$$h \sim 6.626069 \cdot 10^{-34} \text{ } \mu\text{eV, or } \sim 4.13567 \text{ GHz (Planck's constant)}$$

An overview of the element characteristic K and L emission line energies for each element and its atomic number are given in the periodic table of elements (Figure 3). The characteristic electromagnetic spectrum that is emitted or absorbed by atoms follow an empirical law that relates the electromagnetic frequencies with the element's atomic number, called Moseley's Law (Moseley, 1914). This law shows that the ionization energy and the characteristic fluorescence energy of an atom increase with the square of the atomic number according to:

$$\sqrt{f} = k_1 (Z + k_2) \quad f \text{ is the frequency of the emission line (e.g } K_\alpha) \quad (2)$$

Z is the element's atomic number

k_1 and k_2 are emission line depend constants

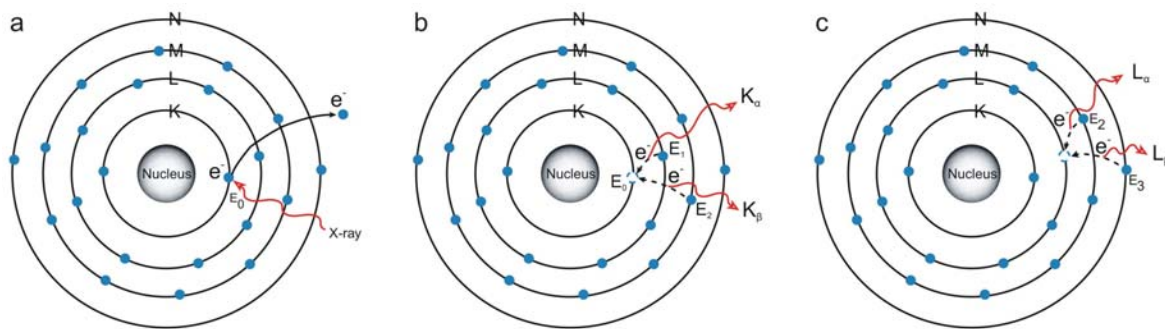


Figure 2. Example of the X-ray fluorescence process on a Titanium atom (Ti, atomic number 22). a) Incoming radiation from the X-ray tube ejects a K-shell electron. b) The vacancy in the K-shell is filled by a L-shell electron emitting the element characteristic K_α radiation, or by a M-shell emitting the element characteristic K_β radiation. c) The vacancy in the L-shell is filled by a M-shell electron emitting the element characteristic L_α radiation, or by a N-shell emitting the element characteristic L_β radiation (modified after: <http://www.amptek.com/pdf/xrf.pdf>).

In case of the XRF core scanner, the incoming X-rays penetrate the sediment surface and ionize the elements within the sediment that subsequently emit their characteristic emission line energies (Figure 4). According to Moseley's law, heavier elements emit relatively high fluorescence energies that are less susceptible to scatter and absorption within the sample material. Consequently, the outgoing fluorescence radiation is linked to the atomic number of the element resulting in larger response depths for heavier elements that emit relatively high fluorescence energies (Figure 3). For instance, the response depths of the fluorescence radiation, or critical depth, is $\sim 8 \mu\text{m}$ for Aluminum (Al, atomic number 13), $\sim 36 \mu\text{m}$ for Calcium (Ca, atomic number 20), and $\sim 180 \mu\text{m}$ for Iron (Fe, atomic number 26) (Potts, 1987). Due to the relatively small critical depth, and subsequent sample

Group IA		Group IIA		Group VIII										Group VIIA		Group VIIIA																																																																																																																																																																																																																																																																																																																																																																																																																																																																																																																																																																																																																																																																																																																																																																																																																																																																																																																																																																																																																												
Key to Energy Values in keV		Key to Energy Values in keV		Key to Energy Values in keV		Key to Energy Values in keV		Key to Energy Values in keV		Key to Energy Values in keV		Key to Energy Values in keV		Key to Energy Values in keV		Key to Energy Values in keV																																																																																																																																																																																																																																																																																																																																																																																																																																																																																																																																																																																																																																																																																																																																																																																																																																																																																																																																																																																																																												
K _{α1} K _{β1}		K _{α1} K _{β1}		K _{α1} K _{β1}		K _{α1} K _{β1}		K _{α1} K _{β1}		K _{α1} K _{β1}		K _{α1} K _{β1}		K _{α1} K _{β1}		K _{α1} K _{β1}																																																																																																																																																																																																																																																																																																																																																																																																																																																																																																																																																																																																																																																																																																																																																																																																																																																																																																																																																																																																																												
L _{α1} L _{β1}		L _{α1} L _{β1}		L _{α1} L _{β1}		L _{α1} L _{β1}		L _{α1} L _{β1}		L _{α1} L _{β1}		L _{α1} L _{β1}		L _{α1} L _{β1}		L _{α1} L _{β1}																																																																																																																																																																																																																																																																																																																																																																																																																																																																																																																																																																																																																																																																																																																																																																																																																																																																																																																																																																																																																												
H 1	0.052	Li 3	0.110	Be 4	0.110	Na 11	1.25	Mg 12	1.30	K 19	3.31	Ca 20	3.69	Sc 21	4.09	Ti 22	4.51	V 23	4.95	Cr 24	5.41	Mn 25	5.90	Fe 26	6.40	Co 27	6.93	Ni 28	7.48	Cu 29	8.05	Zn 30	8.64	Ga 31	9.25	Ge 32	9.89	As 33	10.54	Se 34	11.22	Br 35	11.92	Kr 36	12.85	Rb 37	13.39	Sr 38	14.16	Y 39	14.96	Zr 40	15.77	Nb 41	16.61	Mo 42	17.48	Tc 43	18.41	Ru 44	19.28	Rh 45	20.21	Pd 46	21.18	Ag 47	22.16	Cd 48	23.17	In 49	24.21	Sn 50	25.27	Sb 51	26.36	Te 52	27.47	I 53	28.61	Xe 54	29.80	Cs 55	30.97	Ba 56	32.19	La 57-71	33.44	Ce 58	34.72	Pr 59	36.02	Nd 60	37.36	Pm 61	38.65	Sm 62	40.12	Eu 63	41.53	Gd 64	42.98	Tb 65	44.47	Dy 66	45.99	Ho 67	47.53	Er 68	49.10	Tm 69	50.73	Yb 70	52.36	Lu 71	54.06	Hf 72	55.76	Ta 73	57.52	W 74	59.31	Re 75	61.13	Os 76	62.99	Ir 77	64.89	Pt 78	66.82	Au 79	68.79	Hg 80	70.82	Tl 81	72.86	Pb 82	74.96	Bi 83	77.10	Po 84	79.30	At 85	81.53	Rn 86	83.80	Fr 87	12.03	Ra 88	12.34	Ac 89	12.65	Th 90	12.87	Pa 91	13.29	U 92	13.61	Np 93	13.95	Pu 94	14.28	Am 95	14.62	Cm 96	14.96	Bk 97	15.31	Cf 98	15.66	Es 99	16.02	Fm 100	16.38	Md 101	16.75	No 102	17.13	Lr 103	17.49	Ac 104	17.84	Th 105	18.19	Pa 106	18.54	U 107	18.89	Np 108	19.24	Pu 109	19.59	Am 110	19.94	Cm 111	20.29	Bk 112	20.64	Cf 113	20.99	Es 114	21.34	Fm 115	21.69	Md 116	22.04	No 117	22.39	Lr 118	22.74	Ac 119	23.09	Th 120	23.44	Pa 121	23.79	U 122	24.14	Np 123	24.49	Pu 124	24.84	Am 125	25.19	Cm 126	25.54	Bk 127	25.89	Cf 128	26.24	Es 129	26.59	Fm 130	26.94	Md 131	27.29	No 132	27.64	Lr 133	27.99	Ac 134	28.34	Th 135	28.69	Pa 136	29.04	U 137	29.39	Np 138	29.74	Pu 139	30.09	Am 140	30.44	Cm 141	30.79	Bk 142	31.14	Cf 143	31.49	Es 144	31.84	Fm 145	32.19	Md 146	32.54	No 147	32.89	Lr 148	33.24	Ac 149	33.59	Th 150	33.94	Pa 151	34.29	U 152	34.64	Np 153	34.99	Pu 154	35.34	Am 155	35.69	Cm 156	36.04	Bk 157	36.39	Cf 158	36.74	Es 159	37.09	Fm 160	37.44	Md 161	37.79	No 162	38.14	Lr 163	38.49	Ac 164	38.84	Th 165	39.19	Pa 166	39.54	U 167	39.89	Np 168	40.24	Pu 169	40.59	Am 170	40.94	Cm 171	41.29	Bk 172	41.64	Cf 173	41.99	Es 174	42.34	Fm 175	42.69	Md 176	43.04	No 177	43.39	Lr 178	43.74	Ac 179	44.09	Th 180	44.44	Pa 181	44.79	U 182	45.14	Np 183	45.49	Pu 184	45.84	Am 185	46.19	Cm 186	46.54	Bk 187	46.89	Cf 188	47.24	Es 189	47.59	Fm 190	47.94	Md 191	48.29	No 192	48.64	Lr 193	48.99	Ac 194	49.34	Th 195	49.69	Pa 196	50.04	U 197	50.39	Np 198	50.74	Pu 199	51.09	Am 200	51.44	Cm 201	51.79	Bk 202	52.14	Cf 203	52.49	Es 204	52.84	Fm 205	53.19	Md 206	53.54	No 207	53.89	Lr 208	54.24	Ac 209	54.59	Th 210	54.94	Pa 211	55.29	U 212	55.64	Np 213	55.99	Pu 214	56.34	Am 215	56.69	Cm 216	57.04	Bk 217	57.39	Cf 218	57.74	Es 219	58.09	Fm 220	58.44	Md 221	58.79	No 222	59.14	Lr 223	59.49	Ac 224	59.84	Th 225	60.19	Pa 226	60.54	U 227	60.89	Np 228	61.24	Pu 229	61.59	Am 230	61.94	Cm 231	62.29	Bk 232	62.64	Cf 233	62.99	Es 234	63.34	Fm 235	63.69	Md 236	64.04	No 237	64.39	Lr 238	64.74	Ac 239	65.09	Th 240	65.44	Pa 241	65.79	U 242	66.14	Np 243	66.49	Pu 244	66.84	Am 245	67.19	Cm 246	67.54	Bk 247	67.89	Cf 248	68.24	Es 249	68.59	Fm 250	68.94	Md 251	69.29	No 252	69.64	Lr 253	69.99	Ac 254	70.34	Th 255	70.69	Pa 256	71.04	U 257	71.39	Np 258	71.74	Pu 259	72.09	Am 260	72.44	Cm 261	72.79	Bk 262	73.14	Cf 263	73.49	Es 264	73.84	Fm 265	74.19	Md 266	74.54	No 267	74.89	Lr 268	75.24	Ac 269	75.59	Th 270	75.94	Pa 271	76.29	U 272	76.64	Np 273	76.99	Pu 274	77.34	Am 275	77.69	Cm 276	78.04	Bk 277	78.39	Cf 278	78.74	Es 279	79.09	Fm 280	79.44	Md 281	79.79	No 282	80.14	Lr 283	80.49	Ac 284	80.84	Th 285	81.19	Pa 286	81.54	U 287	81.89	Np 288	82.24	Pu 289	82.59	Am 290	82.94	Cm 291	83.29	Bk 292	83.64	Cf 293	83.99	Es 294	84.34	Fm 295	84.69	Md 296	85.04	No 297	85.39	Lr 298	85.74	Ac 299	86.09	Th 300	86.44	Pa 301	86.79	U 302	87.14	Np 303	87.49	Pu 304	87.84	Am 305	88.19	Cm 306	88.54	Bk 307	88.89	Cf 308	89.24	Es 309	89.59	Fm 310	89.94	Md 311	90.29	No 312	90.64	Lr 313	90.99	Ac 314	91.34	Th 315	91.69	Pa 316	92.04	U 317	92.39	Np 318	92.74	Pu 319	93.09	Am 320	93.44	Cm 321	93.79	Bk 322	94.14	Cf 323	94.49	Es 324	94.84	Fm 325	95.19	Md 326	95.54	No 327	95.89	Lr 328	96.24	Ac 329	96.59	Th 330	96.94	Pa 331	97.29	U 332	97.64	Np 333	97.99	Pu 334	98.34	Am 335	98.69	Cm 336	99.04	Bk 337	99.39	Cf 338	99.74	Es 339	100.09	Fm 340	100.44	Md 341	100.79	No 342	101.14	Lr 343	101.49	Ac 344	101.84	Th 345	102.19	Pa 346	102.54	U 347	102.89	Np 348	103.24	Pu 349	103.59	Am 350	103.94	Cm 351	104.29	Bk 352	104.64	Cf 353	104.99	Es 354	105.34	Fm 355	105.69	Md 356	106.04	No 357	106.39	Lr 358	106.74	Ac 359	107.09	Th 360	107.44	Pa 361	107.79	U 362	108.14	Np 363	108.49	Pu 364	108.84	Am 365	109.19	Cm 366	109.54	Bk 367	109.89	Cf 368	110.24	Es 369	110.59	Fm 370	110.94	Md 371	111.29	No 372	111.64	Lr 373	111.99	Ac 374	112.34	Th 375	112.69	Pa 376	113.04	U 377	113.39	Np 378	113.74	Pu 379	114.09	Am 380	114.44	Cm 381	114.79	Bk 382	115.14	Cf 383	115.49	Es 384	115.84	Fm 385	116.19	Md 386	116.54	No 387	116.89	Lr 388	117.24	Ac 389	117.59	Th 390	117.94	Pa 391	118.29	U 392	118.64	Np 393	118.99	Pu 394	119.34	Am 395	119.69	Cm 396	120.04	Bk 397	120.39	Cf 398	120.74	Es 399	121.09	Fm 400	121.44	Md 401	121.79	No 402	122.14	Lr 403	122.49	Ac 404	122.84	Th 405	123.19	Pa 406	123.54	U 407	123.89	Np 408	124.24	Pu 409	124.59	Am 410	124.94	Cm 411	125.29	Bk 412	125.64	Cf 413	125.99	Es 414	126.34	Fm 415	126.69	Md 416	127.04	No 417	127.39	Lr 418	127.74	Ac 419	128.09	Th 420	128.44	Pa 421	128.79	U 422	129.14	Np 423	129.49	Pu 424	129.84	Am 425	130.19	Cm 426	130.54	Bk 427	130.89	Cf 428	131.24	Es 429	131.59	Fm 430	131.94	Md 431	132.29	No 432	132.64	Lr 433	132.99	Ac 434	133.34	Th 435	133.69	Pa 436	134.04	U 437	134.39	Np 438	134.74	Pu 439	135.09	Am 440	135.44	Cm 441	135.79	Bk 442	136.14	Cf 443	136.49	Es 444	136.84	Fm 445	137.19	Md 446	137.54	No 447	137.89	Lr 448	138.24	Ac 449	138.59	Th 450	138.94	Pa 451	139.29	U 452	139.64	Np 453	139.99	Pu 454	140.34	Am 455	140.69	Cm 456	141.04	Bk 457	141.39	Cf 458	141.74	Es 459	142.09	Fm 460	142.44	Md 461	142.79	No 462	143.14	Lr 463	143.49	Ac 464	143.84	Th 465	144.19	Pa 466	144.54	U 467	144.89	Np 468	145.24	Pu 469	145.59	Am 470	145.94	Cm 471	146.29	Bk 472	146.64	Cf 473	146.99	Es 474	147.34	Fm 475	147.69	Md 476	148.04	No 477	148.39	Lr 478	148.74	Ac 479	149.09	Th 480	149.44	Pa 481	149.79	U 482	150.14	Np 483	150.49	Pu 484	150.84	Am 485	151.19	Cm 486	151.54	Bk 487	151.89	Cf 488	152.24	Es 489	152.59	Fm 490	152.94	Md 491	153.29	No 492	153.64	Lr 493	153.99	Ac 494	154.34	Th 495	154.69	Pa 496	155.04	U 497	155.39	Np 498	155.74	Pu 499	156.09	Am 500	156.44	Cm 501	156.79	Bk 502	157.14	Cf 503	157.49	Es 504	157.84	Fm 505	158.19	Md 506	158.54	No 507	158.89	Lr 508	159.24	Ac 509	159.59	Th 510	159.94	Pa 511	160.29	U 512	160.64	Np 513	160.99	Pu 514	161.34	Am 515	161.69	Cm

volume analyzed by the XRF core scanner, the lighter elements Al and Si are much more sensitive to sample heterogeneities and mineralogical effects. A proper arrangement of the measurement area can largely compensate for these effects when measuring fine-grained material (Ge et al., 2005; Potts, 1987). However, heterogeneity and surface roughness effects could become more pronounced for coarser-grained sample material.

Two XRF core scanners are in operation at the MARUM institute, University of Bremen. XRF scanner I is a first generation core scanner that was developed and built at the Royal Netherlands Institute for Sea Research (NIOZ, Texel, the Netherlands) in the mid 90-ties. With this scanner it is possible to analyze the elements from Potassium (K, atomic number 19) through to Strontium (Sr, atomic number 38) (Jansen et al., 1998; Röhl and Abrams, 2000). This XRF scanner uses a Molybdenum (Mo) X-Ray source, a Kevex™ peltier-cooled PSI detector with a 125µm thick Beryllium (Be) window, and a multi channel analyzer with a 20 eV spectral resolution. XRF scanner II is a second-generation core scanner and was developed and built by AVAATECH (Texel, the Netherlands). The XRF scanner II is able to analyze a wider elemental range compare to XRF scanner I, from Aluminum (Al, atomic number 13) through to Uranium (U, atomic number 92) (Richter et al., 2006). At present, this scanner is equipped with an Oxford Rhodium (Rh) X-ray source, an Amptek 2-stage Peltier-cooled detector with a 25 µm thick Be window, and a multi-channel analyzer with a spectral resolution of 20 eV (2048 channels). Both systems use a helium-flushed prism to minimize radiation scattering between of the incoming X-ray beam and the outgoing XRF radiation. The X-ray source and the detector are oriented under a 45° angle with the sediment surface and can be lowered to the sediment surface at any given position (Figure 4). The XRF scanners irradiate a sediment surface of 1 cm x 1 cm for sampling intervals ≥ 1 cm, but the

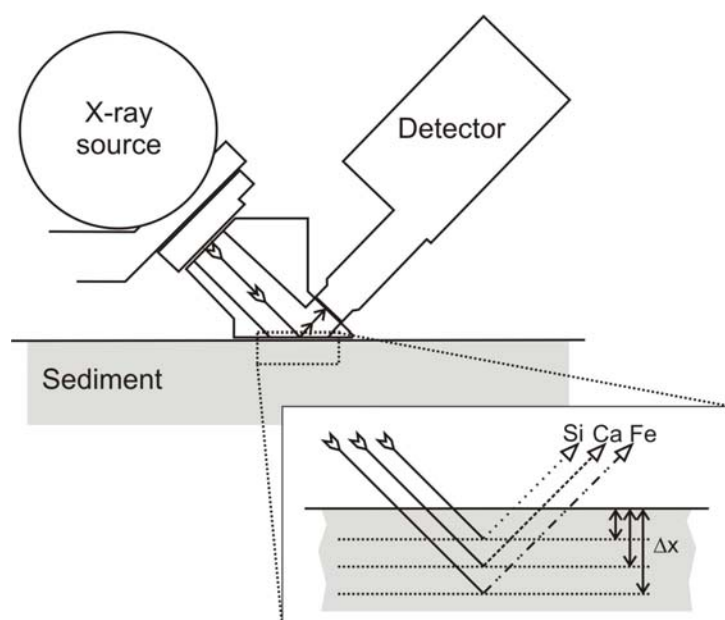


Figure 4. Excitation geometry in XRF core scanner analysis. The critical depth (Δx) of the elements Si, Ca, and Fe (not to scale) are linked to the emitted fluorescence energies. Higher fluorescence energies of heavier elements are less susceptible to absorption and scatter effect with in the sample volume resulting in a larger critical depth.

dimensions can be changed for higher sample resolutions down to 0.2 cm x 1 cm. The detector registers the emission line energies of the irradiated sample material and their frequency over a predefined measure time as element intensities in counts, which are proportional to the element concentrations.

The split sediment cores measured with XRF scanner II are covered with a 4 µm thin SPEXCerti Prep Ultralene® foil to prevent contamination of the measurement unit and desiccation of the sediment during the XRF scanner analyzes. This foil has a high transmission of relatively weak fluorescence energies and a complete transmission for all elements heavier than Cl, which makes it especially suitable for XRF analyses of lighter elements such as Al and Si (Tjallingii et al, *in press.*, Chapter 3). The split sediment cores measured with XRF scanner I are covered with a Mylar foil. Although XRF analyses are not temperature dependent, warming of the core sections to room temperature avoids condensation of water on the foil that might influence the measurements. There should be no air bubbles under the foil, and the foil should be free of wrinkles. Furthermore, the sediment surface should be smoothly equalized to ensure maximum quality of the XRF measurements.

The analytical precision of the XRF core scanner varies with the element intensity that, in turn, is linked to the element concentration, the lithology and physical properties of the sample material, and the hardware settings (Röhl and Abrams, 2000; Westerhold, 2003). The precision and the quality of the XRF measurements improve for higher element intensities. Therefore, the energy level of the X-ray source and the count time are optimized to the X-ray hardware of each core scanner. XRF scanner I is operated with a generator setting of 20 kV and 0.087 mA. The generator settings of XRF scanner II can be changed from 4 kV to 50 kV in combination with six different filters in order to optimize the settings for different elements in relation to their atomic number. The full elemental range from Al to Ba can be covered in a single run. An overview of the optimal instrumental settings for specific sets of elements is given in Table 1. Generally, measurements are carried out with a sampling time of 30 seconds, but this time can be adapted to maximize the results in relation to the available time at the scanner of a given project.

Tube voltage (kV)	Filter	Elemental spectrum
5	-	Al & Si at low bulk concentrations
10	-	Al, Si, P, S, Cl, K, Ca, Ti, Mn, Fe
30	Pd thick	Br, Rb, Sr, Zr
50	Cu	Rb*, Sr, Zr, Ba (*at high bulk concentrations)

Table 1. Instrumental setting for specific sets of elements of XRF core scanner II after Richter et al. (2006).

An incoming XRF photon can be identified by the disturbance of the potential field of the detector crystal. However, the detector crystal can only register one photon at the time. After a photon hits the detector crystal the, potential field has to build-up again in order to measure the next photon. Although this time is very short (in the order of 10^{-3} sec), the amount of time lost due to recharging of the detector crystal will become more significant for higher count rates. To compensate for the recovering time of the detector the measurement time is extended to realize the predefined sample time, which is indicated by the dead time. Therefore, the dead time will increase when the incoming fluorescence count rate increases. The dead time is calculated according to:

$$\text{Dead Time (\%)} = [100 - (\text{Live Time} / \text{Real Time} * 100)] \quad (\text{e.g., LiveTime}=30\text{sec}) \quad (3)$$

The analog signal of the detector has to be converted in a digital signal by the pulse-shaper before the XRF spectrum can be processed. However, a linear input-output relation can only be obtained for a dead time under 40 % (Figure 5). Hence, the optimal generator settings for XRF II are indicated by a dead time between 20% and 40% that ensures the highest possible element intensities. Test runs on the lithological extremes of the sediment core (e.g. darkest and brightest intervals) before starting routine analyzes help define the optimal generator settings.

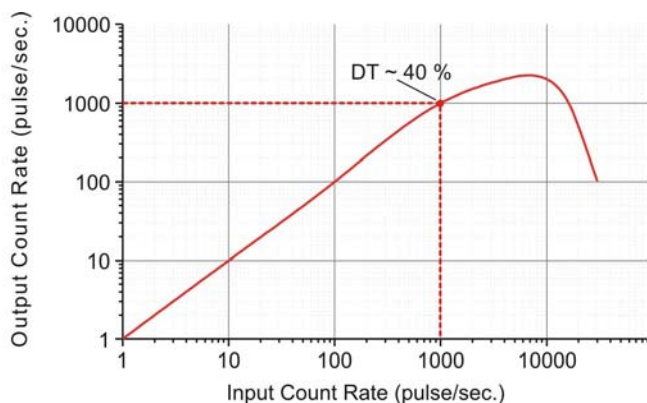


Figure 5. Input count rate (x-axis) and output count rate (y axis) of the Amptek PX2CR shape amplifier (shape time constant = $20\mu\text{sec}$). If the dead time exceeds 40 % the input count rate becomes larger than 1000 pulses a second and becomes non-linear (source: <http://www.amptek.com/px2.html>).

Each XRF measurement comprises a spectrum representing the recorded emission lines and their frequency (Figure 6). Processing software based on iterative least square fitting that convert the XRF spectra into element intensities on a PC linked to the XRF core scanner. The processing software applies background subtraction, sum-peak correction, escape peak correction, and peak integration of the XRF spectrum. XRF scanner I uses the KEVEX™ Toolbox software whereas the XRF scanner II uses the WinAxil and WinBatch software packages of Canberra. The processing software uses an iterative least-square fitting procedure

of a Gaussian function to approximate the fluorescence lines. In general, the goodness-of-fit of a process model increases if the model identifies all peaks present in the XRF spectrum because the program does not look at individual peaks but at groups of peaks. The Canberra WinAxil software used for XRF scanner II allows the user to add (or remove) elements to the processing model in order to improve the goodness-of-fit between the analyzed XRF spectrum and the processing model. The goodness-of-fit is indicated by a χ^2 value that should be less than three. The element intensities (counts) are calculated as the peak areas of the processed model (Figure 6), and can be normalized by the predefined measure time to obtain count rates (counts per second). Although the software applies background subtraction, low background values enhance the peak fitting process. Higher source energies used for the analyses of heavy elements generate much higher background values that predominantly originates from scatter of primary radiation (Jenkins, 1974). However, the application of filters during the XRF analyses enable to suppress the background radiation (Table 1), such as the Cu filter used for the 50 kV analyses that suppresses the background radiation in the central part of the 50 kV spectrum (Figure 6).

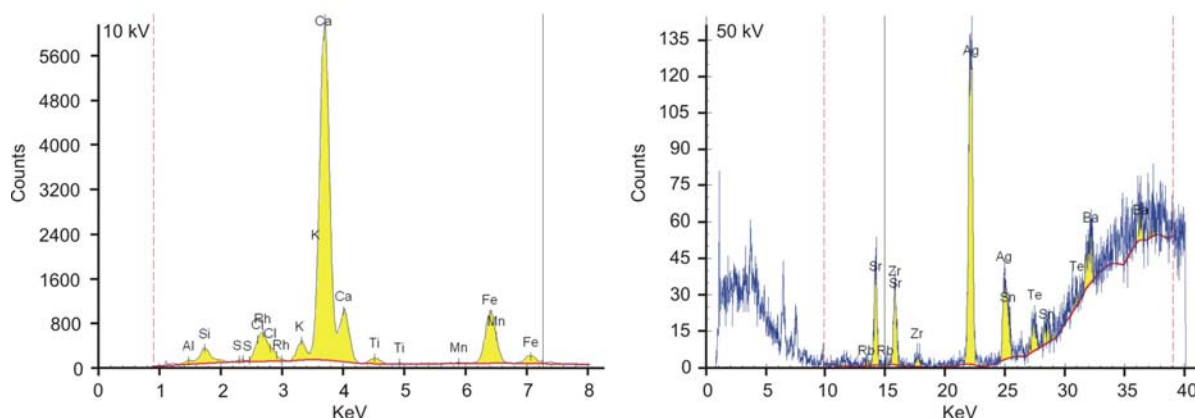


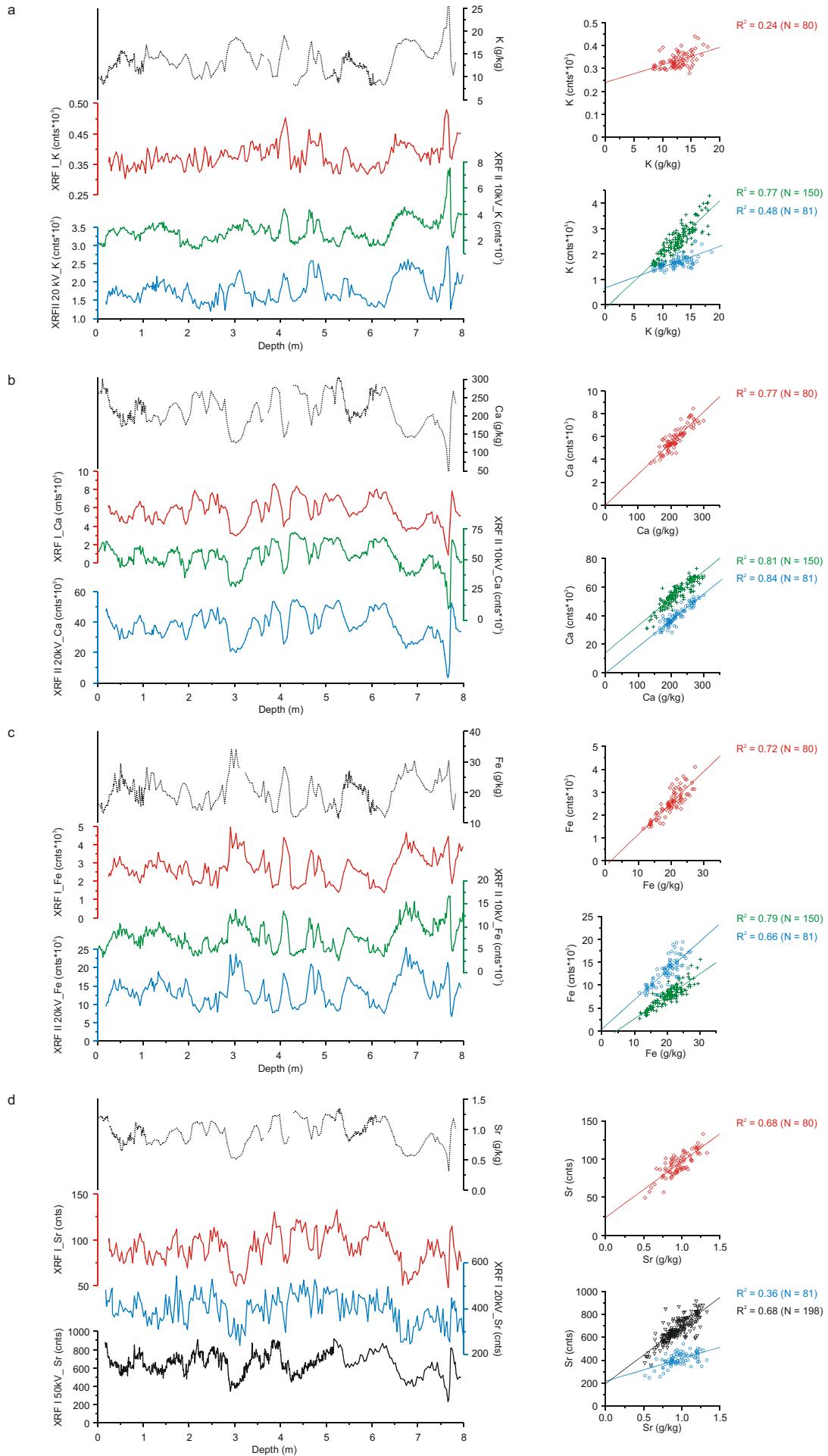
Figure 6. XRF spectra measured at the split core surface of core GeoB7920 (11.90 m) with 10 kV and a 50 kV. The processing software calculates the element intensities by the integration peak area (indicated in yellow).

2.1.2 Comparison of XRF Core Scanner I and II

Deep-sea sediment cores GeoB4216-1 (30.63°N, 12.40°W, 2324 m water depth) and GeoB7919-5 (20.94°N, 19.39°W, 3420 m water depth) were both measured with XRF Core Scanner I and II at The MARUM institute, University of Bremen. These gravity cores were selected based on their different chemical composition. The two lightest elements (K and Ca) and the two heaviest elements (Fe and Sr) measured with XRF scanner I at 20 kV have been compared with XRF scanner II measurements of different generator settings. XRF scanner II analyzed the element intensities of the elements K, Ca, and Fe at both 10 kV and 20 kV, whereas the element intensities of the element Sr was measured at 20 kV and 50 kV. All XRF analyses were performed with a sampling time of 30 seconds. The 50 kV measurements of XRF scanner II were performed in combination with a Cu filter. The XRF measurements of were compared with chemical analyses on discrete sediment samples (in g/kg). Chemical analyses were performed on discrete samples of core GeoB4216-1 with inductive coupled plasma ICP-MS (Plewa, *unpublished*). Chemical analyses were performed on discrete samples of core GeoB7919-5 with the Spectro Xepos EDPXRF analyses (Wien et al., 2006). Chemical data on discrete samples (g/kg), XRF I measurements, and XRFII measurements were obtained for the upper 8 meters of core GeoB4216-1, and the upper 7.7 meter of core GeoB7919-5. XRF measurements of core GeoB7919-5 could not be obtained at gaps in the split surface at 2.14 – 2.24, and 4.50 - 3.90 m. These gaps are smaller for chemical records obtained with XRF scanner II that allows one to chose the measurement track outside of the split core center.

As shown in Figures 7 and 8, both XRF scanners produce satisfying results for the elements Ca, Fe, and Sr of both sediment cores. However, XRF scanner I measurements of the element K are less reliable than the measurements of XRF scanner II for the sediments of core GeoB4216-1 and GeoB7919-5. Westerhold (2003) indicated that the reproducibility of the element K measured with XRF core scanner I strongly improves for elements intensities well over 300 counts in sediments containing high amounts of Ca. In the XRF spectrum, the K_{α} -peak of K is situated very close to the K_{α} -peak of Ca (Figure 6), and the high K_{α} -peak of Ca interferes with the much smaller K_{α} -peak of K (Westerhold, 2003). Measuring the element

Figure 7 (next page). Chemical analyses of sediment core GeoB4216-1 measured with ICP (black dotted line), XRF Core Scanner I (red), XRF Core Scanner II at 10 kV (green), XRF Core Scanner II at 2 kV (Bleu), XRF Core Scanner II at 50 kV (black). A) Comparison of the element K. B) Comparison of the element Ca. C) Comparison of the element Fe. D) Comparison of the element Sr.



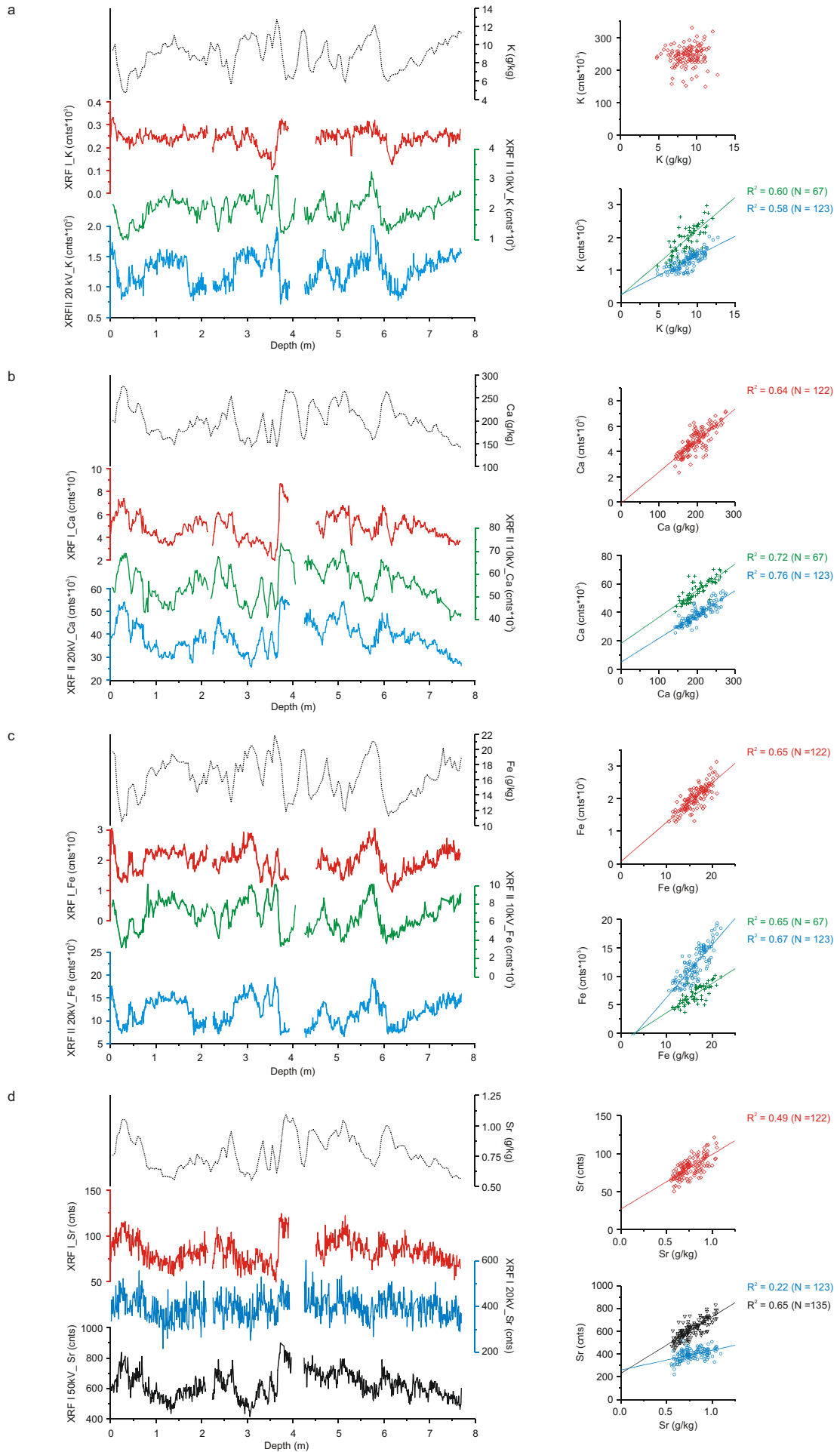


Figure 8 (previous page). Chemical analyses of sediment core GeoB7919-5 measured with ICP (black dotted line), XRF Core Scanner I (red), XRF Core Scanner II at 10 kV (green), XRF Core Scanner II at 2 kV (Bleu), XRF Core Scanner II at 50 kV (black). a) Comparison of the element K. b) Comparison of the element Ca. c) Comparison of the element Fe. d) Comparison of the element Sr. Gaps and a damaged split core surface inhibited to take XRF core scanner measurements at 2.10-2.30 m and at 3.98-4.52 m.

K accurately is less problematic for XRF scanner II due to the optimized generator settings, newer hardware components and processing software. Additionally, the Ultralene® foil used to cover the split core sections measured with XRF scanner II has an especially high transmission for lighter elements such as the element K. Different hardware components result in satisfying results for the element Sr measured at 20 kV with XRF scanner I and at 50 kV with XRF scanner II.

2.1.3 Precision of XRF Core Scanner II

The element intensities of XRF scanner measurements depend on the element concentration, the attenuation coefficient of the sample material the energy level of the X-ray source, the count time, and the X-ray hardware (Röhl and Abrams, 2000; Westerhold, 2003). The attenuation coefficient of the sample material indicates the radiation absorbing characteristics and depends on the chemical composition and the physical properties of the sample material (Tjallingii et al., *in press.*). The analytical precision of XRF scanner I was indicated by the proportional deviation from the arithmetic mean of three-fold measurements (Westerhold, 2003). Appropriately, the analytical precision of XRF scanner II was calculated as the proportional deviation (in %) of five-fold measurements for different element concretions of four sediment cores from the northwestern African Margin. These measurements were performed at 10kV (Al, Si, S, K, Ca, Ti, Fe) and at 50 kV (Rb, Sr, Zr, Ba). The analytical precision increases for higher elemental intensities in an identical manner for all elements, and show relatively little diversity between the different sediment cores (Figure 9). The 10 kV measurements indicate that the deviation become significantly larger than $\pm 10\%$ of the mean for element intensities less than ~ 1000 counts (Figure 9a and b). The element intensities of 50 kV become larger than $\pm 10\%$ for element intensities less than ~ 500 counts (Figure 9c). The absolute element intensities of the 50 kV measurements are significantly lower than the 10 kV measurements due to the application of a Cu filter during these measurements. The Cu filter reduces the background in the central part of the spectrum and, therefore, the background values increase at the edges of the spectrum (Figurer 6). However, the K_{α} spectral line of Ba (37.4 KeV) is located at the edge of the 50 kV spectrum resulting

in higher back ground values and higher analytical uncertainty (Figure 9c). The elements Ag, Sn, and Te originate as artifacts of the collimator and electronic components of the detector used in the XRF core scanner.

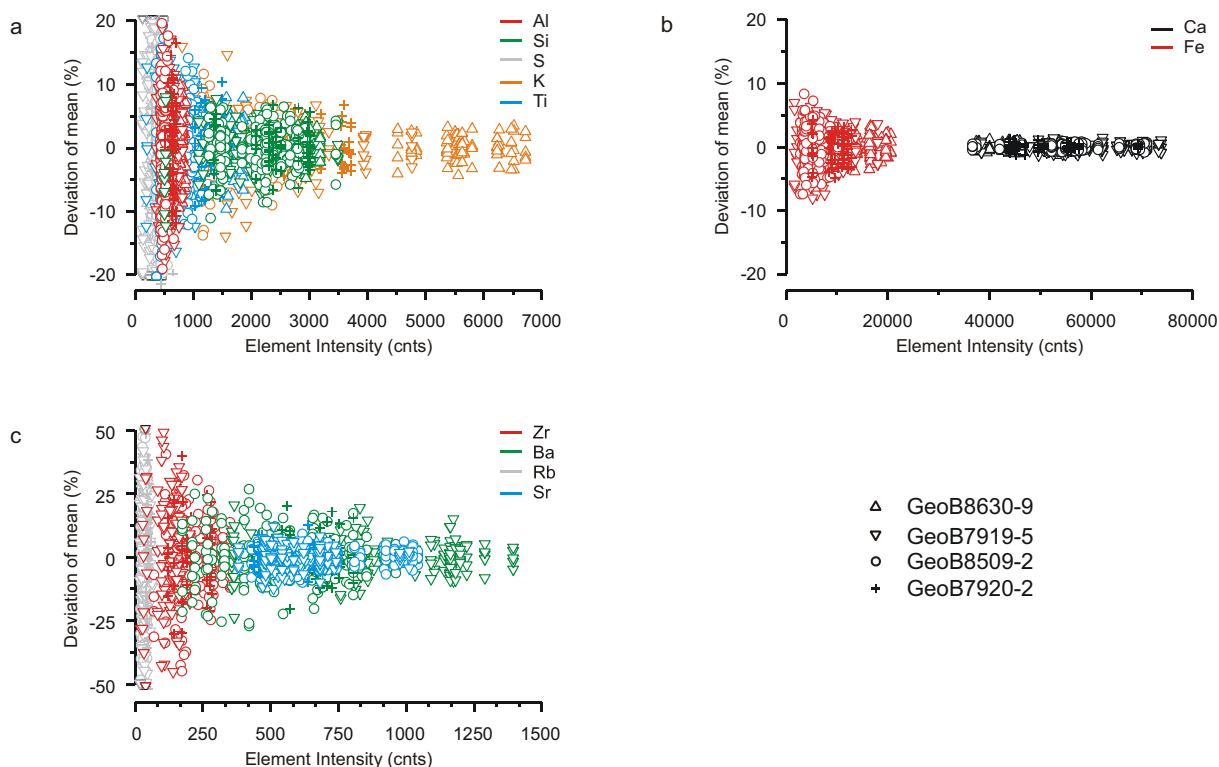


Figure 9. Analytical precision of the XRF core scanner II calculated as the proportional deviation of the mean from five-fold measurements. a) Proportional deviation of the elements Al, Si, S, K, and Ti measured at 10 kV. b) Proportional deviation of the elements Fe and Ca measured at 10 kV. c) Proportional deviation of the elements Rb, Sr, Zr, and Ba measured at 50 kV in combination with a Cu filter. The data are from late Quaternary sediment sequences on the continental margin off Cape Blanc (GeoB7919-5, GeoB7920-2, GeoB8509-2, GeoB8630-3).

2.1.4 Influence of physical properties

Variations of physical properties such as grain size or porosity affect the amount of scatter at the surface of the sediment sample and, hence, the amount of radiation received by the sample. Westerhold (2003) and Kuhlmann (2004) demonstrated this by XRF measurements of drill biscuits surrounded by a relatively dense drill mud matrix. However, it is hard to estimate the influence of grain-size variations from actual marine sediments, because strong grain-size variations are mostly attend by variations of the chemical sediment composition (e.g turbidites). Therefore, artificial sediment mixtures of loess and sieved foraminifers were used to indicate the influence of coarse-grained sediments on the quality of XRF core scanner data. Three foraminifer sieve fractions (< 150 μm , 150-212 μm , and 212-350 μm) were mixed with

loess so that each sieved fraction contained of three samples with respectively 40%, 60%, and 80 % carbonate.

As shown in Figure 10, the total element intensities, calculated as the sum of all element intensities, decline with increasing grain-sizes. Decreasing of total intensities with increasing grain size is probably related with increasing radiation scatter on rougher sediment surfaces of coarse-grained sample material. Previous studies referred to this effect as *sandpaper effect* (Jansen et al., 1998; Kuhlmann, 2004). Although, the divergence between the individual measurements of each remains relatively unaffected, the intensity differences between the three different carbonate concentrations become larger with increasing grain sizes. This suggests that sample inhomogeneities become abundant in coarse-grained sediments, which play only a minor role in fine-grained marine sediments.

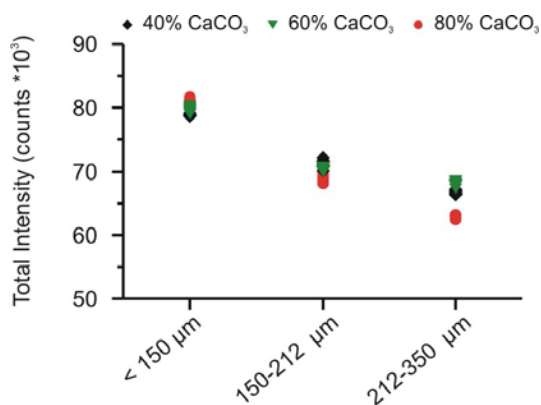


Figure 10. Total element intensities of artificially mix sediment samples. The samples contain 40, 60 and 80 % carbonate of three different grain-size fractions.

Although the XRF scanner analyses only the very upper part of the sediment, the element intensity of elements heavier than K are fairly unaffected by down-core changes of physical properties (Tjallingii et al., *in press.*, Chapter 3). However, element intensities of the lighter elements Al and Si are strongly reduced due to the formation of a thin water film between the split core surface and the Ultralene® foil that covers the sediment core during the XRF analyses. This artificially enhanced water content is reflected by the Cl intensities in marine sediments, as Cl is restricted to seawater (Tjallingii et al., *in press.*). However, the extraordinary small sample volume analyzed by the XRF core scanner and the artificially enhanced water content in the sample volume inhibits accurate calibration of the Cl intensities with standard water content measurements of discrete sediment samples.

Tjallingii et al. (*in press*) successfully corrected for the intensity loss of the elements Al and Si in sediment core GeoB7920 due to water absorption effects by using the following correction equations:

$$Al_{dry} = Al_{wet} / (-0.17 * \exp -(Cl_{wet}/11886.4)) \quad (4)$$

$$Si_{dry} = Si_{wet} / (-0,057 + 1,175 * \exp -(Cl_{wet} / 6229,95)). \quad (5)$$

Here, Al_{wet} , and Si_{wet} are the element intensities of Al and Si as measured at the split core sediment surface, and the Cl intensities are used as a proxy for the water content in the sample volume analyzed by the XRF scanner. However, application of these functions as a correction model to any sediment core measured with the XRF core scanner will further increase the significance of this method. Therefore, these correction functions were applied to sediment cores GeoB7919 and GeoB8630 (Figure 11 and 12). The XRF cores scanner analyses are calibrated with chemical analyses on discrete samples performed on a Spectro Xepos EDPXRF.

The corrected Al intensities calculated from equation 4 improves the correlation coefficient (R^2) for core GeoB7919, but not for core GeoB8630 (Figure 11). The Al concentrations in core GeoB8630 are relatively low, and the concentration variations are relatively small compared to these in the other sediment cores. The corrected Si intensities calculated from equation 5 improves the correlation coefficient (R^2) for the Si measurements of cores GeoB7919 and GeoB8630 (Figure 12). Although the correction equations 4 and 5 are subject to considerable scatter, the water correction equations obtained from GeoB7920

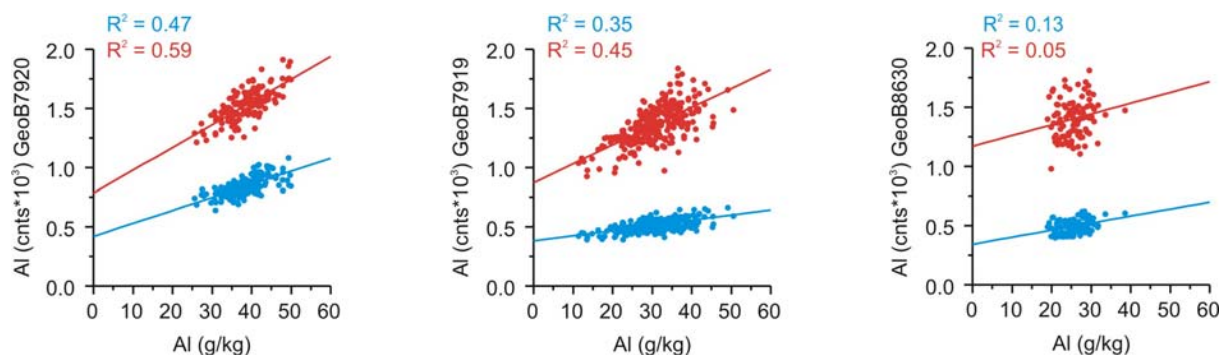


Figure 11. Comparison of XRF core scanner measurements taken at the split core surface (blue) and the element intensities as calculated with the water correction functions obtained from core GeoB7920 (red) for the element Al of sediment cores GeoB7920 (N = 162), GeoB7919 (N = 273), and GeoB8630 (N = 103). The XRF measurements are calibrated with conventional sample XRF analyses (Spectro Xepos).*

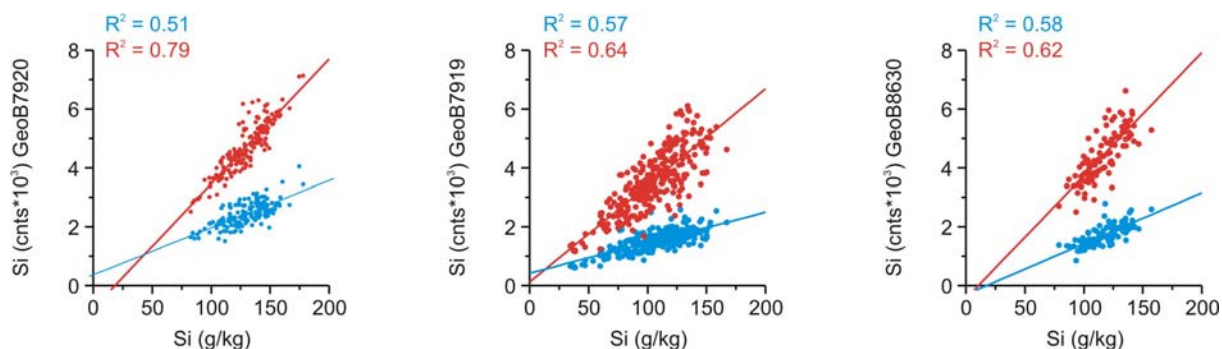


Figure 12. Comparison of XRF core scanner measurements taken at the split core surface (blue), and the element intensities as calculated with the water correction functions obtained from core GeoB7920 (red) for the element Si of sediment cores GeoB7920 (N = 162), GeoB7919 (N = 273), and GeoB8630 (N = 103).*

*[Conventional sample XRF data of core GeoB8630 (Schulz & Kölling, unpublished). Conventional sample XRF data of core GeoB7919 (Wien et al., 2006).]

(Tjallingii et al., (in press.), Chapter 3) seems to improve the correlation coefficient for other sediment cores off Cape Blanc as well. However, limited variations of the element concentration in the sediment core restrain accurate estimation of linear correlation, and resulting in insignificant correlation coefficients.

2.1.5 Spectro Xepos EDPXRF analyzes

Chemical analyses on discrete samples performed on a Spectro Xepos EDPXRF at the geochemistry department of the University of Bremen are used for calibration of XRF Core Scanner data. The Spectro Xepos EDPXRF analyzes the absolute element concentrations (g/kg) from Magnesium (Mg, atomic number 12) through U (uranium, atomic number 92) of discrete sediments samples. The element concentration obtained by the XRF sample analyzer correlate well with these of ICP-AES analyses (Wien et al., 2005). The sediment samples are prepared with approximately 4 g of freeze-dried and ground sample material, loosely packed in a sample cup, which is covered with a 4 µm thick prolene foil. Additionally, a foam plug filled up the remaining open space in the sample cup to fix sample material in the sample cup. Grinding the sediment to a powder and the relatively large amount of sample material ensure a representative and homogenous sediment sample. The XRF sample analyzer also provides the sediment mass attenuation coefficient (MAC) for every sample that indicates the radiation absorbing properties of the sediment sample. The XRF sample analyses are ideal for calibration of the XRF core scanner II measurements since both methods use the same analytical principle and cover the same elemental range. However, the XRF sample analyzer measures dry and homogenized powder samples, whereas the XRF core scanner analyses the

sediment surface of split core archive half. For detailed technical specifications of the Spectro Xepos EDPXRF analyzer see *Wien et al. (2005)*.

2.2 Grain size analysis and the End-Member Modeling Algorithm

The terrigenous sediment fraction can be considered as a mixture of sediment populations that can be ascribed to different sediment-transport mechanisms (e.g., *Weltje and Prins, 2003*). As these transport mechanisms have a strong imprint on the grain-size distributions of the carried sediment fraction through selective transport, the grain size provides a powerful tool to distinguish variations in the transport mechanisms, which are ultimately related to climate variability.

Approximately 0.5 ml of bulk sediment was used to isolate the terrigenous sediment fraction from for grain-size analyses. Carbonate, organic carbon, and biogenic silica were removed with excess HCl, H₂O₂, and NaOH, respectively, and neutralized after every treatment. First, 100 ml demineralized water and 15 ml HCl were added to the sediment sample in order to dissolve the carbonate. The mixture was boiled for 1 min to speed up the reaction and neutralized afterwards by adding approximately 1 liter of demineralized water. The sample settled down over 24 hours after which the excess was decanted. Second, the organic matter was dissolved by adding 10 ml H₂O₂ and heating the sample until the effervesce reaction stopped. Again, the sample was neutralized by adding approximately 1 liter of demineralized water and settled down over 24 hours after which the excess was decanted. Third, approximately 6 g NaOH and 100 ml demineralized water was added to the sample and boiled for 5 minutes to dissolve the biogenic opal. Afterwards, the samples were neutralized twice with 1 liter of demineralized water. Random microscope observations were obtained to crosscheck the removal of all biogenic constituents. Finally, each sample was boiled with ~300 mg of Na₄P₂O₇·10H₂O before measuring to avoid the formation of aggregates. The grain-size distribution of the isolated lithogenic sediment fractions were measured with the Coulter Laser Particle Sizer (LS200) that measures particles in the range from 0.4 to 2000 μm in 92 size classes. All measurements were performed with degassed water to minimize the effect of air bubbles and repeated 3 to 8 times to ensure reproducible results.

Statistically evident grain-size populations were calculated from the grain-size measurements with the end-member-modeling algorithm of *Weltje (1997)*. As stated by e.g., *Weltje and Prins (2003)*, the end-member-modeling algorithm is able to derive a mixing

model from a series of compositions solely based on co-variant structures in the modeled matrix and showing the following characteristics:

- The size distribution of the end members may contain negative proportions (actually the only specification prescribed for the end members).
- The observed compositional variation reflects linear mixing or an analogous process with a superimposed measurement error.
- There are no restrictions related to the shape of the end-member size distributions.
- The end members are allowed to show overlap between the respective size distributions.
- The end members are linearly independent, i.e. none of the end members can be expressed as a mixture of the other end members

The minimum number of dimensions, or end members, required for a satisfactory approximation of the data was established by calculation of the coefficient of determination (Prins and Weltje, 1999). The coefficients of determination represent the proportions of the variance of each variable that can be reproduced by the approximated data. This proportion is equal to the squared correlation coefficient (r^2) of the input variables and their approximated values (see also chapter 4, figure 5a). The squared correlation coefficients are repeatedly calculated for models with 1 to 10 end members. The goodness of fit is indicated by the distribution of the coefficients of determination across the grain-size classes for different numbers of end members. Additionally, the mean coefficient of determination (r^2_{mean}) across the grain-size classes increases when the number of end members is increased (see also chapter 4, Figure 5b). In general, the number of end members is determined by the best reproducibility on one hand, and a minimal number of end members on the other hand.

2.3 Analyses of carbonate, organic carbon, opal, and terrigenous matter

The amounts of carbonate, organic carbon, and opal as main sediment constituents are all measured from a small part of the freeze-dried and ground bulk sediment samples. The carbon concentration is measured on 25 μg sediment of sediment with the Elementar Vario EL 3 CHN analyzer. These analyses were performed of both bulk sediment samples and carbonate free samples. Dissolving calcium carbonate (CaCO_3) with HCl (1M) before analyzing allows one to measure the organic carbon concentration. The carbonate concentration is calculated after subtracting the organic carbon concentration from the total carbon concentration measured on the bulk sediment samples. Biogenic opal concentrations are measured from a

proportion (~ 4 mg) of bulk sediment by the automated leaching method of *Müller and Schneider* (1993). The lithogenic content was calculated as the residual sediment fraction of the sediment free of carbonate, organic matter, and biogenic opal.

2.4 Physical properties

The wet bulk density (WBD) and the salt corrected dry bulk density (DBD) were calculated from syringe sample as stated by Weber et al (1997). These physical properties were calculated from syringe volume (V_W), the wet mass (M_T), and the freeze-dried mass (M_D). The mass of the salt (M_S) was estimated from the mass of the water content (M_W) and the salinity ($S = 35\%$) according to:

$$M_W = M_T - M_D \quad \text{and} \quad M_S = M_W * S / (1-S) \quad (6)$$

Assuming the salt density is 2.1 g/cm^3 , the water content (in %), the WBD, and the DBD (in g/cm^3) can be calculated as:

$$\text{Water content} = (M_T - M_D) / M_T * 100 \quad (7)$$

$$\text{WBD} = (M_T - M_S) / (V_T - (M_S / 2.1)) \quad (8)$$

$$\text{DBD} = (M_D - M_S) / (V_T - (M_S / 2.1)) \quad (9)$$

2.5 Stable isotope stratigraphy

The stable isotopic stratigraphy was constructed from the epibenthic foraminifer species *Cibicidoides wuellerstorfi*. Syringe samples (~10ml) were freeze-dried, weighed and washed over a $150 \mu\text{m}$ and a $63 \mu\text{m}$ mesh sieve and dried at 50°C . Two to five specimens of the washed fraction $> 250 \mu\text{m}$ were picked for isotope analyses. The foraminifers were analyzed on a Finnigan MAT 252 micro-mass spectrometer coupled to a Finnigan automated carbonate device at the MARUM institute, University of Bremen. The samples were solved in orthophosphoric acid at 75°C and measured with a precision of $\pm 0.07\%$ for $\delta^{18}\text{O}$ and $\pm 0.05\%$ $\delta^{13}\text{C}$ compared to an internal laboratory standard. The international standard NIST 19 was used to convert the stable oxygen values to the VPDB-scale. The benthic stable isotope records are expressed with the δ notation:

$$\delta^{18}\text{O}_{\text{Sample}} = \frac{[(^{18}\text{O}/^{16}\text{O})_{\text{Sample}} - (^{18}\text{O}/^{16}\text{O})_{\text{Standard}}]}{(^{18}\text{O}/^{16}\text{O})_{\text{Standard}}} \times 1000 \quad (10)$$

$$\delta^{13}\text{C}_{\text{Sample}} = \frac{[(^{13}\text{C}/^{12}\text{C})_{\text{Sample}} - (^{13}\text{C}/^{12}\text{C})_{\text{Standard}}]}{(^{13}\text{C}/^{12}\text{C})_{\text{Standard}}} \times 1000 \quad (11)$$

- Chapter 3 -

Influence of the water content on X-ray fluorescence core scanning measurements in soft marine sediments

Rik Tjallingii¹, Ursula Röhl¹, Martin Kölling², and Torsten Bickert¹

¹*Research Center for Ocean Margins, University of Bremen, 28354 Bremen, Germany*

²*Department of Geosciences, University of Bremen, 28354 Bremen*

Accepted for publication in Geochemistry, Geophysics, Geosystems (G³)

Abstract.

The X-ray fluorescence (XRF) core scanner provides bulk-sediment chemistry data measured non-destructively at the split core sediment surface. Although this method is widely accepted, there is little known about the effects of physical properties such as density and water content on XRF core scanner data. Comparison of XRF scanner measurements from the sediment surface and dry powder samples of sediment core GeoB7920 indicate strongly reduced element intensities for the lighter elements Al and Si. We relate the lower element intensities of the measurements taken at the sediment surface to the amount of water in the sample volume analyzed by the XRF core scanner. The heavier elements K, Ca, Ti, and Fe remain relatively unaffected by the variation of any physical property within sediment core GeoB7920. Additionally, we successfully use the elemental intensity of Cl as a proxy for the seawater content in the sample volume analyzed by the XRF core scanner. This enables the establishment of a correction function for the elements Al and Si that corrects for the radiation absorption of the water content in sediment core GeoB7920 off Cape Blanc, NW Africa.

Keywords: X-ray fluorescence, XRF core scanner, physical properties, sediment chemistry, interstitial water, seawater.

1 Introduction

The Avaatech X-ray Fluorescence (XRF) core scanner is a computer-controlled core-scanning tool that analyzes the chemical composition of sediments directly at the surface of a split sediment core. The XRF core scanner allows non-destructive, nearly continuous, and relatively fast analysis of the elements from Aluminum (Al, atomic number 13) through to Uranium (U, atomic number 92) (Richter et al., 2006). Detailed XRF core scans have already successfully been used for high-resolution time series, stratigraphic correlations, and detailed sedimentary and climatic reconstructions on various time scales (e.g. Bahr et al., 2005; Grützner et al., 2005; Haug et al., 2001; Hepp et al., 2006; Jaccard et al., 2005; Kuhlmann et al., 2004; Lamy et al., 2001; Röhl et al., 2001; Westerhold et al., 2005)

The XRF scanner measures the chemical composition of the sediment as element intensities in total counts (cnts) or counts per second (cps), which are proportional to the chemical concentrations. Although element intensities mainly depend on the element concentration, they are also influenced by the energy level of the X-ray source, the count time, and the physical properties of the sediment (Röhl and Abrams, 2000). Conventional XRF analyzers use dry and homogenized powder samples in order to avoid interference of sample inhomogeneities or physical variations. However, down-core varying physical properties can be an issue for XRF core scanner analyzes that are obtained directly at the split core surface.

Mineral heterogeneities and surface roughness effects are minimized by the relatively large irradiated area (1 cm^2) of the core scanner for fine-grained sediments (Ge et al., 2005; Jansen et al., 1998). However, in particular sandy sediments bring about surface roughness and mineral inhomogeneities effects due to enhanced radiation scatter at the sample surface (Jansen et al., 1998; Richter et al., 2006). Additionally, there are indications that the XRF core scanner data are dependant on changes in density and porosity although these are not quantified. For instance, XRF measurements on drill biscuits of carbonate (CaCO_3) rich sediments demonstrated significantly lower element intensities compared to the relatively denser drill mud matrix surrounding the biscuits (Kuhlmann, 2004; Westerhold, 2003). Radiation absorption and scatter of water in natural rocks, soils and sediments could also cause influence XRF measurements (Ge et al., 2005; Koshikawa et al., 2003). Recent studies with an XRF microscanner indicated that the cohesive and adhesive properties of the interstitial water forms a water film directly under the foil covering the sediment. The water film artificially increases water content in the sample volume analyzed by the XRF scanner

and has an especially strong effect on the lighter elements Al and Silicon (Si, atomic number = 14) (Kido et al., 2006).

The ionization energy and the characteristic fluorescence energy increase with the square of the atomic number as stated by Moseley's law (Moseley, 1914). Additionally, weaker fluorescence energies are more susceptible to scatter and absorption effects (Potts, 1987). Consequently, the penetration depth of the fluorescence radiation, or critical depth, is $\sim 8 \mu\text{m}$ for Al, $\sim 36 \mu\text{m}$ for Calcium (Ca, atomic number 20), and $\sim 180 \mu\text{m}$ for Iron (Fe, atomic number = 26) (Figure 1) (Potts, 1987). The radiation absorption characteristics of the sample material are indicated by the mass attenuation coefficient and depend on the chemical composition and the physical properties (Jenkins and de Vries, 1970; Potts, 1987). For multi-component materials, the mass attenuation coefficient is calculated as the sum of the single contributions of all elements proportional to their elemental mass fraction (Potts, 1987). The Lambert-Beer law, which states that equal path lengths of the same material absorb the same fraction of intensity, describes radiation attenuation. Accordingly, the transmission (T) describes the intensity loss of an X-ray beam as it penetrates matter by an exponential function:

$$T(x) = I_x/I_0 = \exp^{-(\alpha x)}$$

The transmission quantifies the intensity attenuation for a given element over path length (x) expressed in terms of the initial intensity (I_0) and the residual intensity (I_x) and the mass attenuation coefficient (α) of the sample material.

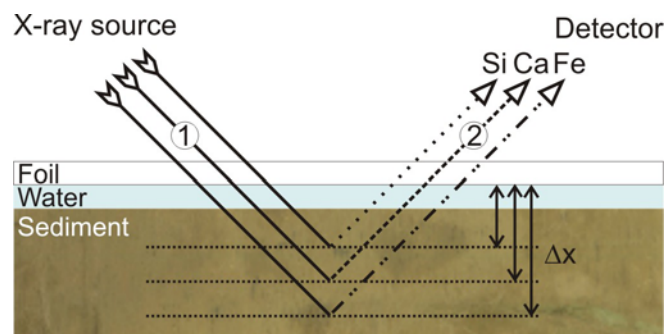


Figure 1. Excitation geometry of the X-ray fluorescence analysis of the elements Si, Ca and Fe by the XRF core scanner (not on scale) (Richter et al., 2006). Elements in the sediment are ionized by the primary X-rays (1), and emit an element specific fluorescence radiation (2), which is registered by the detector. Heavier elements emit stronger fluorescence energy resulting in a larger critical depth (Δx). A thin water film is formed directly under the foil that covers the split core sediment surface due to the cohesive and adhesive properties of water. This water film will be proportional thicker for the lighter elements with a relatively small critical depth than for heavier elements with a relatively large critical depth.

The objective of this study is to investigate and estimate the influence of down-core changes of the physical properties on XRF core scanner measurements. Therefore, we compare XRF core scanner analyses of the split core sediment and on discrete homogenized samples used for conventional XRF measurements. We focus on the effects for the total intensity and on the individual element intensities of the elements from Al through to Fe in marine sediment core GeoB7920 off Cape Blanc, NW Africa.

2 Material and Methods

Sediment core GeoB7920 (20°45.1' N, 18°34.9' W) is a 16.18 m long core that was retrieved from a water depth of 2278 m during Meteor expedition M53/1 off Cape Blanc, NW Africa (Figure 2) (Meggers et al., 2002). Accumulation rates are relatively high in this area due to high surface water productivity and relatively large amounts of eolian dust transported into the area from the Saharan desert and Sahelian region (deMenocal et al., 2000; Matthewson et al., 1995; Stuut et al., 2005; Tiedemann et al., 1989). The pelagic sediments of core GeoB7920 mainly consist of calcium carbonate (CaCO₃) and lithogenic material, both approximately 35 - 70 % of the proportional weight, and relatively small amounts of organic matter (<3%), and opal (<3.5 %).

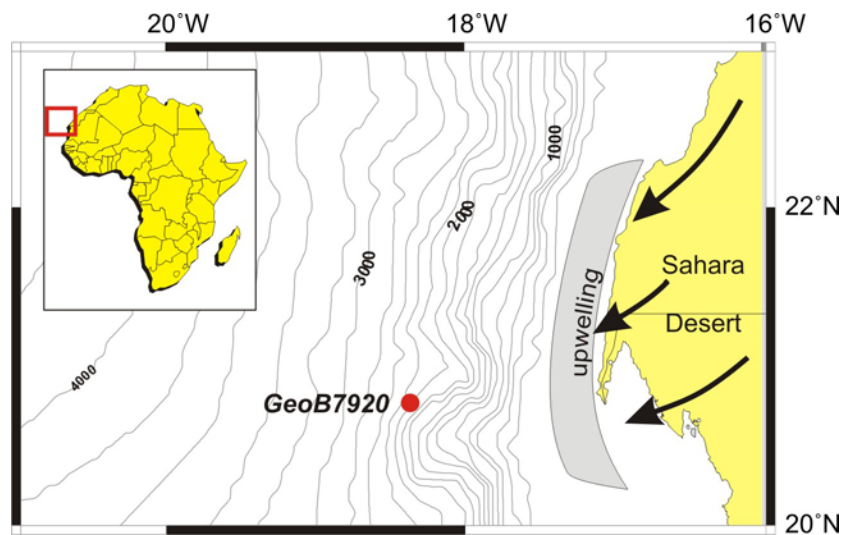


Figure 2. Location of core GeoB7920 and the regional settings off Cape Blanc, NW Africa. The NE trade winds (black arrows) transport large amounts of wind-blown dust from the Saharan Desert into the study area (Stuut et al., 2005). Year round wind-induced upwelling occurs over the continental shelf, indicated by the shaded area resulting in high surface water productivity over the core location (Helmke et al., 2005).

The XRF core scanning measurements were obtained directly at the split core surface of the archive half with the Avaatech XRF core scanner at the University of Bremen. The split core surface has to be covered with a 4 μm thin SPEXCerti Prep Ultralene® foil to avoid contamination of the XRF measurement unit and desiccation of the sediment. This foil has a high transmission for the relatively weak K_{α} fluorescence energies of the lighter elements Al (88%), Si (92%), and Chlorine (Cl, atomic number 17) (98%) and has a complete transmission for all elements heavier than Cl (Figure 3). The XRF radiation passes through three foils between the sediment and the detector; the first covers the sediment surface, the second and the third foil cover the He-flush prism (Figure 3b). The He-flushed prism forms a pseudo vacuum transmission medium between the X-ray source, the sediment, and the detector. The initial element intensities (I_1) of the elements Al, Si, and Cl were calculated from the transmission of the Ultralene foil and the residual element intensity (I_4) recorded by the detector (Figure 3). Maximum quality of the XRF measurements demands a smoothly equalized sediment surface, no air bubbles under the foil, and no wrinkles in the foil. All XRF scanner measurements were carried out with a generator setting of 10 kV and a sampling time of 30 seconds to obtain the element intensities from Al through to Fe. The dimensions of the irradiated sediment surface are 1 cm x 1 cm, but can be changed for higher sample resolutions (down to 0.2 cm x 1 cm). Technical and practical details about the XRF core scanner are described in Richter et al. (2006) and on <http://www.avaatech.com>.

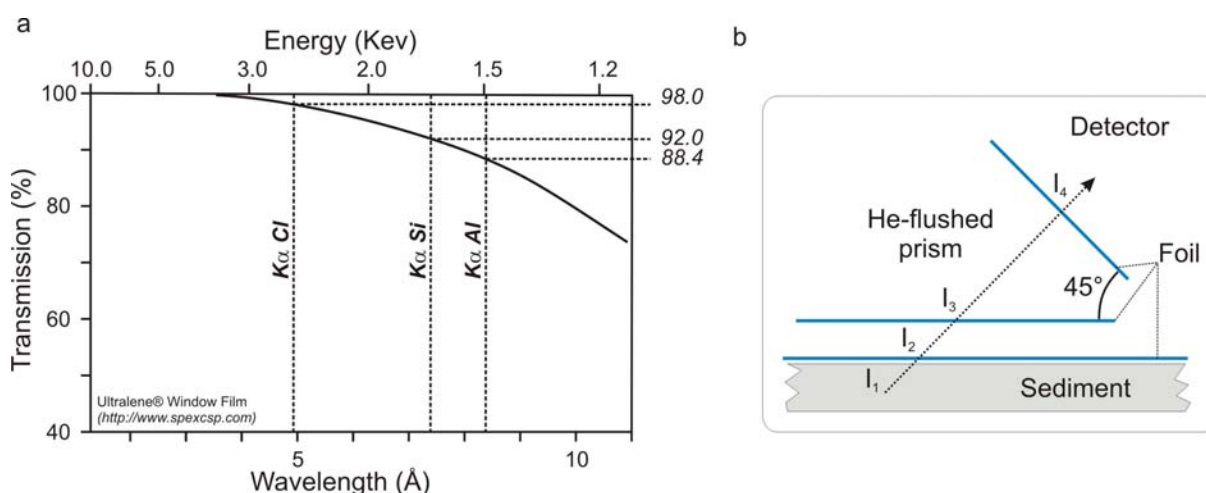


Figure 3. Transmission properties of the Ultralene® foil used for the XRF core scanner analyses, and the K_{α} fluorescence energies of elements Al, Si, and Cl. A. The foil is transparent for all elements with K_{α} energies larger than ~ 3 KeV, or a wavelength smaller than ~ 4 Å, corresponding to the elements heavier than Chlorine (Cl, atomic number 17, $K_{\alpha} = 2.62$ KeV). B. The X-ray fluorescence radiation passes through three layers of foil on its way from the sediment to the detector. From the initial intensity (I_1) of the elements Al, Si, and Cl transmitted from the sediment remains the residual intensity (I_4) due to the transmission of the foil.

The quality of the element intensities of the XRF core scanner was validated with chemical data of a conventional XRF analyzer (Spectro Xepos EDPXRF). The conventional XRF analyzer measures the elemental concentration from Magnesium (Mg, atomic number 12) through to Barium (Ba, atomic number 56) in g/kg and provides the sediment mass attenuation coefficient of every sample in cm^2/g (Wien et al., 2005). This XRF analyzer measures loosely packed powder samples (~ 4 g) prepared from freeze-dried and ground sediment (Wien et al., 2005). The chemical element concentrations were determined with a sample resolution of 10 cm (164 samples in total).

The sum of all element intensities (I_{total}) was compared with the carbonate content, wet bulk density (WBD), grain-size variations, and the mass attenuation coefficient of dry powder samples to indicate the influence of down-core physical and compositional variations. The sample volume, the wet mass and the freeze-dried mass were measured to calculate the WBD (Weber et al., 1997). The carbonate content was determined from CHN elemental analyses of approximately 25 mg dried and ground sample material. The proportional weight of the sediment fractions, $<63 \mu\text{m}$, $63\text{-}150 \mu\text{m}$, and $>150 \mu\text{m}$ were obtained by the wet sieving of bulk sediment samples. These measurements were carried out every 10 cm on 10 ml syringe samples (164 samples in total).

The influence of physical properties on individual element intensities was investigated by comparing measurements XRF measurements taken at the split core surface (*wet samples*) and from dried and homogenized powder samples (*dry samples*) with conventional XRF measurement. The XRF core scanner analyses of the wet sample measurements were carried out every 2 cm. The dry samples measured with the XRF core scanner are exactly the same samples as prepared for the conventional XRF analyzer. We assume that the XRF measurements of the dry and homogeneous powder samples are not influenced by variations of physical properties. Subsequently, we consider the element intensity of the dry sample measurements as the initial intensity, and use the ratio of the wet and dry sample measurements to indicate the transmission related to physical properties. However, the small sample volume analyzed by the XRF scanner and the formation of a water film directly under the foil (Figure 1) inhibits accurate calibration of physical properties measured from 10 ml syringe samples. We use the Cl intensity measured by the XRF scanner as a proxy for the water content in the volume analyzed by the XRF scanner, since the interstitial water consists of seawater and Cl is predominantly restricted seawater. Hence, the radiation transmission by the water content in the sample volume can be indicated by the ratio of wet and dry element intensities and the Cl intensity.

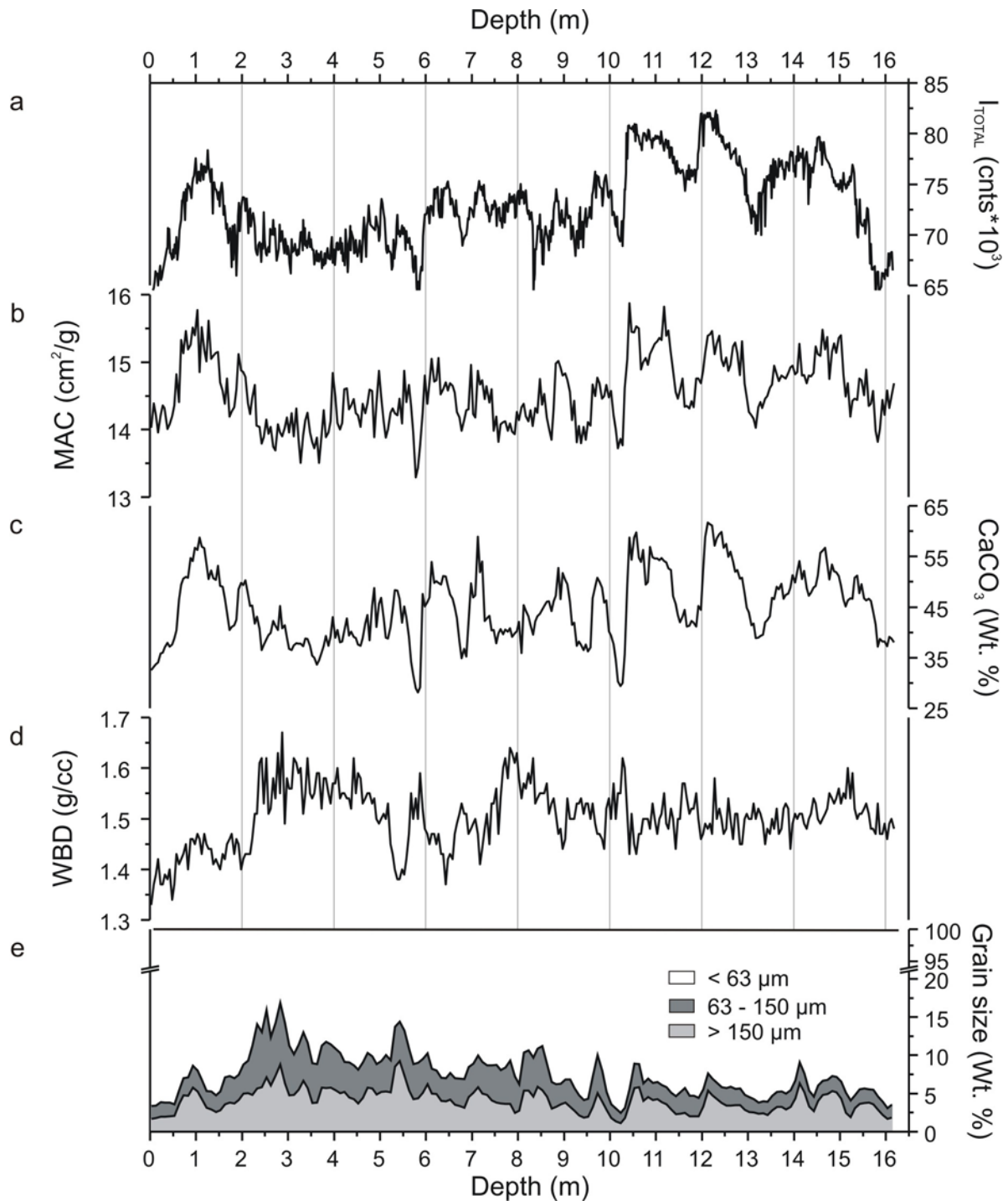


Figure 4. Down-core variation of physical and chemical sediment properties of core GeoB7920. A. Total intensity (I_{total}) calculated as the sum of all elements intensities measured by the XRF core scanner. B. Sediment mass attenuation coefficient (MAC) derived from conventional XRF analyses. C. Major sediment compositional variations indicated by the carbonate content (CaCO_3). D. Major physical sediment variations indicated by wet bulk density (WBD). E. Proportional variations of the grain-size fractions $<63 \mu\text{m}$, $36\text{-}150 \mu\text{m}$, and $>150 \mu\text{m}$. I_{total} and MAC correlate much better with the carbonate content than with the WBD. I_{total} seems to be unaffected by the sediment grain-size variations.

The element intensity of the XRF core scanner measurements depends on the element concentration, but also on the core lithology and the hardware settings (e.g. count time) (Röhl and Abrams, 2000). The analytical precision of XRF analyses varies with the element intensity (Ramsey et al., 1995), and can be indicated as the deviation of the mean of five-fold measurements (Westerhold, 2003). These five-fold measurements were repeated at different positions of core GeoB7920 to ensure a variety of element intensities.

3 Results and Interpretation

In order to distinguish between the influence of down-core chemical and physical changes, we compared the sum of all element intensities (I_{total}) with the carbonate content, WBD, and sand-size fraction of the bulk sediment (Figure 4). We assume that the total intensity describes the down-core radiation attenuation of the wet samples. This assumption is supported by the good down-core correlation of the mass attenuation coefficient data measured on dry samples measured and the conventional XRF analyzer and the total intensity measured on wet samples (Figure 4a-b). The carbonate content is used to indicate the down-core variations of the chemical composition since carbonate content CaCO_3 is the dominant chemical component in the sediment core (~30-60 Wt. %) (Figure 4c). Variations of the WBD and grains-size fractions are used to indicate the down-core changes of physical properties (Figure 4d and e). Variations of the total intensity correlate much better with the variations of the carbonate content than with WBD variations or grains-size variations (Figure 4). Therefore, the chemical composition seems to dominate the sediment radiation absorption characteristics and the total fluorescence radiation in the relatively fine-grained sediment core GeoB7920.

The influence of physical properties on individual element intensities is studied by comparison of wet sample measurements, dry sample measurements and conventional XRF measurements (Figure 5 and 6). The element intensities of the elements Al and Si are much higher for the dry sample measurements, and have much better correlation coefficients (R^2) when compared with conventional XRF analyses (Figure 5). Since the element Cl is predominantly restricted to seawater in soft marine sediments, the higher Cl intensities in the wet sample measurements are related to the artificially elevated seawater content due to the formation of a water film directly under the foil. Thus, we use the Cl intensities of the wet sample measurements as a proxy for the water content in the sample volume analyzed by the XRF. The gradual down-core decrease of the Cl intensity is interpreted as the loss of interstitial seawater and porosity due to down-core sediment compaction. As shown in Figure 5b, the correlation coefficient for Cl is better for the dry sample measurements because these

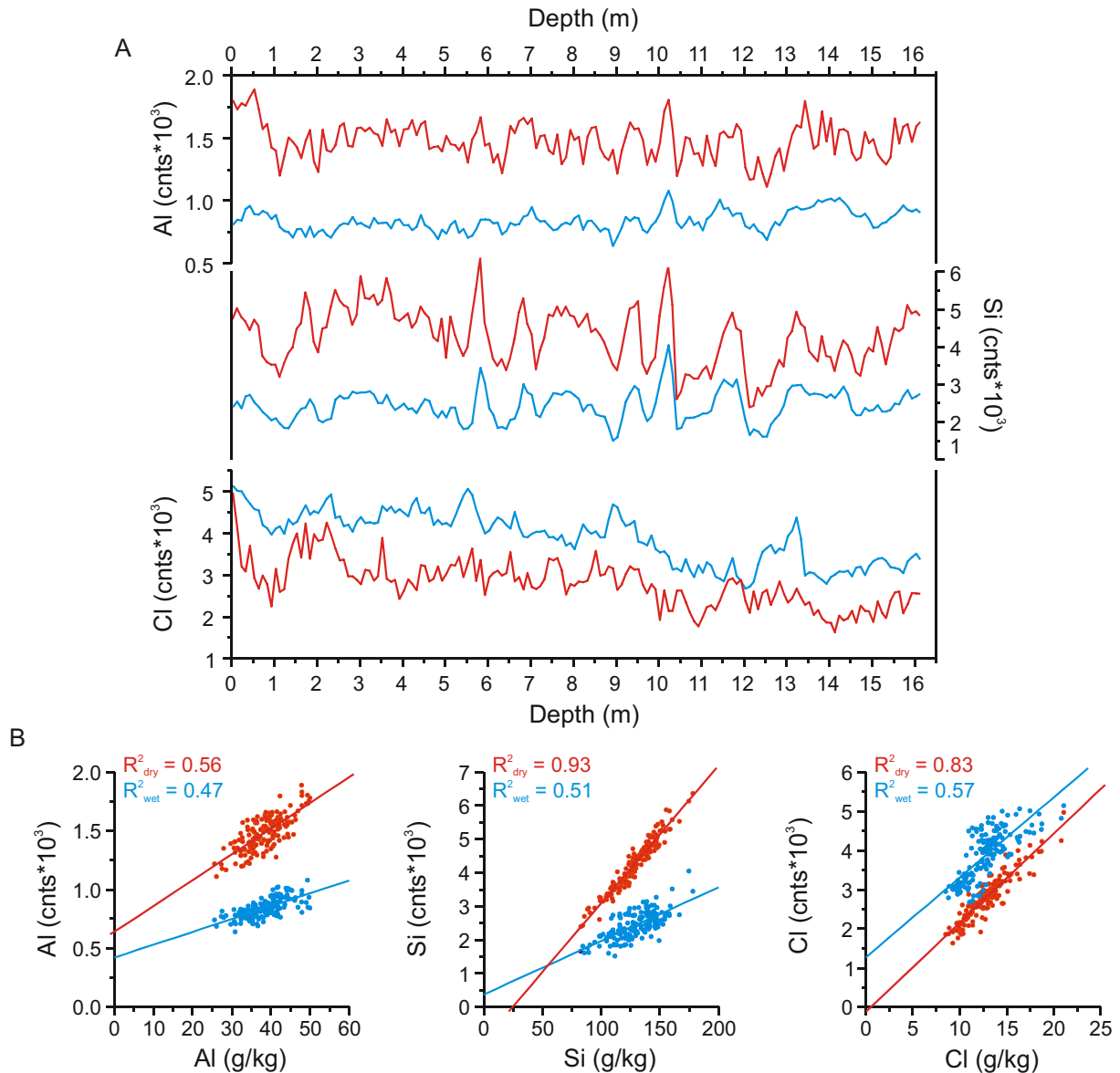
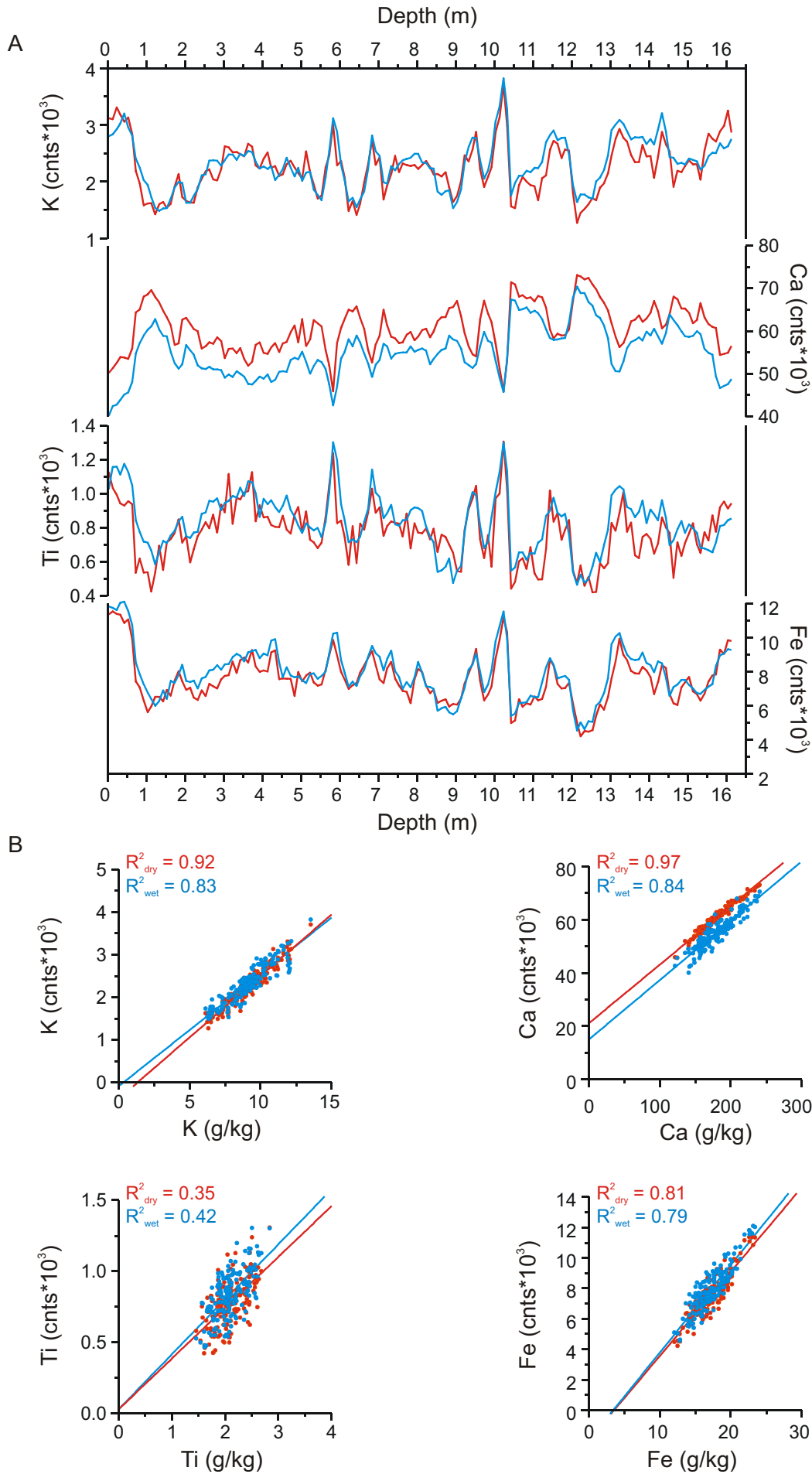


Figure 5. Comparison of wet sample measurements (blue), dry samples measurements (red) for the elements Al, Si, and Cl. A. The intensities of the elements Al and Si are much higher for dry sample measurements than for wet sample measurements. The element intensities of Cl are higher for the wet sample measurements. B. The calibration with chemical concentrations of the conventional XRF analyses shows significantly higher correlation coefficients (R^2) for the dry powder measurements than for the measurements at the sediment surface ($N = 164$).

Figure 6 (next page). Comparison wet sample measurements (blue) and dry sample measurements (red) of the elements K, Ca, Ti and Fe. A. The wet sample measurements of the elements K, Ti and Fe are comparable to the dry sample measurements. The element intensities of Ca are slightly higher for the dry sample measurements. B. The correlation coefficient (R^2) does not differ much between the wet and the dry sample measurements compared to chemical concentrations of the conventional XRF analyses ($N = 164$).



are the same samples that were used for the conventional XRF analyzer. The wet and dry sample measurements for the elements K, Ca, Ti and Fe are in good agreement (Figure 6). The good agreement between wet and dry sample measurements suggests that sample inhomogeneity effects play only a minor role in the samples used in this study. However, the slightly higher Ca intensities and reduced scatter on the regression of the dry sample measurements are related to grinding of the foraminifera shells in dry samples. The artificially enhanced water content in the wet samples strongly reduces the lighter elements whereas the heavier element intensities remain relatively unaffected.

We focus on the element intensity differences of the elements Al and Si, which show the largest difference between wet and dry sample measurements. Comparison of the dry and wet element ratios, and the Cl intensities has been used to define the transmission by the water content for the elements Al and Si (Figure 7). According to the Beer-Lambert law, the dry and wet element ratios and the Cl intensities follow an exponential attenuation function. The scatter around the regressions is related to analytical precision of the elements Al, Si, and Cl, and should therefore be considered both in the x and in the y dimension of the regression plots. Most likely, the lower correlation coefficient for the element Al than for Si (Figure 7) is related to the lower element intensities and larger analytical uncertainty of the Al intensities (Figure 8). The analytical precision of the elements Al, Si, and Cl measured by the XRF core scanner is estimated over an entire range of concentrations since the precision varies with element concentration (Ramsey et al., 1995). The slightly elevated analytical uncertainty of

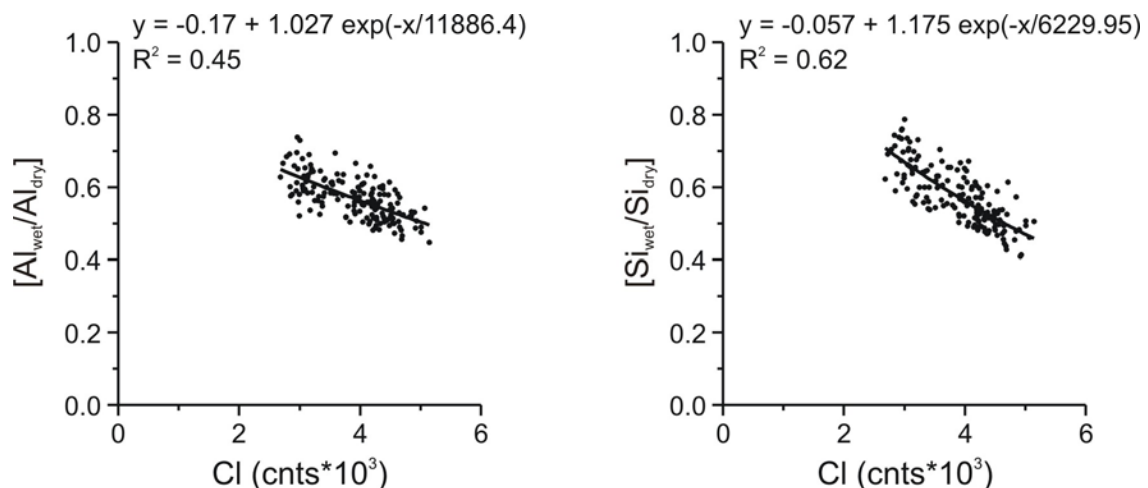


Figure 7. Regression plots showing the exponential attenuation function between the Cl intensity (x-axis) and the wet-dry intensity ratio of Al and Si (y-axis). The Cl intensity reflects the water content in the sample volume analyzed by the XRF scanner. The wet-dry intensity ratios of Al and Si indicate the radiation transmission as stated by the Beer-Lambert law. The correlation coefficients indicate an acceptable correlation between the Cl intensities in the wet samples and the transmission of the elements Al and Si.

Cl, with respect to its high element intensities, is related to the interference of Rh spectral lines emitted by the XRF source.

The exponential attenuation functions of Figure 7 enable the prediction of dry sample intensities for the elements Al and Si from their wet sample intensities and the Cl intensity. The predicted element intensities for Al and Si correlate well with the dry sample measurements (Figure 9a), and significantly improve the correlation coefficients with the conventional XRF analyses (Figure 9b). The good match between predicted and dry sample intensities indicates that the Cl intensities of the wet sample measurements give a good estimate of the water content in the sample volume analyzed by the XRF core scanner. Also, the water content accounts for the largest influences on the XRF measurements of the lighter elements Al and Si. The differences between the predicted element intensities and the dry sample measurements can be related to the analytical uncertainties of the XRF scanner and sample inhomogeneities.

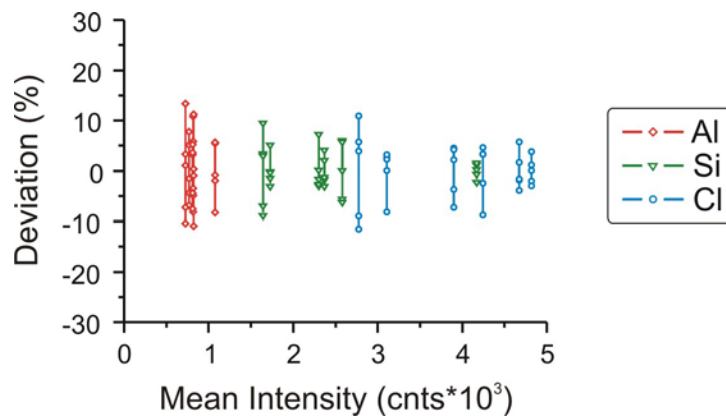


Figure 8. Analytical precision of the elements Al, Si and Cl for the wet sample measurements of core GeoB7920. The precision is indicated by the proportional deviation of 5-fold measurements and improves with increasing element intensity. The proportional deviations of replicate measurements decrease from approximately $\pm 10\%$ to $< \pm 5\%$ with increasing mean intensities for the elements Al and Si. The deviation variations of Cl are relatively large with respect to the high mean element intensities because of the interference of the Rh spectral lines from the X-ray source.

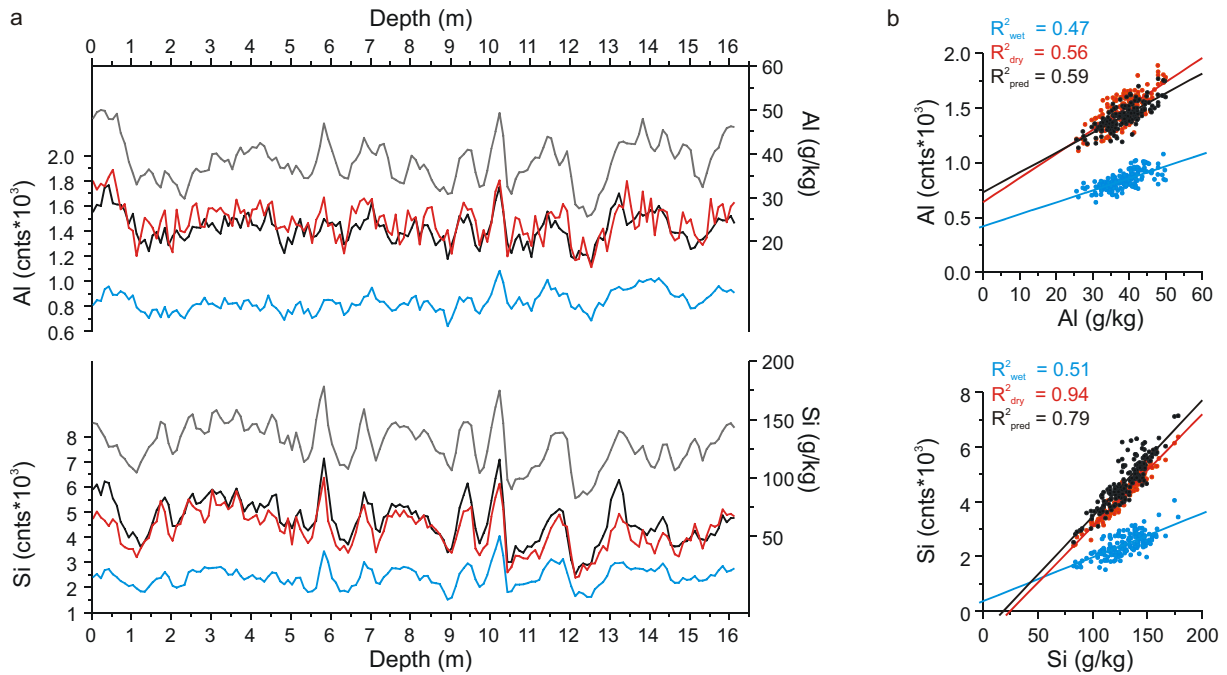


Figure 9. Comparing the quality of wet sample intensities (blue), dry sample intensities (red), and water corrected intensities (black) for the elements Al and Si measured with the XRF core scanner. A. The predicted element intensities of Al and Si are consistent with down-core variations of the dry sample intensities. B. The water corrected element intensities improve the correlation coefficients (R^2) significantly and compromise the regression lines of the dry sample measurements.

4 Discussion

Although the WBD and the sediment composition are not completely independent of each other, changes in the CaCO_3 content influence the total intensity recorded by the XRF scanner much stronger than changes in WBD. Additionally, variations of the mass attenuation coefficient indicate that the X-ray absorption properties of the sediment correlate with the carbonate content. Grain-size variations seem to have no significant influence on the scanner intensity in the relatively fine-grained marine sediment of core GeoB7920. However, surface roughness effects can become more pronounced in sediments with more abundant sand-sized particles (Jansen et al., 1998; Richter et al., 2006). Reduction of the porosity and interstitial water over depth due to sediment compaction, and density variations related to lithological changes can influence XRF core scanner measurements (Kuhlmann, 2004; Westerhold, 2003). Nonetheless, the relatively small density variations in GeoB7920 have no distinct effect on the XRF core scanner measurements.

Comparison of wet and dry sample measurements indicates much lower element intensities for the wet sample measurements of the lighter elements Al and Si. We assume that the XRF core scanner measurements of the dry samples are not influenced by variations of physical properties. In this case, the dry sample measurements indicate the initial intensity and

the wet sample measurements indicate the residual intensity as stated by the Beer-Lambert law. The strongly reduced Al and Si intensities of wet sample measurements is related to the transmission of the artificially enhanced water content due to pooling of water directly under the Ultralene foil. Elevated seawater contents in the wet samples are also indicated by the higher Cl intensities compared to dry samples. The relatively weak K_{α} energies of the elements Al and Si are much more susceptible for absorption effects than the relatively strong K_{α} energies emitted by heavier element (Potts, 1987). Moreover, the water film between the Ultralene foil and the sediment surface will be proportionally larger for lighter elements with relatively shallow critical depths, such as Al and Si. A strong influence of interstitial water on the fluorescence radiation of the elements Al and Si was also found for other XRF analyzers (Ge et al., 2005; Kido et al., 2006).

The element intensities of the elements K, Ti and Fe show only minor differences between the wet and the dry sample measurements. The interstitial water and the preparation procedures of the dry samples seem to have only little influence on the quality on the intensities of these elements. The small differences between the wet and dry sample measurements of these elements are related to the analytical precision of the scanner, sample heterogeneity effects, and possible mineralogical effects (Ramsey et al., 1995). The slightly higher Ca intensities of the dry sample measurements compared to the wet sample measurements are related to the grinding of the dry sediment samples. The element Ca mainly represents fine-grained (~8-20 μm) nannofossils, and coarse-grained (>63 μm) foraminifers and foraminifer fragments that consist of carbonate (CaCO_3). Grinding of the relatively coarse-grained CaCO_3 particles to a powder (< 70 μm) (Potts, 1987) homogenizes the CaCO_3 particles in the sample and increases the Ca values.

The high water content (60% to 40%) of sediment core GeoB7920 is common in the upper few meters of marine sediments and declines with depth. Although the Ultralene foil stimulates the formation of a water film between the sediment surface and the foil, the use of a foil is necessary in order to prevent contamination of the measurement unit and desiccation of the sediment during the analyses. The pooling of water directly under the foil is indicated by the much higher Cl intensities of the wet sample measurements compared to the dry sample measurements (Figure 5). However, the artificially enhanced water content and the relatively small sample volume analyzed by the XRF prevent accurate determination and calibration of the water content by standard methods (e.g. by determined from syringe samples). Nevertheless, the exponential functions describing the relation between the Cl intensities and the ratios of the wet and dry sample intensities indicate acceptable correlation

coefficients (Figure 7) and enable accurate prediction of dry sample intensities (Figure 9) for the elements Al and Si. The scatter in the regressions of Figure 7 is related with the analytical uncertainties of elements Al, Si, and Cl. The precision of Cl causes scatter in the x dimension and has an equally strong effect on the regressions of Al and Si. Scatter in the y dimension is related to the analytical precision of the elements Al and Si. Higher element intensities and analytical precision of Si reduce the scatter of the regression and result in a higher correlation coefficient compared to Al. Although the amount of scatter in the regression plots is considerable, the exponential attenuation functions enable one to accurately predict the dry sample element intensities. Furthermore, the predicted element intensities improve the correlation coefficients with conventional XRF analyses significantly for the elements Al and Si. Hence, correcting for the water content by using the Cl intensity as a proxy for the water content, clearly improves the quality of the XRF core scanner measurements for the element Al and Si. The differences between the predicted element intensities and the dry sample measurements are ascribed to analytical uncertainties, mineral heterogeneities and sample-to-sample heterogeneities.

5 Conclusions

The split sediment cores analyzed with the Avaatech XRF core scanner are covered with a foil to prevent contamination of the measurement unit and desiccation of the sediment. However, cohesive and adhesive properties of water cause the formation of a thin water film between the sediment surface and the foil. This water film artificially enhances the water content in the sample volume analyzed by the XRF core scanner, which strongly reduces the element intensities of the lighter element Al and Si. These lighter elements have relatively low fluorescence energies and are, therefore, more susceptible to absorption effects than the higher fluorescence energies of heavier elements. Comparison of XRF core scanner measurements taken at the split core sediment surface and on dry powder samples illustrates the influence of the artificially elevated water content on XRF core scanner data. Cl intensities, which are predominantly restricted to seawater, can be used as a proxy for interstitial seawater in the sample volume analyzed by the XRF core scanner. Hence, comparison of Cl intensities and the element intensity ratios of wet and dry sample measurements can be used to quantify the attenuation of the artificially elevated water content for a given element. These functions successfully predict the element intensities of the dry sample measurements and significantly improve quality of the XRF measurements.

Acknowledgements

We would like to acknowledge Holger Kuhlmann, Thomas Westerhold, Heike Pfletschinger, Jan-Berend Stuut, and Christian Winter for their helpful suggestions throughout this study. Vera Lukies is thanked for her help with the XRF core scanner measurements, and Hella Buschhoff and Karsten Enneking for their support with the laboratory work. Furthermore we like to acknowledge the support of Aad Vaars, Sjerry van der Gaast, Bob Koster and Thomas Richter with the XRF core scanner. We owe many thanks to the captain and all cruise participants of RV Meteor cruises M53/1. Finally, we wish to thank the reviewers greatly helped to improve the manuscript. This study was funded by the Deutsche Forschungsgemeinschaft (DFG) as part of the DFG Research Center Ocean Margins at the University of Bremen. This is RCOM publication RCOM0439.

- Chapter 4 -

Sedimentation processes and marine productivity off Cape Blanc (NW Africa) during the last glacial-interglacial cycle

Rik Tjallingii¹, Jan-Berend Stuut¹, Torsten Bickert¹, Ursula Röhl¹, Maarten Prins²

¹ DFG Research Center for Ocean Margins, University of Bremen, 28334, Bremen, Germany

² Department of Paleoclimatology & Geomorphology Vrije Universiteit, Amsterdam, The Netherlands

To be submitted to Paleooceanography

Abstract

We present a millennial-scale record of eolian dust input and marine productivity in the upwelling area off Cape Blanc (Northwest Africa) during the last glacial- interglacial cycle. Grain-size analyses of the carbonate-opal-organic free sediment fraction and Zr-Rb ratios were used to indicate variations of the continental aridity and paleo-wind strength. Furthermore, we used the Si-Fe ratio to indicate the contribution of coastal eolian dust sources. These data show high contributions from coastal dust sources and maximum surface trade wind intensities during the maximum glacial conditions of marine isotope stage (MIS) 2 and 4. However, low opal and low total-organic-carbon (TOC) accumulation rates coincident with these periods indicate low coastal upwelling intensities and marine productivity off Cape Blanc probably related to increased trade wind zonality. Elevated opal accumulation rates occur during glacial Dansgaard-Oeschger (D-O) stadial events, whereas strongly increased TOC accumulation rates occur during glacial D-O interstadial events. We suggest that the antiphasing of opal and TOC accumulation off Cape Blanc is linked to surface circulation and trade wind intensities. Strongly reduced opal accumulations during interglacial humid conditions are related with the Northern position of the Inter Tropical Convergence Zone (ITCZ) and the consequent reorganization of the atmospheric circulation. Finally, variations of eolian dust input or fluvial supply seems to play a minor role on the productivity off Cape Blanc.

Keywords: NW Africa, eolian dust, fluvial sediment supply, upwelling, productivity, end-member modeling, XRF core scanner.

1 Introduction

Over the last decade, paleoclimate studies focused on abrupt climate variations that occurred during the late Pleistocene, indicated as D-O variations (Bond et al., 1993; Dansgaard et al., 1993), in order to understand the causes and effects of abrupt climate events. Although the true trigger mechanism for these high-frequency climate variations is still under debate, there is strong evidence that these climate events are associated with large fresh-water pulses into the North Atlantic (e.g. Rahmstorf, 2002). Climate records obtained from ice cores (Johnsen et al., 2001; NGRIP-members, 2004) and marine sediments (Hemming, 2004; Leuschner and Sirocko, 2000) indicate a widespread footprint of these abrupt climate events. However, the involvement of the subtropical oceanic and atmospheric processes and their possible feedbacks are still largely unanswered, and could provide crucial information regarding the ultimate implications of these extreme and abrupt climate events. The region off Northwest Africa is an ideal study area to investigate these processes because this region records coherent high and low latitude climate signals due to its oceanographic setting (Chapman, 1996; deMenocal et al., 2000b; Zhao et al., 1995). The region off Cape Blanc is strongly influenced by Northeast trade winds that induce year-round upwelling (Harris et al., 1996; Helmke et al., 2005; Wefer and Fischer, 1993; Zhao et al., 2006) and carry large amounts of eolian dust from the Sahara Desert to the proximal Atlantic Ocean (Chiapello et al., 1995; Stuut et al., 2005; Tetzlaff and Peters, 1986). Consequently, the paleoclimate archives from the Cape Blanc region contain valuable information about the variations in continental climate and marine productivity.

Present-day primary production is monitored by chlorophyll-*a* concentrations in the surface waters obtained from satellite imagery that is high consistent with the TOC collected in sediment traps off Cape Blanc (Helmke et al., 2005). Similarly, paleoproductivity variations in this region have been reconstructed by chlorophyll-*a* accumulation in marine sediments, which are in good agreement with the mass accumulation rates of opal and TOC (Harris et al., 1996). At present, productivity in the upwelling areas off Northwest Africa is primarily controlled by the strength of the Northeast trade winds (Adkins et al., 2006; Helmke et al., 2005; Zhao et al., 2006). However, the accumulation rates of TOC were lowest during the Last Glacial Maximum (LGM) (Bertrand et al., 1996; Martinez et al., 1999; Zhao et al., 2006), although trade wind system strongly intensified during this time (Sarnthein and Koopmann, 1980; Sarnthein et al., 1981). Bertrand, *et al.* (1996) explained the strongly reduced productivity during the LGM by reduced upwelling or by the migration of upwelling areas further off shore. A detailed reconstruction of opal accumulation rates off Cape Blanc

suggests that upwelling intensities are tightly coupled to the continental hydrological balance during the Holocene (Adkins et al., 2006). The hydrological conditions varied strongly over Northwest African during the last deglaciation and the Holocene (deMenocal et al., 2000a; Gasse, 2002) influencing the amount and the spatial distribution of fluvial and eolian sediments (Sarnthein and Koopmann, 1980).

The present-day distribution of the terrigenous sediment fraction (carbonate and opal free) over the continental margin off Northwestern Africa indicates that eolian dust dominates the region between 12° and 25°N with a maximum at 20°N, whereas fluvial supply becomes more abundant North and South of this region (Holz et al., 2004; Sarnthein and Koopmann, 1980; Tetzlaff and Peters, 1986). Hyper-arid desert conditions and intensification of the trade wind system during the LGM were deduced from a strong offshore expansion of the terrigenous coarse-silt sediment fraction and a southward shift of the fluvial fraction to south of 10°N (Sarnthein and Koopmann, 1980; Sarnthein et al., 1981). These observations were based on the assumption that fluvial sediments are generally finer than 6 µm, as found from terrigenous sediments off Northwest African river deltas, and that eolian sediments are coarser than 6 µm (Koopmann, 1981). Increasing eolian contributions were interpreted as enhanced continental aridity, whereas coarsening of the eolian contributions were interpreted as increasing of the wind intensities. During the hyperarid conditions of the LGM and the arid present-day conditions, the terrigenous fraction consists predominantly of eolian dust transported, although fluvial sediments from ephemeral rivers played a major role during humid periods (Tiedemann et al., 1989). Abundant fluvial sediments all along the continental Northwest African slope illustrate the humid conditions of the early Holocene African humid period, and reveal a complete halt of dust supply by the surface trade wind system (Sarnthein and Koopmann, 1980).

Applying the end member modeling algorithm of Weltje (1997) to terrigenous silt fraction of surface sediments from the continental margin off Northwestern Africa distinguished two silt-sized end members and one hemipelagic end member (Holz et al., 2004). This end-member approach revealed similar results for sediments from the continental margins off large coastal deserts and characterized sand or silt-sized end members interpreted as eolian material, and clay to fine-silt sized interpreted as fluvial derived material (Holz et al., 2004; Prins and Weltje, 1999; Stuut and Lamy, 2004; Stuut et al., 2002). Consequently, wind-strength variations can be deduced from the proportional variations of the eolian grain-size fractions, whereas the proportional variations of river-derived material indicates variations in river run off, which is related to continental-humidity. Moreover, it was shown

that paleowind strength variations can also be indicated by the variations of the heavy mineral fraction (Liu et al., 2006; Martinez et al., 1999; Matthewson et al., 1995) since the element Zirconium (Zr) is restricted to the mineral Zircon occurring predominantly in the coarse-silt fraction, whereas Rubidium (Rb) is particularly common in the clay fraction (Matthewson et al., 1995). The silt-sized eolian dust particles off Northwest Africa mainly consist of quartz grains (Koopmann, 1979; Parkin and Shackleton, 1973). Intensely iron-stained quartz grains originate from the southern Sahara and Sahel region supplied by more zonal wind systems at mid-tropospheric levels (Balsam et al., 1995; Koopmann, 1981). Dust loads from the northern Sahara, the Atlas Mountains, and the coastal areas are transported by the Northeastern trade winds that supply pale quartz grains that lack an iron stain (Koopmann, 1979). Hence, variations of the chemical composition of the eolian dust load can also be used to identify the source area of terrigenous sediments.

In this study we compare variations of the grain-size variations and chemical analyses of the terrigenous sediment fraction with opal and organic carbon accumulation rates of marine sediment core GeoB7920 off Cape Blanc during the last interglacial-glacial cycle. We estimate the wind strength and the source area of eolian transported material, and their influence on the upwelling area off Cape Blanc. Here we use a multi-proxy approach of a single sediment core that avoids dating uncertainties among the different proxy records.

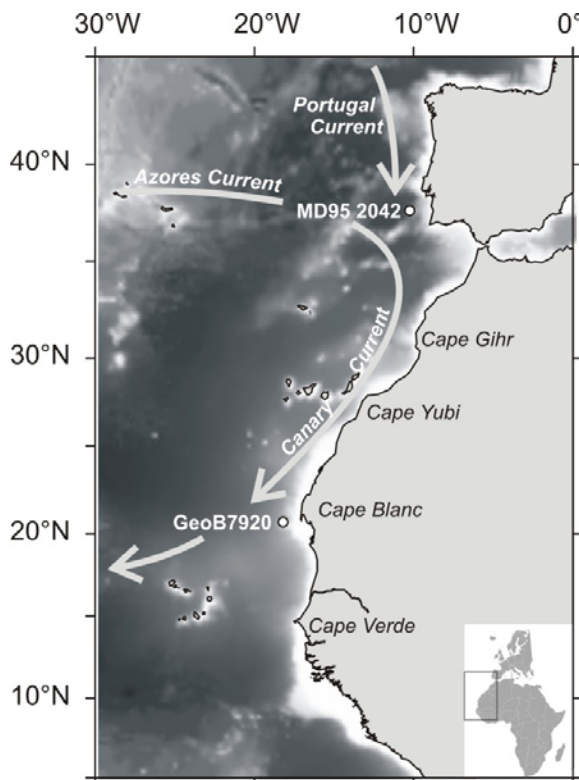


Figure 1. Map of the eastern subtropical Atlantic region indicating the positions of the cores used in this study (black dots), the present-day ocean surface circulation (gray arrows), and the Northwest African capes. The Portugal Current and the Canary Current, that originates from the Azores Current, form the eastern boundary current.

2 Core location and regional settings

Sediment core GeoB7920 (20°45.1'N; 18°34.9'W, 2278 m depth) was retrieved from the slope off Cape Blanc (Mauritania) at the same location as ODP Site 658 (Figure 1) during Meteor expedition M 53/1 (Meggers et al., 2002). At present, the area off Northwest Africa is the most prominent high productivity region in the subtropical Northeastern Atlantic due to wind-induced upwelling of sub-surface water masses. Upwelling occurs throughout the year in the region off Cape Blanc and occurs seasonal north (boreal winter/spring) and south (boreal summer/fall) of this region following the migration of the ITCZ (Helmke et al., 2005). The surface waters north of Cape Blanc are underlain by oxygen-rich but relatively low-nutrient North Atlantic Central Water (NACW), and South of Cape Blanc by the nutrient-rich South Atlantic Central Water (SACW) (~ 150 - 450 m) (Hagen, 2001; Siedler and Onken, 1996). The boundary between these water masses follows the Canary Current (Figure 1) that detaches away from the coast to a westward direction between 25°N and 22°N (Siedler and Onken, 1996). The encounter between the southward flowing Canary Current and the northward flowing undercurrent causes eddy-type mixing of the two water masses (Mittelstaedt, 1991). Moreover, off Cape Blanc the Canary Current front separates coastal upwelling from open ocean productivity (Hagen, 2001; Mittelstaedt, 1991). Annual variations in the primary production off Cape Blanc obtained from satellite imagery and mooring sites suggest that enhanced surface water productivity is related with El Niño-Southern oscillation (ENSO) (Helmke et al., 2005). In turn, the supply of nutrient-rich SACW from the equatorial Atlantic into the region off Northwest Africa may be linked to ENSO or North Atlantic Oscillation (NAO) variations (Hagen, 2001). At present, core GeoB7920 is situated in water masses of North Atlantic Deep Water (NADW) found at water depths below 2000 m off northwest Africa.

Core GeoB7920 is situated adjacent to the Sahara Desert under the major present-day African dust plume. At present, the hyper-arid Sahara Desert stretches between approximately 32°N and 20°N and separates the Northern Africa summer and winter rainfall regimes (Gasse, 2002; Nicholson, 2000). Precipitation in the Sahel region depends on the position of the ITCZ and the southwestern low-level monsoon flow located south of the ITCZ (Figure 2). The formation of a low pressure cell over the southern Sahara and the northward migration of the ITCZ to 18°-20°N during boreal summer, bring the moist monsoonal air flow from the tropical Atlantic into northwest Africa (Gasse, 2002; Nicholson, 2000). During boreal winter, the Mediterranean zone receives precipitation from the Northeast Atlantic brought by frontal systems of the mid-latitude Westerlies due to the more southeastern position of the Azores

high-pressure system (Nicholson, 2000). The northern Sahara also belongs to the area of winter rainfall although precipitation in this area is low and irregular (Gasse, 2002). The Northeast trade wind is the dominant surface wind system over the hyper arid Saharan region north of the ITCZ, and is the major supplier of the silt-sized pale-quartz from coastal regions to proximal parts of the eastern Atlantic (Koopmann, 1981; Pye, 1987; Stuut et al., 2005). The Northeast trade wind system migrates seasonally over northwestern Africa along with the ITCZ, but is active year-round at the Cape Blanc region (Nicholson, 2000). The mid-tropospheric Saharan Air Layer carries eolian dust from the southern Sahara of which the silt-size fraction settles within a zone extending to approximately 700 km off shore during boreal summer (Koopmann, 1981; Pye, 1987). A particular expression of the Northeast trade winds system, the Harmattan, supplies eolian dust from the southern Sahara and Sahel region predominantly during boreal winter into the equatorial Atlantic. The silt-sized eolian dust fraction from the southern Sahara and the Sahel region is characterized by intensely iron-stained quartz grains (Koopmann, 1981).

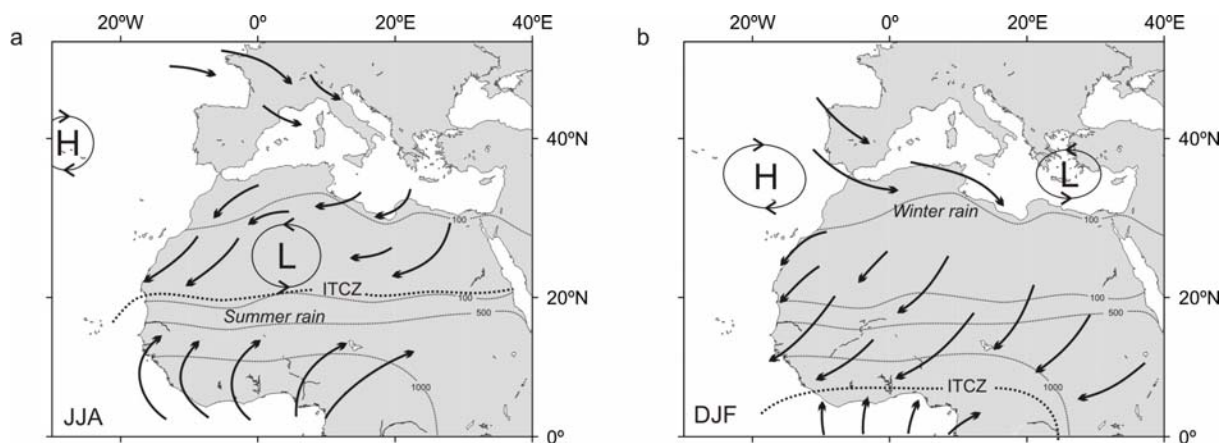


Figure 2. Seasonal variation of the position of the ITCZ, the major wind systems and pressure cells, and areas of precipitation over northern Africa. a) Boreal summer situation. b) Boreal winter situation. Arrows indicate direction of the surface winds, whereas H indicates an atmospheric high-pressure cell and L an atmospheric low-pressure cell. The fine dotted lines indicate the mean annual precipitation (mm/yr).

3 Methods

Approximately 0.5 ml sediment was used to isolate and analyze the grain-size distribution of the lithogenic fraction. For that, carbonate, organic carbon, and biogenic silica were removed with excess HCl, H₂O₂, and NaOH respectively, and neutralized after every treatment. Random microscope observations were obtained to cross check the removal of all biogenic constituents. To avoid the fine-grained fraction to form aggregates, each sample was boiled with ~300 mg of Na₄P₂O₇·10H₂O for approximately one minute shortly before measuring.

The grain-size distribution of each sample was obtained with the Coulter LS200 laser particle sizer that measures particles in the range from 0.4 to 2000 μm in 92 size classes. All measurements were performed with degassed water and repeated about 3 to 4 times to minimize the effect of air bubbles.

The grain-size distribution data of core GeoB7920 were unmixed with the end-member modeling algorithm (Weltje, 1997), which expresses the complete data set as a limited number of subpopulations. The end-member modeling algorithm provides the simplest possible explanation of the observed variation among a set of compositions in terms of mixing. To estimate the minimum number of end members required for a satisfactory approximation of the data, the coefficients of determination were calculated for 2 to 10 end members. The coefficient of determination represents the proportion of the variance of each grain-size class that can be reproduced by the approximated data. This proportion is equal to the squared correlation coefficient (R^2) of the input variables and their approximated values (Weltje, 1997). The goodness of fit is indicated by the coefficient of determination (R^2) and the mean coefficient of determination (R^2_{mean}) that are calculated for an increasing number of end-members. The best statistical fit is given by the least amount of end members that explain the largest amount of variance.

The relative elemental concentrations of the elements Silicon (Si), Iron (Fe), Rubidium (Rb) and Zirconium (Zr) were measured as element intensities directly at the split core surface in a non-destructive way with the XRF core scanner at the MARUM institute, University of Bremen. The elements Si and Fe were measured every 2 cm at 10 kV for 30 seconds. The elements Rb and Zr were measured every 1 cm at 50 kV in combination with a Cu filter for 30 seconds. A gap in the archive half of the core prohibited accurate measurements to be taken between 4.80 and 4.90 m. The element intensities of the lighter element Si are corrected for intensity loss due to the interstitial water (Tjallingii et al., 2007).

The dry bulk density (DBD) was calculated from the wet and freeze-dried weight (Weber et al., 1997) of 10 ml syringe samples. Carbonate (CaCO_3), organic matter (TOC), and biogenic opal analyses were performed on a small proportion of the freeze-dried and ground sediment samples with a sample resolution of 5 cm. CaCO_3 and TOC measurements were performed on the Elementar Vario EL 3 CHN. The opal content was measured using an automated leaching method (Müller and Schneider, 1993) with a sample resolution of 10 cm. The lithogenic content was calculated as the proportional weight of the sediment fraction free of carbonate, organic matter, and biogenic opal. The proportional weight (in Wt. %), linear

sedimentation rates (LSR in cm/ka), and the DBD (in g/cm³), were used to calculate the mass accumulation rate of TOC and opal ($MAR = LSR * DBD * C/100$).

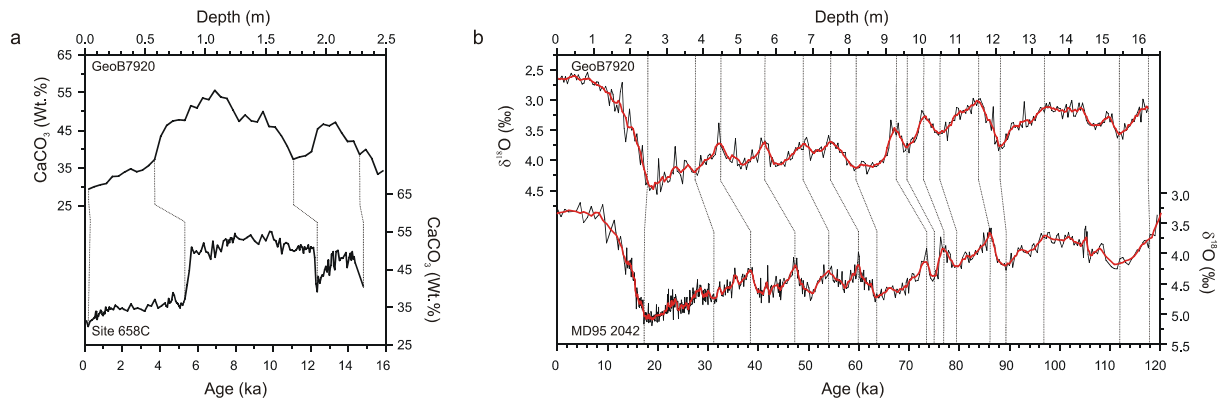


Figure 3. Age model of core GeoB7920. a) Correlation of the carbonate stratigraphy of cores GeoB7920 with the ¹⁴C AMS dated record of ODP Site 658C (deMenocal, et al., 2000b). b) Correlation of the oxygen-isotope stratigraphy of GeoB7920 and core MD95 2042 (Shackleton, 2000) on the GRIP ss09sea age scale (Johnsen, et al., 2001; Shackleton, et al., 2004). The gray line indicates the original data and the red line indicates the 5-point moving average.

4 Chronostratigraphy

The age model of core GeoB7920 was constructed by peak-to-peak correlations performed with the software package Anayseries 1.1 (Paillard et al., 1996). The upper 14.8 ka (2.28 mbsf) of our age model was constructed by peak-to-peak correlation of the carbonate record of GeoB7920 with the carbonate record of the parallel sediment core ODP Site 658C (Figure 3a) (deMenocal, et al., 2000a; deMenocal, et al., 2000b). The age control of the upper 14.8 ka of Site 658C was established by 22 accelerator mass spectrometer radiocarbon dates. Although there is an acceptable match between the carbonate records, peak-to-peak correlation inhibits to accurately determine the age of the core top (Figure 3a). The age model of core GeoB7920 prior to 17.3 ka (2.58 mbsf) was constructed by a correlation of the 5-point average smoothed *Cibicides wuellerstorfi* $\delta^{18}\text{O}$ stratigraphy with the stable benthic oxygen isotope stratigraphy of core MD95 2042 located off Portugal (Figure 1). Both core GeoB7920 and core MD95 2042 are situated under the direct influence of the North Atlantic eastern boundary current system. The stratigraphy of core MD95 2042 contains a very well dated stratigraphy based on ¹⁴C AMS dating calibration of paired ¹⁴C and ²³⁰Th measurements on pristine corals (Cayre et al., 1999; Shackleton et al., 2004; Shackleton et al., 2000). The oxygen-isotope stratigraphy of GeoB7920 is in good agreement with the record of core MD95 2042 (Figure 3b), and covers the marine isotopic stages (MIS) 5.4 to 1 after Martinson *et al.* (1987). Accordingly, the age model of the 16.18 meter long core GeoB7920 spans the last

~118 ka (Figure 4). Sedimentation rates are calculated by linearly interpolation between the correlation points, and vary between 7.8 and 23.8 cm/ka (average ~ 15 cm/ka) (Figure 4b).

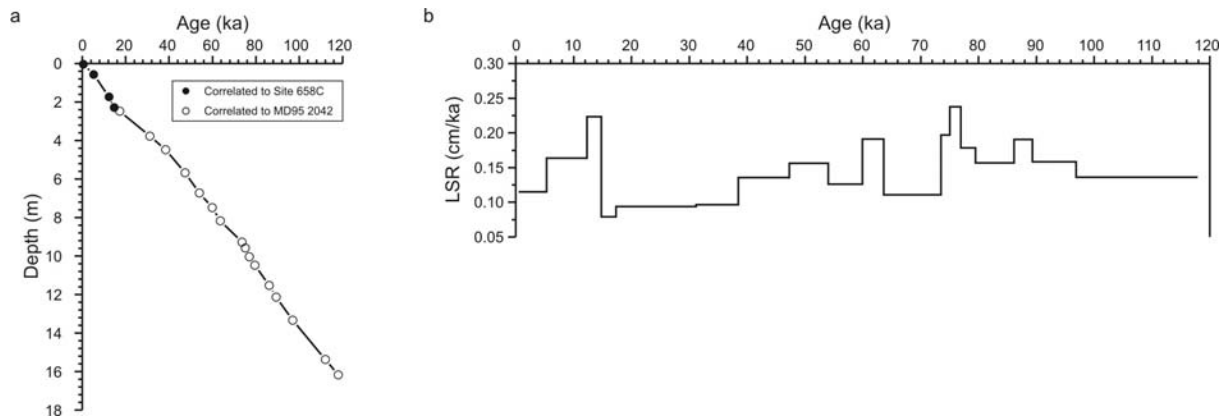


Figure 4. a) Age model of core GeoB7920. b) Linear sedimentation rates (LSR) of core GeoB7920 calculated by linear interpolation between the correlation points of the age model.

5 Results and interpretations

5.1 End-member modeling

Statistically evident grain-size populations were calculated from the terrigenous grain-size distributions with the end-member modeling algorithm of Weltje (1997). The minimum number of end members (EMs), required for a satisfactory approximation of the data resulted in three end members that explain 88% of the total variance (R^2_{mean}) in the grain-size distributions ($N = 316$) of core GeoB7920 (Figure 5). The three end members EM1, EM2, and EM3 have modal grain-sizes of 57.8 μm , 34.6 μm , and 4.9 μm , respectively (Figure 5c).

The terrigenous fraction of surface sediments from the Northwest African margin was described by a three-end-member model (Holz et al., 2004) with comparable grain-size distributions as found in core GeoB7920 (Figure 6). The spatial distribution of these surface sediment end-members indicate high proportions coarse-grained end members (EM1 and EM2) in the regions off Cape Blanc that are dominated by eolian transported material. The fine-grained end member (EM 3) is most dominant off northern Morocco with predominantly fluvial transported sediments due to high river run-off from the Atlas Mountains (Holz et al., 2004). Hence, EM1 and EM2 are interpreted as proximal and distal eolian transported material, respectively. The fine-grained end member (EM3) is interpreted as a hemipelagic end member associated with predominantly fluvial transported material.

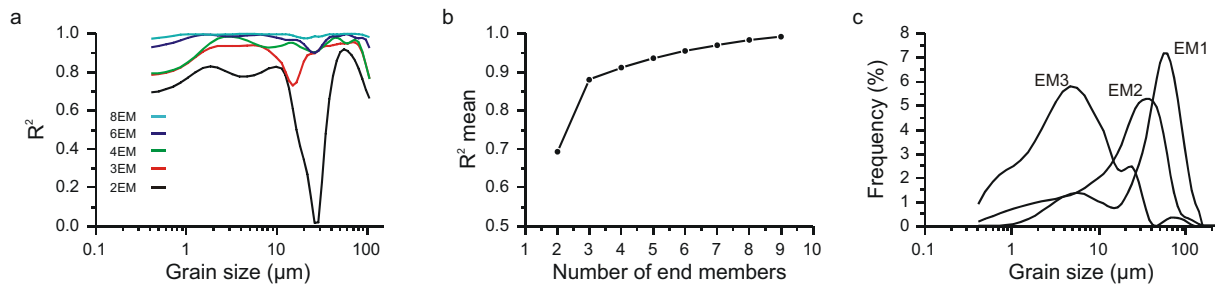


Figure 5. Goodness-of-fit statistics of the predicted grain-size populations and the grain-size distributions of the three-end-member model. a) Coefficients of determination (R^2) for each size class and for different end-member solutions (2 to 9 end members). b) Mean coefficient of determination (R^2 mean) for different end-member solutions (2 to 9 end members). c) Modeled grain-size distributions of the three-end-member model for the sediment fraction free of carbonate, organic matter, and opal of core GeoB7920.

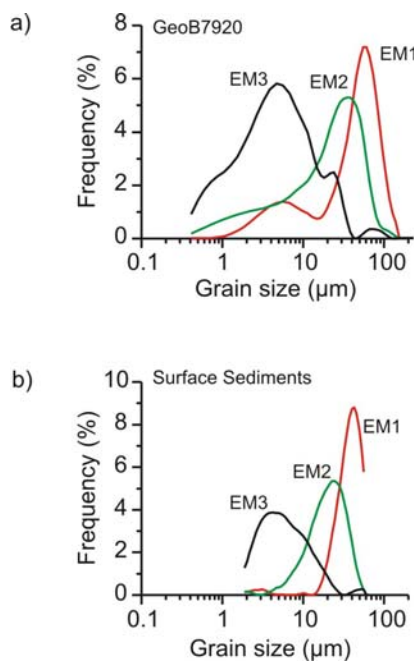


Figure 6. Grain-size distribution of the end members obtained from the terrigenous fraction of: a) core GeoB7920, and: b) surface sediments from the Northwest African margin (Holz, et al., 2004).

5.2 Wind strength and continental aridity

Interpreting the three end members as proxies for proximal eolian dust (EM1), distal eolian dust (EM2), and fluvial mud (EM3), the proportional variation of the three end members can be used as paleoclimate indicators. Variations of total eolian transported material depend on variations in the continental hydrological balance and related changes of the vegetation cover (deMenocal et al., 2000a; Parkin and Shackleton, 1973; Tiedemann et al., 1994; Tiedemann et al., 1989). Accordingly, a reduction of the proportion eolian end members (EM1 + EM2) is linked with reduced eolian dust input due to expansion of the vegetation cover, or an increase of the proportions EM3 due to enhanced river run off from the continent. Although presently there are no active river systems discharging at Cape Blanc, there are strong indications that larger river systems have been active during past humid conditions (Krastel et al., 2004;

Vörösmarty et al., 2000). Nevertheless, both reduced proportions of the eolian end members as a result of expansion of the continental vegetation cover, and enhanced proportions of the hemipelagic end member as a result of increased fluvial supply indicate reduced continental aridity.

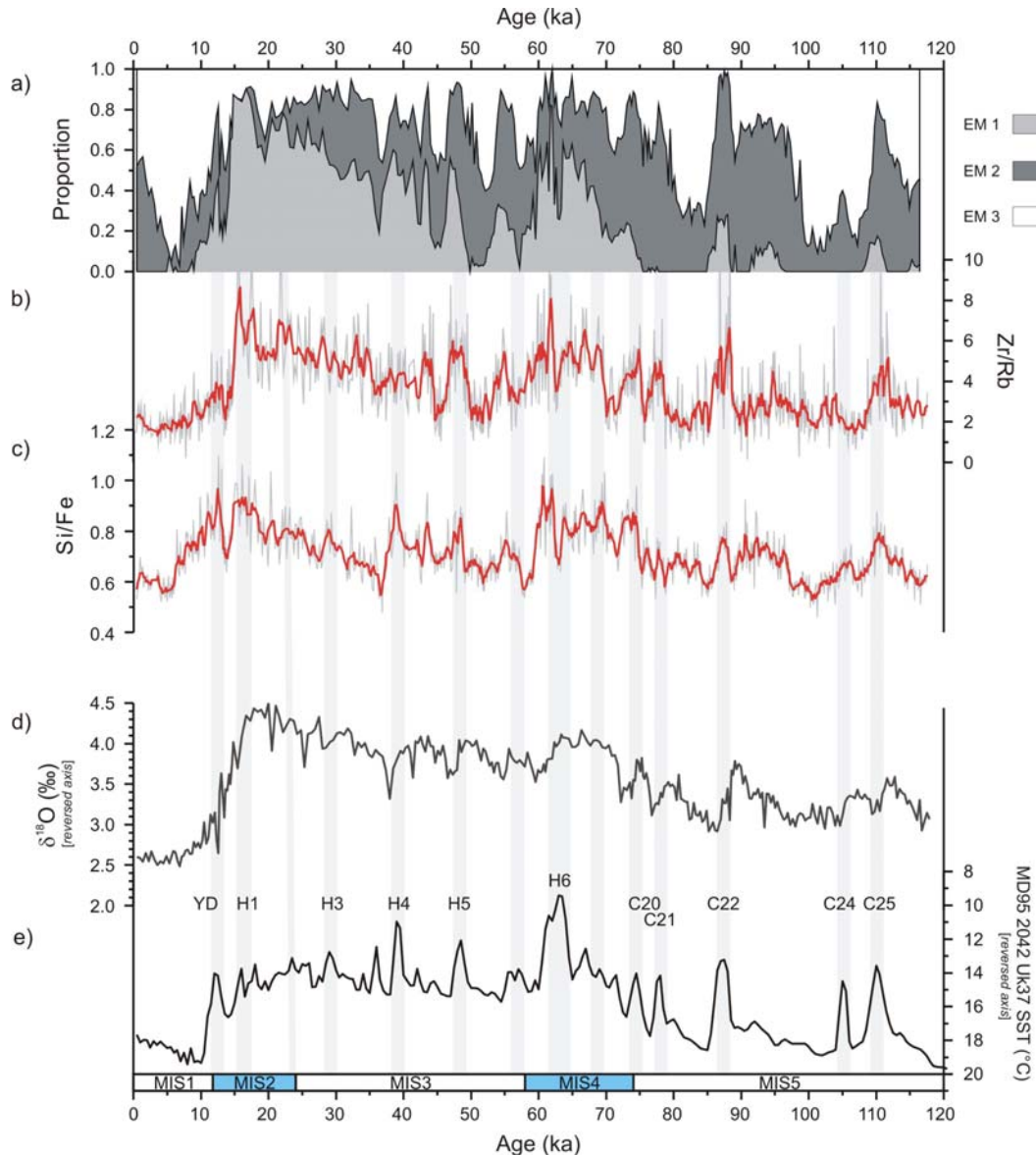


Figure 7. Results from terrigenous material in sediment core GeoB7920. a) Variation of the relative abundances of end members. b) Variation of the Zr-Rb ratio calculated from XRF core scanner measurements indicating the relative variation of the heavy mineral fraction (reversed axis). The gray line indicates the 1 cm resolution; the red line indicated the 5-point moving average. c) Variation of the Si-Fe ratio calculated from XRF core scanner measurements indicating the variation of pale quartz grains from coastal sources, and iron stained quartz from inland dust source. The gray line indicates the 1 cm resolution; the red line indicated the 5-point moving average. d) Benthic $\delta^{18}\text{O}$ stratigraphy of GeoB7920 that indicates changes in the global ice volume. e) Mean annual SST record from core MD95 2042 [Bard, et al., 2004]. Shaded areas indicate D-O stadial events associated with Heinrich ice rafting events (H events) and Greenland cold events (C events) as shown by the mean annual SST record of core MD95 2042.

Down-core variations of the coarse-grained end member (EM1) are closely related to variations of the heavy mineral fraction indicated by the Zr-Rb ratio (Figure 7). The proportions EM1 and Zr-Rb ratios show a particular strong resemblance to the benthic $\delta^{18}\text{O}$ record indicating increased trade wind intensities during periods of increased global ice volumes (Figure 7). Higher frequent variations show increased proportions EM1 and enhanced Zr-Rb ratios in combination with strongly decreased SSTs in the eastern North Atlantic off Portugal (Figure 7), which are associated with Heinrich ice rafting events and Greenland stadial conditions (Bard et al., 2004; Pailler and Bard, 2002). The increase of proportion EM1 and the Zr-Rb ratios during glacial stadial events suggest abrupt intensification of the northeast trade winds and the supply of coarse-grained coastal dust sources. In addition, high Si-Fe ratios during D-O stadial events suggest more eolian input from local coastal sources and less iron-stained eolian material from the Southern Sahara. Alternatively, exposure of the relatively broad continental shelf off Cape Blanc, and consequent reduction of the distance between core and coast due to the glacial sea level low stand, could have increased the influence of more local coastal dust sources during full glacial conditions. Reduced proportions EM2 and relatively high Si-Fe ratios during full glacial conditions of MIS 4 and MIS 2 suggest stronger influence of coarse-grained coastal sources and possibly bypassing of the finer silt-sized dust fraction to more distal parts of the Atlantic margin. Abruptly increasing proportions EM2 together with increasing proportions of EM1 and higher Zr-Rb ratios suggest aridification over the continent associated with an intensification of the surface trade wind system during interglacial stadial events (Figure 7). Enhanced proportions of EM2 during the stadial events of MIS 5 correspond to elevated Zr-Rb ratios, whereas proportions EM1 are low or even lacking. Hence, the Zr-Rb ratio is not strictly related to the sand-sized terrigenous fraction described by EM1, but is also abundant in the terrigenous coarse-silt fraction described by EM2.

5.3 Mass accumulation rates and productivity

We calculated the opal and TOC mass accumulation rates (MAR in $\text{g/cm}^2/\text{ka}$) from linear sedimentation rates (Figure 4). Both the opal and the TOC accumulation rates indicate low productivity during the full glacial conditions of MIS 4, at the end of MIS 3, and during MIS 2. Elevated opal accumulation rates occur during periods with enhanced eolian contribution during MIS 5, the Heinrich and stadial events of H4, H5, H6, C20, C21, C22, and during the last deglaciation (Figure 8). These events co-occur with elevated proportions of EM1 and of

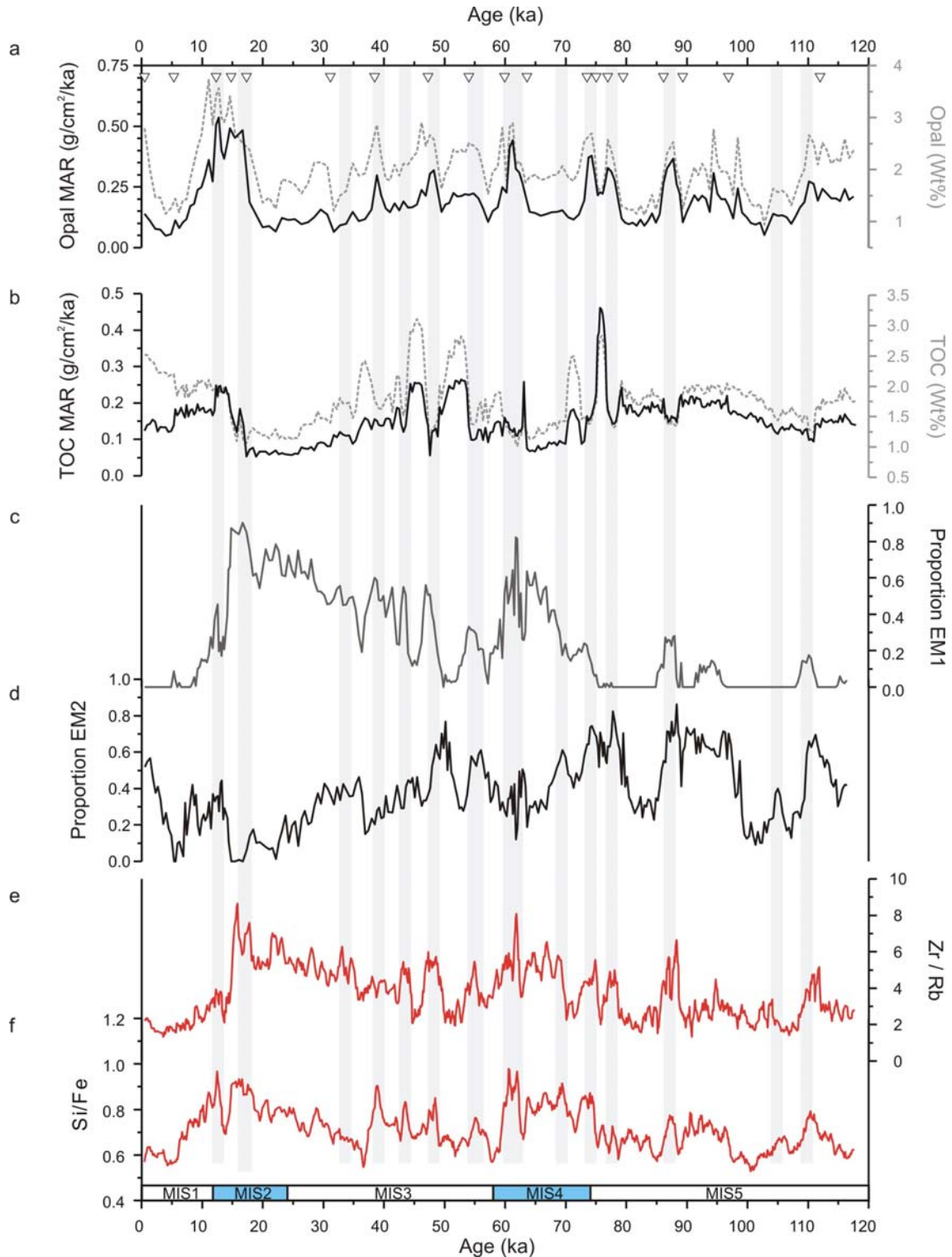


Figure 8. Results from sediment core GeoB7920. a) Opal mass accumulation rates (MAR, black line, in $\text{g}/\text{cm}^2/\text{ka}$) and TOC contents (dotted gray line, in wt. %). Black triangles indicate the correlation points of the age model used to calculate linear sedimentation rates and MAR. b) TOC MAR (black line, in $\text{g}/\text{cm}^2/\text{ka}$) and opal contents (dotted gray line, in wt. %). c) Variation of the relative abundances of EM1. d) Proportional variation of EM2. e) 5-point moving average of the Zr-Rb ratio indicates the relative contribution of the heavy mineral fraction. f) 5-point moving average of the Si-Fe ratio used to indicate the relative contribution of the pale-quartz coastal dust sources and the iron-stained quartz from the southern Sahara and the Sahel region. Shaded areas indicate D-O stadal events as shown in figure 7.

EM2 suggesting enhanced trade wind intensities and continental aridity (Figure 8c-d). Additionally, the relatively high Zr-Rb and Si-Fe ratios during these glacial stadial events hint to enhanced eolian supply from coastal dust sources (Figure 8e-f). Elevated TOC accumulation rates occur during glacial interstadial conditions whereas upwelling intensities are generally low during these events. High opal and TOC accumulation rates occur during the last deglaciation (Figure 8). Interstadial conditions of MIS 5 and the Holocene indicate low opal accumulation rates during periods of low eolian supply whereas TOC accumulation rates are generally higher than maximum glacial conditions and vary relatively little compared to last glacial variations.

6 Discussion

6.1 Grain-size distributions off NW Africa

The terrigenous fraction of deep-marine sediments off Northwestern Africa consists of a mixture of eolian dust and hemipelagic mud (Holz et al., 2004; Sarnthein and Koopmann, 1980; Weltje and Prins, 2003), comparable to other continental margins adjacent to coastal deserts (Prins and Weltje, 1999; Stuut and Lamy, 2004; Stuut et al., 2002). In general, the down-wind decrease in transport capacity of the trade wind system can be recognized by a down-wind fining of eolian dust (Weltje and Prins, 2003). Consequently, intensity fluctuations of the wind system result in variations of the size of eolian transported sediment fraction at a single location (Prins and Weltje, 1999; Stuut and Lamy, 2004). However, unlike mooring data (Ratmeyer et al., 1999a) and aerosol samples (Stuut et al., 2005) that cover only one dust event of one annual season, marine sediment samples cover many seasonal cycles as given by the sedimentation rates. Therefore, sediment samples can be described as a mixture of end members that reflect the transport capacity of different transport mechanisms. Accordingly, the spatial distribution and depositional environments of the end members from surface sediments can be used as an analogue for the depositional environments of the end members derived from sediment core GeoB7920. Indeed, the end members of GeoB7920 are very similar to the end members resulting from the surface samples from the margin off Northwest Africa of Holz *et al.* (2004), despite the fact that these result from a different grain-size analyzer (SediGraph) and the samples were not free of biogenic opal.

The end members obtained from the terrigenous fraction allow the distinction of different sediment-transport mechanisms and their relative contribution to the total terrigenous fraction. Off Cape Blanc the terrigenous sediment fraction is mostly interpreted as

strictly eolian supply, since the majority of land-derived sediments are of eolian origin (Adkins et al., 2006; deMenocal et al., 2000a; Matthewson et al., 1995), although fluvial sediments by ephemeral coastal rivers might play a role during more humid periods (Sarnthein and Koopmann, 1980; Tiedemann et al., 1994). Moreover, mooring data suggest fluvial sediments or laterally advected sediments off Cape Blanc even under the present day arid conditions (Ratmeyer et al., 1999b). The three-end member model of sediment core GeoB7920 demonstrates that the terrigenous sediments fraction off Cape Blanc consists of a mixture of two silt-sized end members and a clay-fine silt end member. These end members suggest that the terrigenous sediments fraction off Cape Blanc consists of both eolian-transported material and hemipelagic mud associated to fluvial transported.

6.2 Continental aridity and wind strength

The enhanced proportions EM1 and EM2 during glacial conditions (Figure 8) indicate strongly enhanced continental aridity. High proportions eolian dust during the LGM indicates expansion of hyper arid desert conditions over Northwest Africa (Sarnthein and Koopmann, 1980; Sarnthein et al., 1981). Moreover, elevated proportions EM1 and enhanced Zr-Rb ratios in core GeoB7920 also suggest intensification of the surface wind system during the full glacial conditions of MIS 4, MIS 2, and the stadial events. The good correlation between the stable benthic oxygen isotope record and the proportions EM1 (Figure 7) strongly suggest that the trade wind intensities are linked to the expansion of high latitude ice sheets during glacial conditions. Expansion of high latitude ice sheets during glacial conditions induced a squeezing and southward displacement of the temperate climate zones including the North Atlantic Westerly system (Sarnthein et al., 1981). The southward displacement of the temperate climate zones would have intensified the atmospheric circulation due to the increased meridional temperature gradients (Sarnthein et al., 1981). In addition, intensification of the surface trade winds under glacial conditions is further suggested by the enhanced Zr-Rb ratios and Si-Fe ratios. Higher Si-Fe ratios indicate a relative increase of pale-quartz from the Northwest African coastal over the iron-stained quartz from the southern Sahara dessert transported by the midtropospheric wind system (Koopmann, 1981). Hence, these results indicate that coarse-grained eolian material originated predominantly from coastal dust sources as suggested for present-day aerosol samples (Stuut et al., 2005).

The strong and abrupt increase of the proportions EM1, EM2, and the Zr-Rb ratios that co-occur with reduced SSTs in the eastern boundary current off Portugal (Bard et al., 2004) suggest increased continental aridity and trade wind intensities associated with high-

latitude stadial events Heinrich events (Figure 7). The strongly reduced SSTs associated with these events were transmitted to lower sub-tropical Northeast Atlantic by the eastern boundary current (Chapman et al., 2000; Zhao et al., 1995). Intensification of the Northeast trade wind during high-latitude stadial and Heinrich events is also suggested by modeling results (deMenocal and Rind, 1993; Timmermann et al., 2005). Contrary, D-O interstadial conditions indicate reduced continental aridity and relaxation of the surface trade wind system. These relatively humid events are highly consistent with paleoclimatic reconstructions from the Mediterranean (Allen et al., 1999; Combourieu Nebout, 2002; Moreno et al., 2005; Sánchez-Goni et al., 2002; Tzedakis et al., 2003) and the western Iberian margin (Roucoux et al., 2005; Sánchez-Goni et al., 2002). The warm North Atlantic SSTs during interstadial conditions promoted the formation of moist air over the North Atlantic and the reduced North Atlantic pressure gradient instigates a southward displacement of the Westerly wind system (Moreno, et al., 2005).

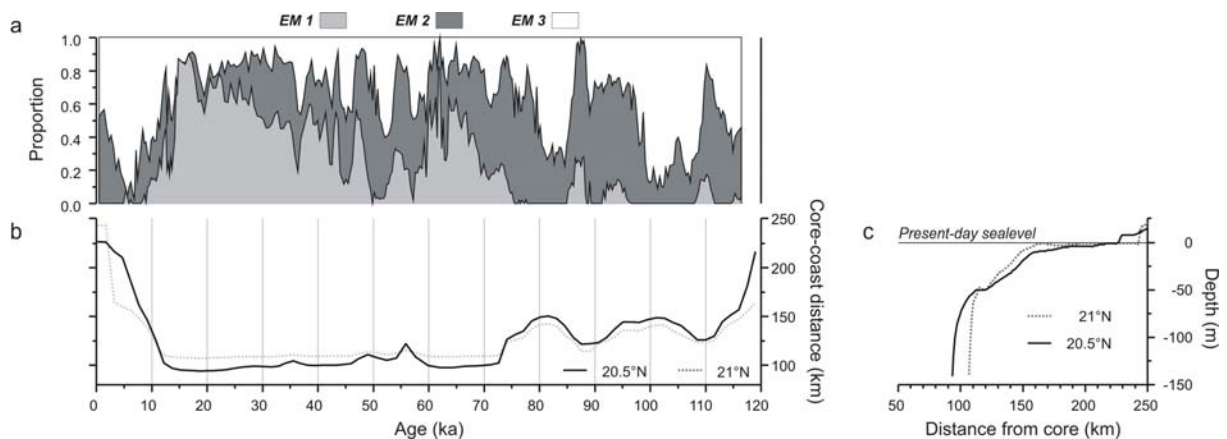


Figure 9. Variation of the relative abundances of end members with respect to sea-level change. a) Variation of the relative abundances of end members in GeoB7920. b) Distance between core position and coastline over time calculated from the interception of the global sea-level curve (Waelbroeck, et al., 2002) and (c) the present-day shelf profiles at 20.5°N (black line) and 21.0°N (dotted gray line).

6.3 Sea-level change

Strong regional differences between glacial and interglacial sedimentation patterns along the Northwest African margin have been attributed to sea-level changes and consequent changes of sediment advection over the shelf and displacement of sediment deposition centers (Bertrand et al., 1996; Martinez et al., 1999). The shelf off Cape Blanc is relatively broad and shallow, and the distance between the core location and the coastline is reduced to less than 100 km during the sea-level lowstand of the last glacial (Figure 9). Owing to the relatively proximal position of core GeoB7920 and the large amounts of terrigenous sediment

transported, we have to take into account the possible effect of sea-level change. Figure 9 shows the core-to-coast distance calculated for the present-day east-west shelf profiles at 20.5°N and 21°N related to the global sea level changes (Waelbroeck et al., 2002). The strongly reduced distance between core and coast during glacial conditions seems to have no significant influence since the proportions proximal eolian sediments (EM1) already decline, although punctuated by an abrupt increase during H1, before sea level rise reduces the core-to-coast distance off Cape Blanc. Hence, the spatial distribution of proximal eolian dust seems to be primarily related to variations in the trade-wind intensity. Nevertheless, exposure of the shelf during glacial conditions inhibits accumulation of fluvial sediments on the shelf, but fluvial supply can be discharged directly on the continental slope instead. Hence, possible ephemeral coastal rivers that were active during the relatively humid glacial interstadial events discharged much closer to the core location. Moreover, lateral advection of fluvial supply from coastal rivers located North of Cape Blanc by the Canary Current could have played a more significant role during the glacial interstadial humid events.

6.4 Productivity variations

Core GeoB7920 is located under the direct influence of the high productivity filament related with upwelling of deeper water masses over the shelf off Cape Blanc (Harris et al., 1996; Helmke et al., 2005). Opal accumulation mainly derives from marine diatoms (Stabbel, 1989) and can be used to indicate the coastal upwelling intensity (Adkins et al., 2006; Harris et al., 1996; Stabbel, 1989). Although the contribution of terrigenous sediments is relatively high, TOC is primarily of marine origin at the core location and can be ascribed to primary production in the surface waters (Harris et al., 1996; Stein et al., 1989).

In general, productivity off Cape Blanc is low during maximum glacial conditions of MIS 4 and MIS 2 and highest during the last deglaciation as indicated by TOC and opal accumulation rates (Figure 8). However, TOC records of sediment cores from the Canary Islands region (Bertrand et al., 2000; Bertrand et al., 1996; Freudenthal et al., 2002) and off Portugal (Cayre et al., 1999; Paillet and Bard, 2002), show only seasonal upwelling under present-day situation, and indicate maximum productivity during the full glacial conditions linked to the trade wind system and upwelling intensification. The strongly decreased productivity off Cape Blanc during the LGM has been linked to shelf exposure that prevented lateral transport of material over the shelf to the Cape Blanc region (Bertrand et al., 2000; Bertrand et al., 1996; Martinez et al., 1999). However, high productivity events also occur during MIS 3 suggesting the effect of upwelling over the shelf is not the major reason for low

productivity during full glacial conditions of MIS 4 and MIS 2. Moreover, marine productivity archives from the upper slope of the Canary Basin indicate that sea-level induced shifting of the upwelling zones probably had a strong imprint on the productivity records (Bertrand et al., 2000; Bertrand et al., 1996; Freudenthal et al., 2002). Low opal and TOC accumulation rates suggest that zonal shifting of the high productivity filament off Cape Blanc is rather unlikely. Possibly, changes in the oceanic surface circulation and the atmospheric circulation could have initiated a meridional migration of the high productivity region. Probably, the zonality of the trade-wind increased during MIS 4 and MIS 2 (Bertrand et al., 1996) and reduced the Ekman transport off Cape Blanc decreasing the coastal upwelling off Cape Blanc. Increased trade-wind intensities and enhanced eolian input during glacial conditions suggest that fertilization of surface waters by eolian dust most likely played a relatively minor role.

The D-O variability of MIS 5 and MIS 3 indicate enhanced opal accumulation rates during D-O stadial events, whereas strongly increased TOC accumulation rates occur during D-O interstadial events (Figure 8). The anti-phasing of opal and TOC accumulation rates indicate a stadial-interstadial decoupling of upwelling intensities and primary production off Cape Blanc. Intensification of the surface trade winds increased coastal upwelling during D-O stadial events. Additionally, cold and fresh melt water introduced in the North Atlantic during Heinrich events was transmitted to the subtropical Atlantic by the eastern boundary current (Chapman and Shackleton, 1998; Zhao et al., 1995). We speculate that the introduction of relatively fresh surface waters during Heinrich events resulted in a stratification of the surface ocean reducing open ocean productivity. Stratification of the water column due to large freshwater input associated with Heinrich events increased the seasonality and reduced the mean annual productivity off Cape Yubi (Meggers et al., unpublished). Moreover, upwelling completely ceased off Portugal during Heinrich events due to introduction of fresh melt water (Bard et al., 2000; Pailler and Bard, 2002). Alternatively, intensification of the trade winds probably strengthened the eastern boundary current preventing a northward migration of the nutrient-rich SACW. Subsequently, we attribute the strongly increased primary production during D-O interstadial events to enhanced open-ocean productivity that strongly increased the mean annual production.

Increased upwelling intensities and productivity during the last deglaciation have been found at multiple sites in the eastern North Atlantic and have been related with large-scale reorganization of atmospheric and oceanic circulation during the major melting phases (Bertrand et al., 1996; Harris et al., 1996; Moreno et al., 2002; Pailler and Bard, 2002; Zhao et

al., 2006). Our data support such a scenario, although the re-establishment of upwelling favorable trade winds probably played a role as well off Cape Blanc. Interglacial conditions show relatively little variations of the TOC accumulation rates compared to the last glacial conditions, which we attribute to relatively stable open ocean productivity. However, strongly reduced opal accumulations seem to be linked to periods of strongly reduced eolian contributions during MIS 5 and the Holocene (Figure 8) suggesting reduced coastal upwelling intensities. Likewise, a link between increased subtropical African aridity and reduced upwelling intensities off Cape Blanc was also suggested by low opal accumulation rates during the early Holocene at ODP Site 658C (Adkins et al., 2006). The strongly reduced eolian dust supply during the early Holocene coincides with the Holocene African humid period during which the Western Sahara was largely covered with vegetation due to strengthening of the African monsoonal system (Claussen et al., 1999; deMenocal et al., 2000a; Prentice et al., 2000). The African humid period is related with a northward movement of the ITCZ (Kutzbach and Liu, 1997) that probably resulted in upwelling unfavorable atmospheric circulation or strongly seasonal reduced coastal upwelling off Cape Blanc. Furthermore, our data suggest that the possible increase of fluvial supply had no significant influence on the primary productivity in the surface waters.

7 Summary and conclusions

End member modeling of the terrigenous grain-size fraction over the last glacial-interglacial cycle reveals strong variations in the Northwest African continental aridity and the intensity of the surface trade-wind system. Both the coarse-grained terrigenous end member and the Zr-Rb ratios indicate that the surface trade-wind intensity is closely linked to the global ice volume. The influence of glacial-interglacial sea level variations and consequent variations of the transport distance to the core location seems to be relatively small. Increased Si-Fe ratios suggest a relative increase of eolian input from coastal dust sources under glacial conditions. However, productivity and upwelling intensities remain low off Cape Blanc despite strongly intensified trade winds during full glacial conditions of MIS 4 and MIS 2, probably due to the stronger trade-wind zonality. Strong and abrupt sub-orbital variations of the eolian end members and chemical sediment composition indicate an intensification of the surface trade winds and continental aridity associated with high latitude D-O stadial events and Heinrich events. Although coastal upwelling intensities increase during these events, open ocean productivity decreases due to the introduction of relatively fresh water in the region off Northwest Africa and consequent stratification of the water column. Contrary, relaxation of

the upwelling intensity and re-initiation of open ocean productivity decreases the seasonality and increases the mean annual production during D-O interstadials. Although the mean annual productivity during interglacial conditions varies only little, variations of the upwelling intensity seem to be coupled to the position of the ITCZ and the strength of the African monsoonal system. In general, productivity variations due to variations of terrigenous input seem to play a minor role in the region off Cape Blanc.

Acknowledgements

We would like to thank Gert Jan Weltje for providing the End-Member Model Algorithm. Heike Pfletschinger and Vera Lukies are thanked for their help with the XRF core scanner measurements. Also, we like to thank Marco Klann, Hella Buschhoff, and Monika Segl for their support with the laboratory work. We owe many thanks to the captain and all cruise participants of RV Meteor cruises M53/1. This study was funded by the Deutsche Forschungsgemeinschaft (DFG) as part of the DFG Research Center Ocean Margins at the University of Bremen. This is RCOM publication No RCOM#.

- Chapter 5 -

Continental humidity in Northwest Africa on orbital and sub-orbital time scales

Rik Tjallingii¹, Martin Claussen^{2,3}, Jens Fohlmeister⁴, Alexandra Jahn⁵, Jan-Berend W. Stuut¹, Torsten Bickert¹, Frank Lamy⁶, Ursula Röhl¹

¹University of Bremen, DFG Research Center for Ocean Margins, Leobener Strasse, Bremen, Germany

²Max Planck Institute for Meteorology, Hamburg, Germany

³Meteorological Institute, University of Hamburg, Germany

⁴Heidelberg Academy of Science, Heidelberg, Germany

⁵Department of Atmospheric and Oceanic Sciences, McGill University, Montreal, Canada

⁶Alfred Wegener Institute, Bremenhaven, Germany

To be submitted to Nature

Abstract

Continental humidity reconstructions based on a marine sediment core off Northwest Africa show that precession-forced humid periods similar to the early-Holocene African Humid Period likewise occurred during marine isotopic stage (MIS) 5. Additionally, these data show a strong influence of high-latitude millennial-scale climate variations under both interglacial and glacial conditions. Our proxy data are consistent with model simulations of both orbital-scale variations of the last glacial-interglacial cycle, and millennial-scale oscillations during MIS 3. Data and model results show that the rather gradual orbital-paced climate variations are punctuated by abrupt dry events associated with North Atlantic ice rafting events.

The Sahara and Sahel region are known for their extreme Holocene climate variations from humid conditions with extensive grassland and numerous lakes during the early-to-middle Holocene African humid period (AHP) to the present-day arid desert conditions (Gasse, 2000; Jolly et al., 1998). These strong climatic variations have been related to precession-forced Northern hemisphere insolation variations and subsequent variations of the African monsoonal system (Kutzbach and Street-Perrott, 1985). Coupled atmosphere-ocean-vegetation model simulations of the Holocene climate indicate that the precessional forcing alone cannot explain the strong variations of the African summer monsoon, and vegetation dynamics are a major amplifier of the climate change over Northwest Africa. The strong non-linear feedback between vegetation dynamics and the subtropical atmosphere create equilibrium conditions that allow two equilibrium states in the Western Sahara; a green state corresponding to stable humid conditions like those of the AHP, and an arid state corresponding to the present-day desert conditions (Brovkin et al., 1998; Renssen et al., 2003). The non-linearity between the vegetation and the subtropical atmosphere enables rapid transitions from the AHP to the present-day arid conditions during the mid Holocene (Claussen et al., 1999). These transitions are indicated by a sharp increase of the terrigenous flux in the marine sediments due to reduced vegetation cover and enhance soil erosion during relatively dry periods (deMenocal et al., 2000a).

Climate records of the Sahara and Sahel region also indicate sub-Milankovitch dry events associated with strongly reduced sea surface temperatures (SSTs) and large-scale reorganization of the North Atlantic thermohaline circulation (THC) during the Younger Dryas and Heinrich event H1 (deMenocal et al., 2000b; Gasse, 2000; Street-Perrott and Perrott, 1990). These Dansgaard-Oeschger (D-O) climate variations are found in many paleoclimatic records indicating a global climate footprint as a result of high-latitude North Atlantic ice-rafting events (Broecker, 1994; Broecker, 2003; Hemming, 2004; Leuschner and Sirocko, 2000), although a trigger mechanism for millennial-scale climate variability is still under debate (Broecker, 2003; Hemming, 2004). Model results indicate that it is unlikely that such trigger mechanisms are located at low latitudes even though these can play an important role in the transmission and possibly the amplification of these signals (Claussen et al., 2003b). Climatic records of the subtropics contain valuable information about high-latitude climate variations and changes in the tropical hydrological balance. Hence, detailed subtropical climate records are crucial for true understanding of past climate dynamics and prediction of future conditions.

The Northwest Africa climate history describes the interplay of the African summer monsoon, the subtropical surface trade wind systems, and the North Atlantic current systems (Figure 1). Since marine records provide accurate datable and continuous information, we compare both paleoceanographic and paleo-aridity records constructed from a marine sediment core off NW Africa (Figure 1) with model simulations of the African climate.

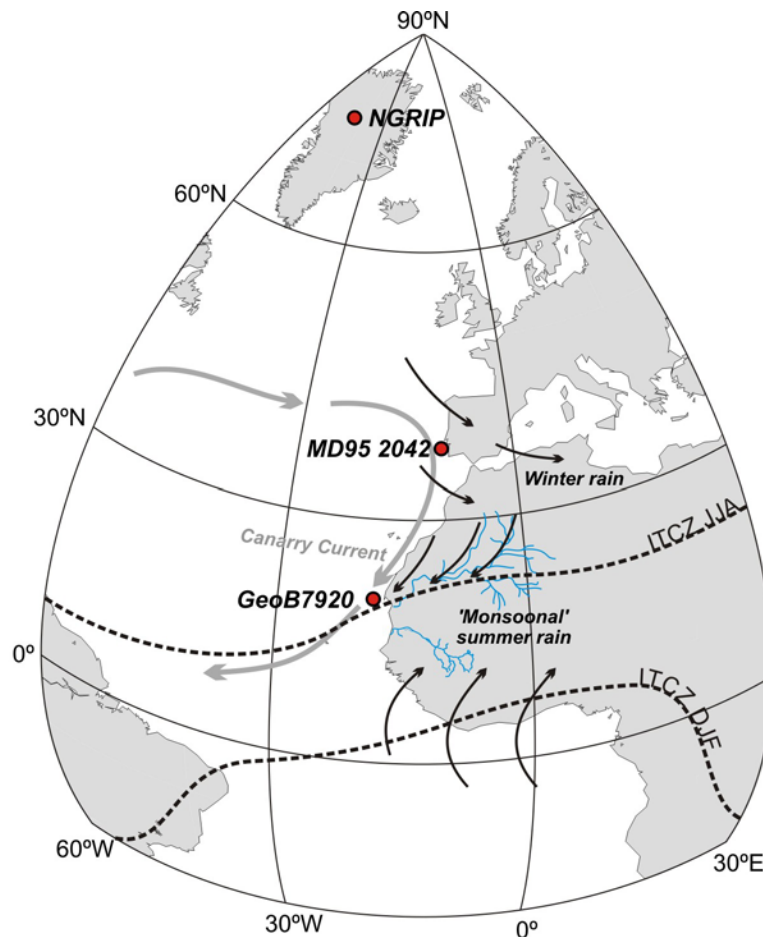


Figure 1. Map with locations of the sediment cores GeoB7920 and MD95 2042, the NGRIP ice core, the glacial North Atlantic surface circulation (grey arrows), and the major surface wind systems (black arrows) over Northwest Africa. The surface trade-wind systems located North and South of the Inter Tropical Convergence Zone (ITCZ; black dotted lines), and migrate seasonally along with the position of the ITCZ. The southeast trade wind system and bends to a southwest direction over West Africa as a humid monsoon flow during boreal summer when the ITCZ reaches its northern most position. North Atlantic Westerlies supply precipitation to the western Mediterranean region during boreal winter but also during glacial conditions (Moreno et al., 2005; Sánchez-Goni et al., 2002). At present, the Senegal River is the major river system discharging off northwest Africa, but there are strong indications of an active river system (Tamanrasset River) draining the Western Sahara during humid conditions (Vörösmarty et al., 2000). Sediment core MD95 2042 was used for construction of the age model (Shackleton et al., 2004) and the SST history of the eastern boundary current (Bard et al., 2004). The NGRIP ice core (NGRIP-members, 2004) is used as a paleoclimate record of the North Atlantic region.

Comparing geological proxy data and modelling results greatly attributes to our understanding of the driving forces and interpretation of geological proxy records on one hand, and enables to prove the quality of the modelling results on the other.

Sediment core GeoB7920 (20°45,09'N-18°34,90'W, 2278 m water depth) was retrieved off Northwest Africa during RV Meteor expedition M 53/1. We examined changes in the deep-water circulation and the Northwest African hydrological balance at the core location over the last glacial-interglacial cycle (~118 ka BP) (Figure 2). The $\delta^{18}\text{O}$ and $\delta^{13}\text{C}$ records of the benthic foraminifera *Cibicides wuellerstorfi* were measured at sub-millennial resolution (Figure 2) in order to construct the age model (see supplementary information) and the deepwater ventilation history related to changes in North Atlantic Deep Water (NADW) formation (Elliot et al., 2002; Vidal et al., 1997), respectively. The benthic $\delta^{18}\text{O}$ record is very similar to oxygen isotope stratigraphy of core MD95 2042 since both core locations are situated in NADW. Hence, the $\delta^{18}\text{O}$ record of GeoB7920 was tuned to the MD95 2042 isotope stratigraphy on GRIPss09sea age (Shackleton et al., 2004). The sub-millennial resolution of the benthic $\delta^{18}\text{O}$ record of core MD95 2042 was found to indicate significant fluctuations in the global ice volume and subsequent functions of the Antarctic temperature (Shackleton et al., 2004; Shackleton et al., 2000). Variations of the NW African continental hydrological conditions were derived from grain-size distributions of the total terrigenous fraction (sediment fraction free of carbonate, opal and organic matter), which are independent of carbonate dissolution effects. The paleohumidity is indicated by the proportion of the fine-grained terrigenous fraction calculated by the End Member Model Algorithm (Weltje, 1997), which is interpreted as the proportion fluvial-transported sediment (supplementary information). High proportions of the fluvial end-member indicate enhanced river input or reduced aeolian contributions to the total terrigenous fraction; both associated with increased humidity and expansion of the vegetation cover over Northwest Africa.

Two model simulations were acquired with the interactive atmosphere-ocean-vegetation (AOV) model of intermediate complexity CLIMBER-2 (supplementary information). The first simulation (AOV-IC) uses external forcing of orbitally induced insolation with prescribed variations in atmospheric CO_2 concentrations and prescribed inland ice variations derived from the sea level variations (Claussen et al., 2006). This simulation allocates the long-term climate variations over multiple precessional cycles (Figure 3). The second simulation, also performed with the CLIMBER-2 model, used prescribed freshwater forcing changes at high northern latitudes and associated changes in the Laurentian ice masses (Claussen et al., 2003b) (AOV-fresh) to simulate climate variations similar to the Heinrich

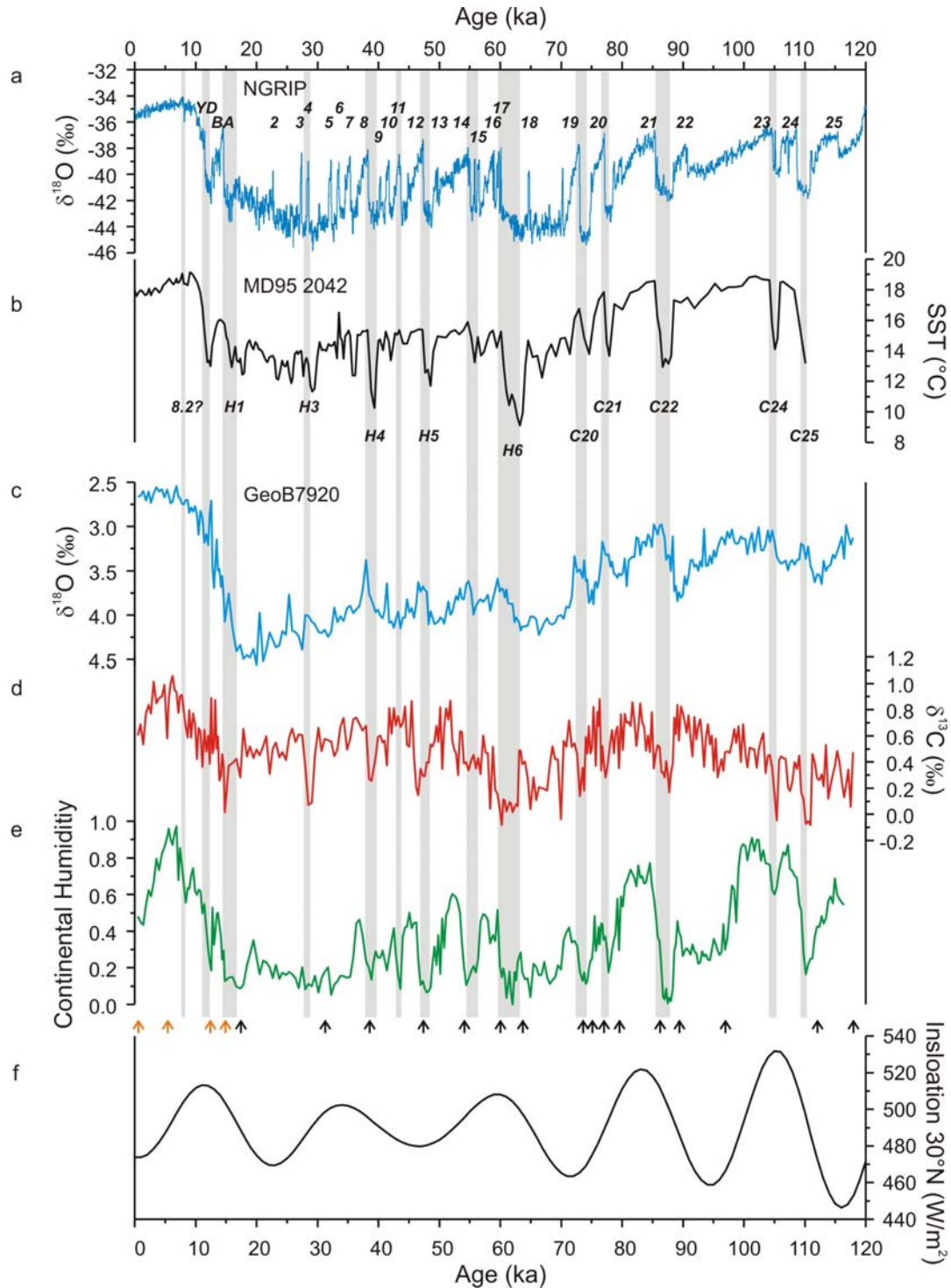


Figure 2. Paleoenvironmental records of the NGRIP ice core, sediment core MD95 2042, and sediment core GeoB7920 during the last glacial-interglacial cycle. a) Stable oxygen isotope stratigraphy of the NGRIP ice core indicating the Greenland temperature variations with Younger Dryas (YD), the Bolling-Allrod (BA), and the Greenland stadial events (2-25) (NGRIP-members, 2004). b) Alkenone SST reconstruction of the eastern boundary current from core MD95 2042 (Chapman et al., 2000). c-d) The stable isotope stratigraphy of benthic foraminifera *Cibicides wuellerstorfi* of core GeoB7920. e) The continental humidity represented by the fine-grained terrigenous end member (supplementary information) of core GeoB7920. The arrows at the bottom indicate the correlation points of the age model (supplementary information). f) Summer insolation at 30°N. The shaded areas indicate cold Greenland stadial events and North Atlantic Heinrich events.

and D-O events of MIS 3 (supplementary information). However, the prescribed fresh water pulses equivalent to Heinrich-rich events were not tuned to the geological dataset but were triggered every 7.5 ka. Therefore, only the simulated responds to Heinrich events, but not the timing can be compared with data.

Long-term variations of the continental humidity parallel the variations of the precession-forced low-latitude (30°N) summer insolation (Figure 2 A and B). Enhanced continental humidity occurs during maximum summer insolation both within MIS 5 and the early Holocene, the latter known as the AHP. The strong similarities between the humid periods strongly suggest identical humid conditions in the Saharan region during MIS 5 as found for the Holocene AHP (Gasse, 2000; Jolly et al., 1998). The two major humid phases of MIS 5 are interrupted by abrupt millennial-scale arid events associated with stadial events 25, 24, 22, 21, and 20 as recorded in the Greenland NGRIP record (NGRIP-members, 2004). These arid events have a similar footprint as the arid events that interrupt the Holocene AHP and co-occur with Heinrich event H1, the Younger Dryas, and the Holocene 8.2 event (Figure 2). We consider these short-term and abrupt arid events as interruptions of the rather gradual orbital-scale humid phases. The Holocene humidity variations of core GeoB7920 are in general agreement with Holocene palaeolake records in the Western Sahara and Sahel region although these show strong local variations (Gasse, 2002). More gradual orbital-paced climate variations were also suggested by Holocene humidity reconstructions in the northern Red Sea region (Arz et al., 2003), and by model simulations of high-frequency Holocene humidity in the western Saharan (Renssen et al., 2006).

The continental humidity record of GeoB7920 (Figure 2) indicates generally dry conditions during the glacial conditions from MIS 4 to MIS 2. However, humidity variations during MIS 3 indicate an alternation of millennial-scale humid and arid events that are very similar to high-latitude climate variations and seem to be independent of the insolation cycle and the African summer monsoon system (Figure 2). Enhanced humidity during MIS 3 interstadial events was also found in western Mediterranean climate records and have been enhanced moist production of the relatively warm North Atlantic SSTs and a southern position of the Azorean high-pressure system during glacial conditions (Allen et al., 1999; Martrat et al., 2004; Moreno et al., 2005; Sánchez-Goni et al., 2002). Our record suggests that the North Atlantic Westerly winter rains supplied large parts of Northwester Africa with precipitation during these interstadial humid events. The millennial-scale dry events recorded in core GeoB7920 coincide with abrupt variations up to ~ 0.7 ‰ in the benthic $\delta^{13}\text{C}$ record, and strongly reduced SSTs in the eastern boundary current off Portugal (Bard et al., 2004)

(Figure 2) indicating large-scale reorganization of the North Atlantic THC. Ice rafting events reduces or shuts off NADW formation and high-latitude cold conditions are transited southward within the eastern boundary current into the Mediterranean (Martrat et al., 2004) region and the eastern subtropical Atlantic (Chapman et al., 2000). These cold conditions in the Northeast Atlantic and the Mediterranean Sea (Cacho et al., 1999) cause arid conditions over Northwest Africa (Figure 2) and the western Mediterranean (Allen et al., 1999; Moreno et al., 2005; Sánchez-Goni et al., 2002). Hence, these data suggest the Northwest African hydrological balance strongly depends on high latitudinal glacial climate variations and Northeast Atlantic SSTs during MIS 3.

The mean annual temperature, the daily precipitation, and the vegetation cover of the Saharan grid box (20°N -30°N, 20°W -30°E) simulated with the AOV-IC model indicate predominantly precession-forced monsoonal variations (Figure 3B). The simulated vegetation

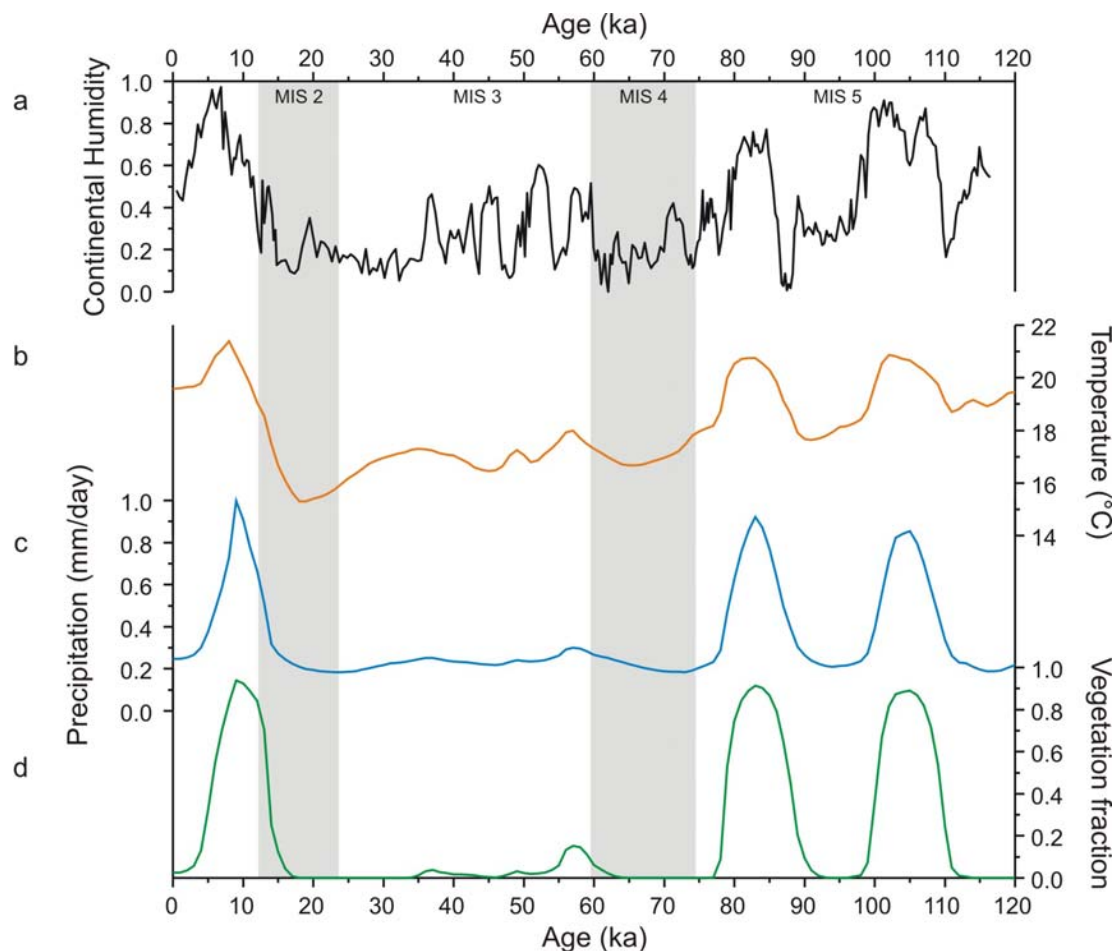


Figure 3. Comparisons of geological data and CLIMBER 2 AOV-IC model simulations (supplementary information). a) Northwest African continental humidity reconstruction from core GeoB7920 over the last ~120 ka. b-d) The AOV-IC model simulations of the mean annual temperature (°C), annual mean daily precipitation (mm/day), and vegetation cover (tree + grass fraction) over the Saharan region (20°N and 30°N) during the last interglacial-glacial cycle. The shaded areas show MIS 4 and MIS 2.

changes in the Saharan grid box are explained by the precession-forced increase of the monsoonal strength and a northward migration of the ITCZ that were further amplified by vegetation dynamics (Brovkin et al., 1998; Claussen et al., 1999; Renssen et al., 2003). The vegetation simulations of the AOV-IC model are highly consistent with the long-term humid periods of MIS 5 and the Holocene as recorded by the continental humidity record of core GeoB7920. These data evidently indicate that humid periods similar to the Holocene AHP occurred during MIS 5. North African pollen and plant macrofossil data of the Holocene AHP indicated that vegetation changes occurred due to a northerly extension of the monsoonal system combined with a southward expansion of Mediterranean vegetation (Jolly et al., 1998). The pronounced early Holocene humid interval in the northern Red Sea region related to a “Mediterranean Monsoon” (Arz et al., 2003) corroborates a strong Mediterranean contribution to the hydrological balance of Northern Africa due to the summer insolation variations. Thus, it is well possible that African humid periods result from the interaction of simultaneously enhanced influence of both the African Monsoon and the Mediterranean or North Atlantic precipitation over North Africa. The AOV-IC simulations indicate that precessional-forced humid periods are absent in the Sahara region during the glacial conditions whereas the humidity record of core GeoB7920 indicates relatively strong variations during MIS 3 (Figure 3). Obviously, the weaker precessional insolation cycles during the last interglacial were not strong enough to provoke orbital-scale humid conditions as recorded during MIS 5 and the early Holocene. Thus, the AOV-IC simulations substantiate the idea of additional sub-orbital forcing mechanism to explain the MIS 3 humid event.

The AOV-fresh model simulates the responds of the global climate system to prescribed freshwater forcing into the Northern Atlantic (supplementary information). This forcing triggers a response in the model-ocean and atmosphere, which realistically describes most features of reconstructed Heinrich events and D-O events (Ganopolski and Rahmstorf, 2002). We focus on the model simulations of the Sahel region since the desert conditions of the Sahara region lack significant variations in precipitation and vegetation cover during the last glacial period. The model results of the Sahelian region show that the simulated Heinrich and D-O events punctuate the long-term orbital forced variations that are parallel to the insolation curve (Figure 4 b-d). The temperature record simulated by the AOV-fresh model (Figure 4b) indicates a strong drop in temperature during Heinrich events, which is accompanied by abrupt reduction of the mean annual precipitation and vegetation fraction (Figure 4c-d). Moreover, simulated precipitation and vegetation variations of the Sahelian regions during MIS 3 respond relatively strong to Heinrich events and much weaker to humid

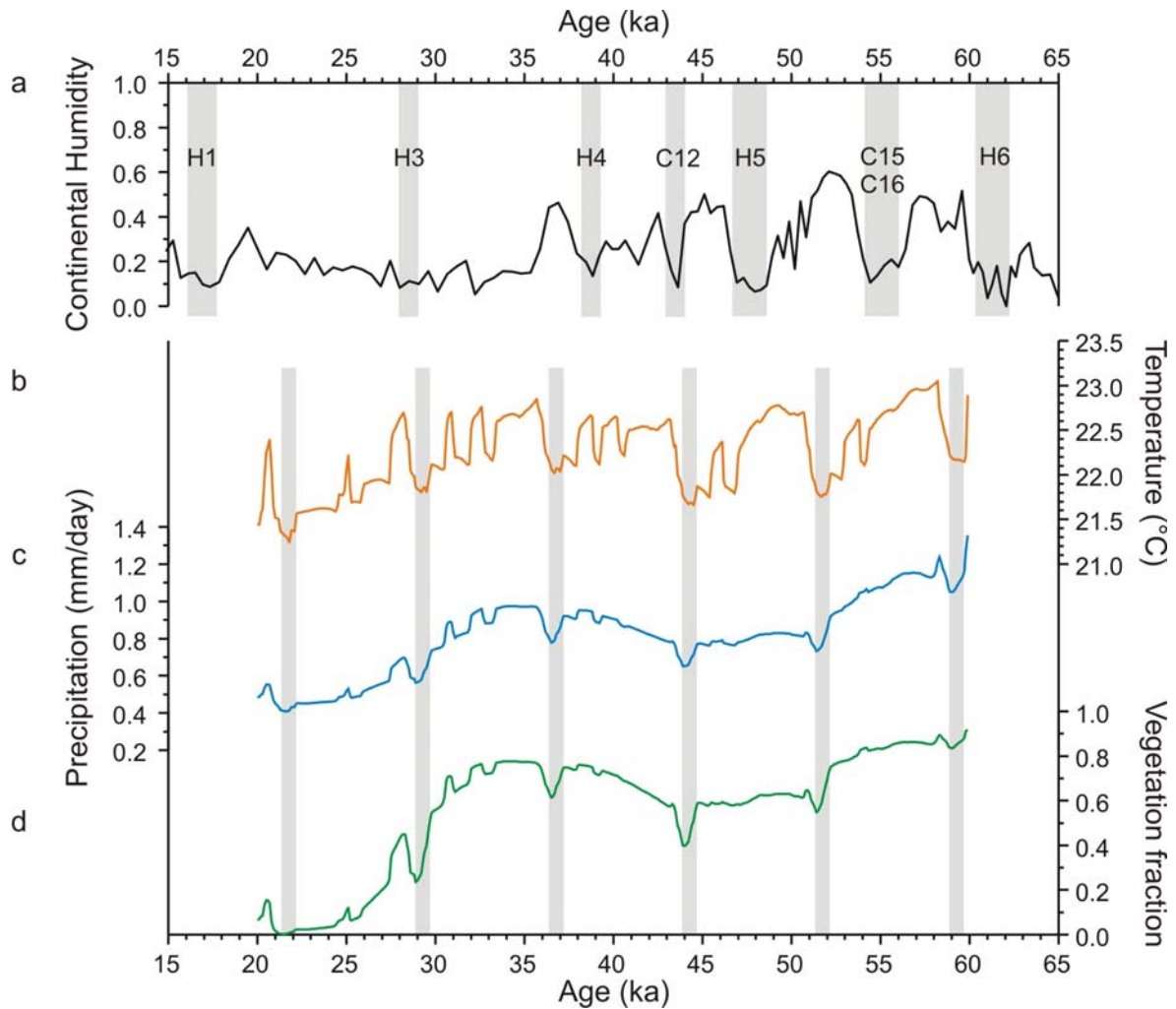


Figure 4. Comparisons of geological data and CLIMBER 2 AOV-fresh model simulations (supplementary information). a) Continental humid reconstruction of core GeoB7920. b-d) AOV-fresh simulations of the mean annual temperature, annual mean daily precipitation, and vegetation cover (tree + grass fraction) over the Saharan region (10°N and 20°N) for the period 60 to 20 ka BP. Shaded areas indicate Heinrich events (A) and modeled Heinrich like events (B-D).

events related to interstadial warm events. These abrupt arid events are in agreement with the humidity record of core GeoB7920 (Figure 4a) associated with ice rafting events and major reorganizations of the North Atlantic circulation (Figure 2). Significant orbital forced climate variations are not indicated by the geological data during MIS 3 due to the southern position of the ITCZ and the African monsoon system under glacial condition. Instead, the MIS 3 humid events indicated in core GeoB7920 conditions suggest enhanced influence of North Atlantic winter rain system (Allen et al., 1999; Moreno et al., 2005; Sánchez-Goni et al., 2002) over Northwest Africa during more moderate interstadial events. However, the orbital forced humid periods of MIS 5 and the AHP are punctuated by arid events associated with North Atlantic ice rafting events and subsequent reorganization of the North Atlantic

circulation (Figure 2) similar to the simulated dry events of MIS 3. Hence, High latitude fresh pulses cause extremely strong and abrupt acidification of Northwest Africa due to southerly advection of polar waters persisted within the eastern boundary current system reaching well into the eastern subtropical Atlantic (Chapman et al., 2000; deMenocal et al., 2000b) and the Mediterranean Sea (Cacho et al., 1999; Martrat et al., 2004).

The strong similarities between geological data and model simulations evidently show that precessional-forced humid periods, similar to the Holocene AHP, occur over multiple insolation cycles in Northern Africa. The rather gradual orbital-scale variations are punctuated by abrupt millennial-scale dry events associated to ice rafting North Atlantic ice rafting events during the last ~120 ka BP. Sever dry event that occur during humid periods of MIS 5 indicates that the impact of high latitude Heinrich like events are much stronger than the Orbital forced African monsoon. Besides a strong influence of Heinrich events, these data suggest that possible North Atlantic and Mediterranean moist sources had a significant influence on the Northwest African hydrological balance. Despite its coarse resolution, the model is able to simulate a realistic response of the Sahel region to Heinrich like events that are related to strong changes in the meridional overturning circulation in the North Atlantic Ocean. Hence, the combination of geological data and model result are an important advance in the understanding of the extreme climate variations of subtropical Africa on orbital and sub-orbital time scales.

Acknowledgements

We thank chief scientist H. Meggers, the captain; the crew and participants of Meteor cruise M53/1. G. J. Weltje is thanked for providing the End-Member Model Algorithm. The authors acknowledge the constructive discussion with A. Ganopolski, E. Bauer, V. Brovkin at the Potsdam Institute for Climate Impact Research, Germany, and M. Prins at the Vrije Universiteit Amsterdam, the Netherlands. M. Segl is thanked for carrying out the stable isotope measurements. This study is supported by the DFG as part of the DFG Research Center for Ocean Margins of the University of Bremen. This is RCOM publication No RCOM#.

Supporting material

Age model

The upper 14.8 ka of the age model of core GeoB7920 (Figure S1) was constructed by peak-to-peak correlation of the carbonate (CaCO_3) record of core GeoB7920 and the ^{14}C AMS dated record of ODP Site 658C (deMenocal et al., 2000a; deMenocal et al., 2000b), which was retrieved at the same geographical position. The age model prior to 14.8 ka is constructed by peak-to-peak correlation of the benthic (*Cibicides wuellerstorfi*) $\delta^{18}\text{O}$ record with benthic $\delta^{18}\text{O}$ stratigraphy of marine sediment core MD95 2042 (Cayre et al., 1999; Shackleton et al., 2004; Shackleton et al., 2000) on the GRIP ss09sea age scale (Johnsen et al., 2001). We performed a peak-to-peak correlation of the smoothed 5-point-average $\delta^{18}\text{O}$ records with the software package AnalySeries 1.1 (Paillard et al., 1996).

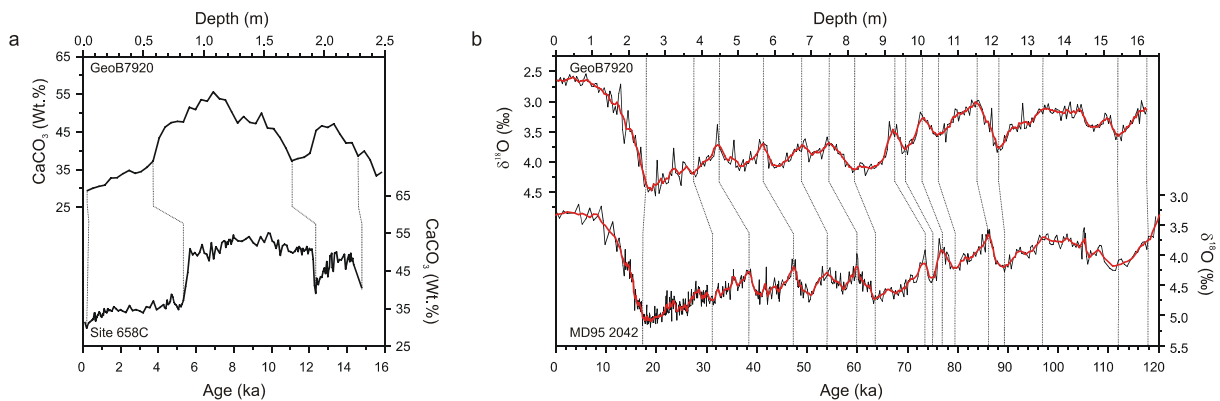


Figure S1. Age model of core GeoB7920. a) Correlation points (dotted black lines) of the carbonate records of GeoB7920 and Site658C (deMenocal et al., 2000a; deMenocal et al., 2000b) for the upper part of the core. b) Correlation points (dotted black lines) of the 5-point average (red line) of the $\delta^{18}\text{O}$ records of core GeoB7920 and MD95 2042 (Cayre et al., 1999; Shackleton et al., 2004; Shackleton et al., 2000).

Continental humidity

The terrigenous fraction was isolated by dissolving the carbonate, organic matter and biogenic opal content from $\sim 0.5\text{ml}$ bulk sediment. Random microscope observations were obtained to confirm the removal of all biogenic constituents. To avoid the fine-grained fraction to form aggregates, each sample was shortly boiled with about 300 mg of $\text{Na}_4\text{P}_2\text{O}_7 \cdot 10\text{H}_2\text{O}$ shortly before measuring. The grain-size distribution of each sample was analyzed with the Coulter LS200 laser particle sizer that measures particles in the range from 0.4 to 2000 μm in 92 size classes. All measurements were performed with degassed water and repeated 3 to 4 times to minimize the effect of air bubbles.

Statistically evident grain-size populations were calculated from the grain-size measurements with the end-member-modeling algorithm (EMMA) of *Weltje* (1997). The minimum number of dimensions, or end members (EMs), required for a satisfactory approximation of the data was established by calculation of the coefficient of determination (Prins and *Weltje*, 1999). The coefficients of determination represent the proportions of the variance of each variable that can be reproduced by the approximated data. The three-end-member model explains 88% of the total variance for the grain-size distributions of core GeoB7920. The three end members EM1, EM1, and EM3 have modal grain-sizes of 57.8 μm , 34.6 μm , and 4.9 μm , respectively (Figure S2).

The silt-sized end members EM1 and EM2 represent wind blown dust carried into the study area by the Northeast trade winds (*Holz et al.*, 2005; *Sarnthein and Koopmann*, 1980; *Weltje and Prins*, 2003). Off NW Africa, fluvial input is characterized by bimodal terrigenous grain-size distribution and with an excess of clay (*Sarnthein et al.*, 1981), which fits the distribution of EM3. End-members modeling of marine surface sediments off NW Africa indicated that the proportion fine-grained end member similar to EM3 increased in areas with enhanced fluvial activity (*Holz et al.*, 2004). Additionally, end-member modeling of terrigenous deep-sea sediments from the Arabic Sea and the subtropical Southeast Atlantic designated fine-grained end members similar to EM3 to fluvial transported mud (*Prins et al.*, 2000; *Stuut et al.*, 2002). We interpret EM3 as a hemipelagic end member that represents fluvial transported material.

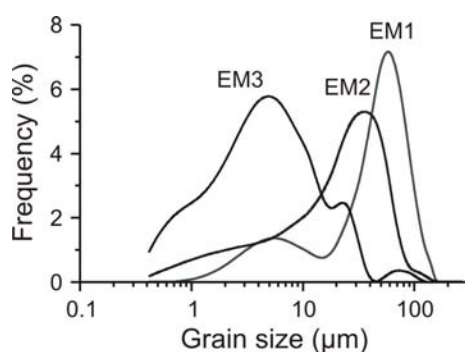


Figure S2. Grain-size distributions of the three end members obtained from the EMMA of the terrigenous sediment fraction. The silt-size end members (EM1 and EM2) are interpreted as eolian transported dust whereas the mud-sized end member (EM3) is interpreted as fluvial derived material.

CLIMBER-2 model and simulations

CLIMBER-2 encompasses a 2.5-dimensional statistical dynamical model of the atmosphere, a multibasin, zonally averaged ocean model, including sea ice dynamics, and a dynamical model of terrestrial vegetation which are coupled by fluxes of energy, water, and momentum (*Brovkin et al.*, 2002; *Ganopolski et al.*, 2001; *Petoukhov et al.*, 2000) The atmosphere model

has a coarse resolution of 10° in latitude and about 51° in longitude. The transport equations for temperature and humidity are solved on 10 vertical levels utilizing universal vertical profiles for temperature and humidity. The short-wave and long-wave radiation fluxes are calculated for 16 vertical layers accounting for evolving stratus and cumulus cloud coverage and average aerosol and ozone concentrations. The ocean model has zonally averaged basins for the Atlantic, the Indian Ocean, and the Pacific Ocean, which are connected by the Antarctic circumpolar current. The meridional resolution is 2.5° , and the vertical is resolved by 20 layers. Land grid cells have fractions of glacial cover and ice-free surface. The latter is separated into forest, grass and bare soil fractions, which interactively evolve under changes in climate. CLIMBER-2 has been validated against present-day climate and tested against comprehensive general circulation models and has been used successfully for a variety of paleoclimate studies (see the list of references in the Table of EMICs*).

The AOV-IC simulation uses external forcing of orbitally induced insolation variations (Berger and Loutre, 1991), prescribed atmospheric CO_2 concentrations (Petit et al., 1999), and prescribed inland ice derived from the sea level variations according to Waelbroeck et al (Claussen et al., 2006; Waelbroeck et al., 2002). In this study the age control of sea level variations has been modified using the orbital timescale of Martinson *et al.* (1987) (Martinson et al., 1987). The AOV-fresh simulation uses orbitally induced insolation variations and prescribed atmospheric CO_2 concentrations as in AOV-IC. To trigger Heinrich events in the model, freshwater is added to the Northern North Atlantic every 7.5 ka with corresponding changes in inland ice masses (Ganopolski and Rahmstorf, 2001). To trigger D-O events in CLIMBER-2, some small amount of freshwater is randomly added to the Northern North Atlantic (Ganopolski and Rahmstorf, 2002). The D-O events then emerge as stochastic resonance in the model. The combined forcing is used to explore the effects of Heinrich events and D-O events on the global climate system (Claussen et al., 2003a).

* M. Claussen (ed.), *Table of EMICs, Report 98, 55 pp., Potsdam Institute for Climate Impact Research. Available at PIK, P.O. Box 601203, 14412 Potsdam, Germany, or at <http://www.pik-potsdam.de/emics>*

- 6. Outlook and perspectives -

The thorough study on the quality of XRF core scanner data obtained from fine-grained marine sediments indicated that changing physical properties have only little influence on the quality of XRF measurements of relatively heavy elements. However, XRF measurements of the lighter elements Al and Si are severely influenced by the pooling water directly under the foil covering the split core surface of soft sediment. As indicated in Chapter 2, the water correction equations obtained from core GeoB7920 enable to correct element concentrations other sediment cores as well, despite the significant scatter on the correction equations themselves. However, repeating dry and wet sample measurements on different deep-sea lithologies would be a first step in order to confirm the consistency and reduce the analytical uncertainties of these correction equations. Although Cl intensities provide a good estimate of the water content in the sample volume analyzed by the XRF core scanner, they are also a source of the scatter in the correction equations (Tjallingii et al., *in press.*). However, accurate calibration of the water content in this small sample volume is technically not possible. The water content obtained from syringe samples is by far too inaccurate, and does not account for the water film that artificially increases the water content in the sample volume analyzed by the XRF core scanner. Hence, one of the outstanding tasks for future work will be to find a way to accurately determination of the water content.

Upwelling areas are known for strong regional variations of sedimentation patterns recorded at proximal locations close to the center of upwelling or more distal locations. Documentation of such regional variations in the upwelling area should be a main focus for future research in the region off Cape Blanc. One of the main preconditions to gain a better insight in past productivity and upwelling variations will be a reliable regional stratigraphy. The XRF core scanner is an excellent tool to obtain such spatial core-to-core correlations, when several well dated reference cores are at hand to cover the various distal and proximal sedimentation conditions (Kuhlmann et al., 2004). A spatial core-to-core correlation of the carbonate stratigraphy record was conducted for more distal sediments cores south of Cape Blanc (Wien et al., 2006). However, this carbonate stack lacks a reliable reference record to accurately reconstruct millennial and sub-millennial variations prior to the LGM. Additionally, the many section boundaries and discontinuities of ODP Site 658 complicate the interpretation of a detailed millennial- and sub-millennial scale stratigraphy prior to the LGM as well. The reliable and detailed stratigraphy of core GeoB7920 covers a continuous sedimentary record of the last glacial-interglacial cycle and forms an excellent reference core of the distal

stratigraphy off the Cape Blanc region. Future research should focus on accurately dated proximal stratigraphy of more proximal key locations within or close to the center of upwelling. Further studies should focus on possible zonal and meridional shifts of the upwelling center with respect sea level change and surface circulation variations of the Canary Current. Furthermore, these studies should focus on changes of marine productivity and upwelling intensity as result for changing trade wind intensity and trade wind zonality. However, interpretation of geological records from such complex regions demands regional model simulations that enable to distinct the influence of changing sea level, wind intensity, and wind zonality. Additionally, more information is needed about the actual source areas of the eolian transported material in order to calculate absolute paleo-wind strengths and accurately reconstruct past variations of the trade wind zonality.

The comprehensive collection of XRF data, grain-size analyses, and stable isotope data in combination with ocean-atmosphere-vegetation modeling model results document strong variations of the northwest African continental humidity during the last glacial-interglacial cycle. These data show that variations of the low-latitude African monsoon initiate African humid periods relative to precessional forced variations of the summer insolation. Northeast African records already suggested that the Mediterranean region could have been a potential moisture source during these humid periods (Arz et al., 2003). However, the importance of the Mediterranean region as possible moisture source over northwestern Africa is still unclear and needs more attention in future studies. Additionally, this study strongly suggests that D-O stadial events cause wide spread dry conditions over Northwest Africa. However, it is still unclear if the more humid continental conditions associated to D-O interstadial events are related to meridional shifts of the ITCZ, or these are related to migration of the North Atlantic temperate climate zones. Comparison of paleoclimate reconstructions along the Northwest African Margin will be essential to recover regional trends and provide additional information about the different forcing mechanisms of the Northwest African climate. Comparison of paleoclimate records off Senegal, Cape Blanc, and off Morocco is planned for the near future. To regard the role of the sub-tropical and tropical regions during D-O climate variations on a global perspective, future research should combine millennial-scale records from Cariaco Basin, Northwest Africa, the Red Sea area, Arabian Sea, Bay of Bengal, the Chinese Loess Plateau, and the Chinese Sea. Such a study will provide new insight about the monsoonal systems of different oceanic basins and the role of low-latitudes in possible teleconnection mechanisms and lateral atmospheric connections. A final aspect for future studies should regard repeating patterns of glacial-interglacial and

millennial-climate variations prior to MIS 5. Such studies are relevant in order to provide additional information about the consistency of climate variations over longer geological time scales.

References

- Abrantes, F. (2003). A 340,000 year continental climate record from tropical Africa - news from opal phytoliths from the equatorial Atlantic. *Earth and Planetary Science Letters* **209**, 165-179.
- Adkins, J., demenocal, P., and Eshel, G. (2006). The "African humid period" and the record of marine upwelling from excess ^{230}Th in Ocean Drilling Program Hole 658C. *Palaeoceanography* **21**, PA4203, doi:10.1029/2005PA001200.
- Allen, J. R. M., Brandt, U., Brauer, A., Hubberten, H.-W., Huntley, B., Keller, J., Kraml, M., Mackensen, A., Mingram, J., Negendank, J. F. W., Nowaczyk, N. R., Oberhansli, H., Watts, W. A., Wulf, S., and Zolitschka, B. (1999). Rapid environmental changes in southern Europe during the last glacial period. *Nature* **400**, 740-743.
- Alley, R. B. (1998). Palaeoclimatology: Icing the North Atlantic. *Nature* **392**, 335-337.
- Alley, R. B., Marotzke, J., Nordhaus, W. D., Overpeck, J. T., Peteet, D. M., Pielke, R. A., Pierrehumbert, R. T., Rhines, P. B., Stocker, T. F., Talley, L. D., and Wallace, J. M. (2003). Abrupt climate change. *Science* **299**, 2005-2010.
- Arz, H. W., Gerhardt, S., Pätzold, J., and Röhl, U. (2001). Millennial-scale changes of surface- and deep-water flow in the western tropical Atlantic linked to Northern Hemisphere high-latitude climate during the Holocene. *Geology* **29**, 239-242.
- Arz, H. W., Lamy, F., Pätzold, J., Müller, P. J., and Prins, M. (2003). Mediterranean Moisture Source for an Early-Holocene Humid Period in the Northern Red Sea. *Science* **300**, 118-121.
- Bahr, A., Lamy, F., Arz, H., Kuhlmann, H., and Wefer, G. (2005). Late glacial to Holocene climate and sedimentation history in the NW Black Sea. *Marine Geology* **214**, 309-322.
- Balsam, W. L., Otto-Bliesner, B. L., and Deaton, B. C. (1995). Modern and last glacial maximum eolian sedimentation patterns in the Atlantic Ocean interpreted from sediment iron oxide content. *Paleoceanography* **10**, 493-507.
- Bard, E., Rostek, F., and Menot-Combes, G. (2004). Radiocarbon calibration beyond 20,000 ^{14}C yr B.P. by means of planktonic foraminifera of the Iberian Margin. *Quaternary Research* **61**, 204-214.
- Bard, E., Rostek, F., Turon, J.-L., and Gendreau, S. (2000). Hydrological Impact of Heinrich Events in the Subtropical Northeast Atlantic. *Science* **289**, 1321-1324.
- Barton, E. D. (1998). Eastern Boundary of the Atlantic: Northwest Africa and Iberia. In "The Sea." (A. R. Robinson, and K. H. Brink, Eds.), pp. 633-657. John Wiley & Sons, Inc., New York.
- Berger, A., and Loutre, M. F. (1991). Insolation values for the climate of the last 10 million years. *Quaternary Science Review* **10**, 297-317.
- Bertrand, P., Pedersen, T. F., Martinez, P., Calvert, S., and Shimmiel, G. (2000). Sea level impact on nutrient cycle in coastal upwelling areas during deglaciation: Evidence from nitrogen isotopes. *Global Biogeochemical Cycles* **14**, 341-355.
- Bertrand, P., Shimmiel, G., Martinez, P., Grousset, F., Jorissen, F., Paterne, M., Pujol, C., Bouloubassi, I., Menard, P. B., and Peypouquet, J. P. (1996). The glacial ocean productivity hypothesis: the importance of regional temporal and spatial studies. *Marine Geology* **130**, 1-9.
- Blunier, T. (1998). Asynchrony of Antarctic and Greenland climate change during the last glacial period. *Nature* **394**, 739-743.
- Blunier, T., and Brook, E. (2001). Timing of millennial-scale climate change in Antarctica and Greenland during the last glacial period. *Science* **291**, 109-112.
- Bond, G., Broecker, W., Johnson, A., McManus, J., Labeyrie, L., Jouzel, J., and Bonani, G. (1993). Correlations between climate records from North Atlantic sediments and Greenland ice-core. *Nature* **365**, 143-147.

- Bond, G., Kromer, B., Beer, J., Muscheler, R., Evans, M. N., Showers, W., Hoffmann, S., Lotti-Bond, R., Hajdas, I., and Bonani, G. (2001). Persistent solar influence on north Atlantic climate during the Holocene. *Science* **294**, 2130-2136.
- Bond, G. C., Heinrich, H., Broecker, W. S., Labeyrie, L., McManus, J. F., Andrews, J., Huon, S., Jantschik, R., Clasen, S., Simet, C., Tedesco, K., Klas, M., Bonani, G. G., and Ivy, S. (1992). Evidence for massive discharges of icebergs into the North Atlantic Ocean during the last glacial period. *Nature* **360**, 245-249.
- Broecker, W., Bond, G., Klas, M., Clark, E., and McManus, J. (1992). Origin of the northern Atlantic's Heinrich events. *Climate Dynamics* **6**, 265-273.
- Broecker, W., Peteet, D. M., and Rind, D. (1985). Does the ocean-atmosphere system have more than one stable mode of operation? *Nature* **315**, 21-26.
- Broecker, W. S. (1994). Massive iceberg discharges as triggers for global climate change. *Nature* **372**, 421-424.
- Broecker, W. S. (2003). Does the Trigger for Abrupt Climate Change Reside in the Ocean or in the Atmosphere? *Science* **300**, 1519-1522.
- Brovkin, V., Bendtsen, J., Claussen, M., Ganopolski, A., Kubatzki, C., Petoukhov, V., and Andreev, A. (2002). Carbon cycle, vegetation, and climate dynamics in the Holocene: Experiments with the CLIMBER-2 model. *Global Biogeochemical Cycles* **16**, 1139, doi:10.1029/2001GB001662.
- Brovkin, V., Claussen, M., Petoukhov, V., and Ganopolski, A. (1998). On the stability of the atmosphere-vegetation system in the Sahara/Sahel region. *Journal of Geophysical Research* **103**, 31,613-31,624.
- Cacho, I., Grimalt, J. O., Pelejero, C., Canals, M., Sierro, F. J., Flores, J. A., and Shackleton, N. J. (1999). Dansgaard-Oeschger and Heinrich event imprints in Alboran Sea paleotemperatures. *Paleoceanography* **14**, 698-705.
- Cayre, O., Lancelot, Y., and Vincent, E. (1999). Paleoceanographic reconstructions from planktic foraminifera off the Iberian Margin: Temperature, salinity, and Heinrich events. *Paleoceanography* **14**, 384-396.
- Chapman, M. R., N.J., S., and Duplessy, J.-C. (2000). Sea surface temperature variability during the last glacial-interglacial cycle: assessing the magnitude and pattern of climate change in the North Atlantic. *Palaeogeography, Palaeoclimatology, Palaeoecology* **157**, 1-25.
- Chapman, M. R., N.J. Shackleton, M. Zhao, and G. Eglinton. (1996). Faunal and alkenone reconstructions of subtropical North Atlantic surface hydrography and paleotemperature over the last 28 kyr. *Paleoceanography* **11**, 343-357.
- Chapman, M. R., and Shackleton, N. J. (1998). Millennial-scale fluctuations in North Atlantic heat flux during the last 150,000 years. *Earth Planet. Sci. Lett.* **159**, 57-70.
- Chiapello, I., Bergametti, G., Gomes, L., Chatenet, B., Dulac, F., Pimenta, J., and Santos Soares, E. (1995). An additional low layer transport of Sahelian and Saharan dust over the North-Eastern Tropical Atlantic. *Geophysical Research Letters* **22**, 3191-3194.
- Claussen, M., Brovkin, V., Ganopolski, A., Kubatzki, C., and Petoukhov, V. (2003a). Climate Change in Northern Africa: The Past is Not the Future. *Climatic Change* **57**, 99-118.
- Claussen, M., Fohlmeister, J., Ganopolski, A., and Brovkin, V. (2006). Vegetation dynamics amplifies precessional forcing. *Geophysical Research Letters* **33**, L09709.
- Claussen, M., Ganopolski, A., Brovkin, V., Gerstengarbe, F. W., and Werner, P. (2003b). Simulated global-scale response of the climate system to Dansgaard/Oeschger and Heinrich events. *Climate Dynamics* **21**, 361-370.
- Claussen, M., Kubatzki, C., Brovkin, V., Ganopolski, A., Hoelzmann, P., and Pachur, H.-J. (1999). Simulation of an abrupt change in Saharan vegetation in the mid-Holocene. *Geophysical Research Letters* **26**, 2037-2040.

- Clemens, S. C. (2005). Millennial-band climate spectrum resolved and linked to centennial-scale solar cycles. *Quaternary Science Reviews* **24**, 521-531.
- Combourieu Nebout, N., J.L. Turon, R. Zahn, L. Capotondi, L. Londeix, and K. Pahnke. (2002). Enhanced aridity and atmospheric high-pressure stability over the western Mediterranean during the North Atlantic cold events of the past 50 k.y. *Geology* **30**, 863-866.
- Conkright, M. E., Locarnini, R. A., Garcia, H. E., O'Brien, T. D., Boyer, T. P., Stephens, C., and Antonov, J. I. (2002). World Ocean Atlas 2001: Objective Analyses, Data Statistics, and Figures, CD-ROM Documentation. Silver Spring, MD. pp. 17.
- Dannenmann, S., B.K. Linsley, D.W. Oppo, Y. Rosenthal, and L. Beaufort. (2003). East Asian monsoon forcing of suborbital variability in the Sulu Sea during Marine Isotope Stage 3: Link to Northern Hemisphere climate. *Geochemistry, Geophysics Geosystems* **4**, 1001, doi:10.1029/2002GC000390.
- Dansgaard, W. (1993). Evidence for general instability of past climate from a 250-kyr ice-core record. *Nature* **364**, 218-220.
- Dansgaard, W., Johnsen, S. J., Clausen, H. B., Dahl-Jensen, D., Gundestrup, N. S., and Hammer, C. U. (1984). North Atlantic climatic oscillations revealed by deep Greenland ice cores. In "Climate Processes and Climate Sensitivity." (J. E. Hansen, and T. Takahashi, Eds.), pp. 288-298. American Geophysical Union, Washington, D.C.
- deMenocal, P. (1995). Plio-Pleistocene African Climate. *Science* **270**, 53-59.
- deMenocal, P. B., Ortiz, J., Guilderson, T., Adkins, J., Sarnthein, M., Baker, L., and Yarusinsky, M. (2000a). Abrupt onset and termination of the African Humid period: rapid climate response to gradual insolation forcing. *Quaternary Science Reviews* **19**, 347-361.
- deMenocal, P. B., Ortiz, J., Guilderson, T., and Sarnthein, M. (2000b). Coherent high- and low-latitude climate variability during the Holocene Warm Period. *Science* **288**, 2198-2202.
- deMenocal, P. B., and Rind, D. (1993). Sensitivity of Asian and African climate to variations in seasonal insolation, glacial ice cover, sea surface temperature, and Asian orography. *Journal of Geophysical Research* **98**, 7265-7287.
- Elliot, M., Labeyrie, L., and Duplessy, J.-C. (2002). Changes in North Atlantic deep-water formation associated with the Dansgaard-Oeschger temperature oscillations (60-10 ka). *Quaternary Science Reviews* **21**, 1153-1165.
- Freudenthal, T., Meggers, H., Henderiks, J., Kuhlmann, H., Moreno, A., and Wefer, G. (2002). Upwelling intensity and filament activity off Morocco during the last 250,000 years. *Deep-Sea Research Part II* **49**, 3655-3674.
- Ganopolski, A., Petoukhov, V., Rahmstorf, S., Brovkin, V., Claussen, M., Eliseev, A., and Kubatzki, C. (2001). CLIMBER-2: a climate system model of intermediate complexity. Part II: model sensitivity. *Climate Dynamics* **17**, 735-751.
- Ganopolski, A., and Rahmstorf, S. (2002). Abrupt glacial climate changes due to stochastic resonance. *Physical Review Letters* **88**, doi:10.1103/PhysRevLett.88.038501.
- Ganopolski, A., and Rahmstorf, S. (2001). Rapid changes of glacial climate simulated in coupled climate model. *Nature* **409**, 153-158.
- Gasse, F. (2000). Hydrological changes in the African tropics since the Last Glacial Maximum. *Quaternary Science Reviews* **19**, 189-211.
- Gasse, F. (2002). Diatom-inferred salinity and carbonate oxygen isotopes in Holocene waterbodies of the Western Sahara and Sahel. *Quaternary Science Reviews* **21**, 737-767.

- Gasse, F., Tehet, R., Durand, A., Gibert, E., and Fontes, J. C. (1990). The arid-humid transition in the Sahara and the Sahel during the last deglaciation. *Nature* **346**, 141-146.
- Ge, L., Lai, W., and Lin, Y. (2005). Influence of and correction for moisture in rocks, soils and sediments on *in situ* XRF analysis. *X-Ray Spectrometry* **34**, 28-34.
- Glaccum, R. A., and Prospero, J. M. (1980). Saharan aerosols over the tropical North Atlantic - mineralogy. *Marine Geology* **37**, 295-321.
- Grimm, E. C., Jacobsen, G. L., Watts, W. A., Hansen, B. C. S., and Maasch, K. A. (1993). A 50,000-Year Record of Climate Oscillations from Florida and its Temporal Correlation with the Heinrich Events. *Science* **261**, 198-200.
- Grützner, J., Hillenbrand, C.-D., and Rebesco, M. (2005). Terrigenous flux and biogenic silica deposition at the Antarctic continental rise during the late Miocene to early Pliocene: implications for ice sheet stability and sea ice coverage. *Global and Planetary Change* **45**, 131-149.
- Hagen, E. (2001). Northwest African upwelling scenario. *Oceanologica Acta* **24**, S113-S128.
- Harris, P. G., Zhao, M., Rosell-Mele, A., Tiedemann, R., Sarnthein, M., and Maxwell, J. R. (1996). Chlorin accumulation rate as a proxy for Quaternary marine primary productivity. *Nature* **383**, 63-65.
- Haug, G. H., Hughen, K. A., Sigman, D. M., Peterson, L. C., and Röhl, U. (2001). Southward migration of the Intertropical Convergence Zone Through the Holocene. *Science* **293**, 1304-1308.
- Heinrich, H. (1988a). Origin and consequences of cyclic ice-rafting in the northeast Atlantic ocean, during the past 130,000 years. *Quaternary Research* **29**, 143-152.
- Heinrich, H. (1988b). Origin and consequences of cyclic ice rafting in the Northeast Atlantic Ocean during the past 130,000 years. *Quaternary Research* **29**, 142.
- Helmke, P., Romero, O., and Fischer, G. (2005). Northwest African upwelling and its effect on offshore organic carbon export to the deep sea. *Global Biogeochemical Cycles* **19**, GB4015, doi:10.1029/2004GB002265.
- Hemming, S. R. (2004). Heinrich events: Massive late Pleistocene detritus layers of the North Atlantic and their global climate imprint. *Review of Geophysics* **42**, RG1005, doi:10.1029/2003RG000128.
- Hepp, D. A., Mörz, T., and Grützner, J. (2006). Pliocene glacial cyclicality in a deep-sea sediment drift (Antarctic Peninsula Pacific Margin). *Palaeogeography, Palaeoclimatology, Palaeoecology* **231**, 181-198.
- Holz, C., Stuut, J.-B. W., and Henrich, R. (2004). Terrigenous sedimentation processes along the continental margin off NW-Africa: implications from grain-size analyses of surface sediments. *Sedimentology* **51**, 1145-1154.
- Holz, C. (2005). "Climate-induced variability of fluvial and eolian sediment supply and gravity-driven sediment transport off Northwest Africa." Dissertation (PhD Thesis), Universität Bremen, pp. 129.
- Ivanochko, T. S., Ganeshram, R. S., Brummer, G.-J. A., Ganssen, G., Jung, S. J. A., Moreton, S. G., and Kroon, D. (2005). Variations in tropical convection as an amplifier of global climate change at the millennial scale. *Earth and Planetary Science Letters* **235**, 302-314.
- Jaccard, S. L., Haug, G. H., Sigman, D. M., Pedersen, T. F., Thierstein, H. R., and Röhl, U. (2005). Glacial/Interglacial Changes in Subarctic North Pacific Stratification. *Science* **308**, 1003-1006.
- Jansen, J. H. F., Van der Gaast, S. J., Koster, B., and Vaars, A. J. (1998). CORTEX, a shipboard XRF-scanner for element analyses in split sediment cores. *Marine Geology* **151**, 143-153.
- Jenkins, R., and de Vries, J. L. (1970). "Practical X-ray spectrometry." MacMillan, London.

- Johnsen, S. J., Dahl-Jensen, D., Gundestrup, N., Steffensen, J. P., Clausen, H. B., Miller, H., Masson-Delmotte, V., Sveinbjörnsdóttir, A. E., and White, J. (2001). Oxygen isotope and palaeotemperature records from six Greenland ice-core stations: Camp Century, Dye-3, GRIP, GISP2, Renland and NorthGRIP. *Journal of Quaternary Science* **16**, 299-307.
- Jolly, D., Harrison, S. P., Damnati, B., and Bonnefille, R. (1998). Simulated climate and biomes of Africa during the late quaternary: comparison with pollen and lake status data. *Quaternary Science Reviews* **17**, 629-657.
- Kanfoush, S. L., Hodell, D. A., Charles, C. D., Guilderson, T. P., Mortyn, P. G., and Ninnemann, U. S. (2000). Millennial-Scale Instability of the Antarctic Ice Sheet During the Last Glaciation. *Science* **288**, 1815-1819.
- Kanfoush, S. L., Hodell, D. A., Charles, C. D., Janecek, T. R., and Rack, F. R. (2002). Comparison of ice-rafted debris and physical properties in ODP Site 1094 (South Atlantic) with the Vostok ice core over the last four climatic cycles. *Palaeogeography, Palaeoclimatology, Palaeoecology* **182**, 329 - 349.
- Kido, Y., Koshikawa, T., and Tada, R. (2006). Rapid and quantitative major element analysis method for wet fine-grained sediments using an XRF microscanner. *Marine Geology* **229**, 209-225.
- Knutti, R., Fluckiger, J., Stocker, T. F., and Timmermann, A. (2004). Strong hemispheric coupling of glacial climate through freshwater discharge and ocean circulation. *Nature* **430**, 851-856.
- Koopmann, B. (1979). "Saharastaub in den Sedimenten des subtropisch-tropischen Nordatlantik während der letzten 20.000 Jahre." Ph.D., Christian-Albrechts-Universität Kiel, pp. 108.
- Koopmann, B. (1981). Sedimentation von Saharastaub im subtropischen Nordatlantik während der letzten 25.000 Jahre. *Meteor Forschungsergebnisse C* **35**, 23-59.
- Koshikawa, T., Kido, Y., and Tada, R. (2003). High-resolution rapid elemental analysis using an XRF microscanner. *Journal of Sedimentary Research* **73**, 824-829.
- Krastel, S., Hanebuth, T. J. J., Antobreh, A. A., Heinrich, R., Holz, C., Kölling, M., Schulz, H. D., Wien, K., and Wynn, R. B. (2004). Cap Tamiris Canyon: A newly discovered channel system offshore of Mauritania. *EOS* **85**, 417-432.
- Kuhlmann, H. (2004). "Reconstruction of the sedimentary history offshore NW Africa: Application of core-logging tools." Dissertation, Universität Bremen, pp. 103.
- Kuhlmann, H., Freudenthal, T., Helmke, P., and Meggers, H. (2004). Reconstruction of paleoceanography off NW Africa during the last 40,000 years: influence of local and regional factors on sedimentation accumulation. *Marine Geology* **207**, 209-224.
- Kutzbach, J. E., and Liu, Z. (1997). Response of the African Monsoon to Orbital Forcing and Ocean Feedbacks in the Middle Holocene. *Science* **278**, 440-443.
- Kutzbach, J. E., and Street-Perrott, F. A. (1985). Milankovitch forcing of fluctuations in the level of tropical lakes from 18 to 0 kyr BP. *Nature* **317**, 130-134.
- Lamy, F., Hebbeln, D., Röhl, U., and Wefer, G. (2001). Holocene rainfall variability in southern Chile: a marine record of latitudinal shifts of the Southern Westerlies. *Earth and Planetary Science Letters* **185**, 369-382.
- Leuschner, D. C., and Sirocko, F. (2000). The low-latitude monsoon climate during Dansgaard-Oeschger cycles and Heinrich Events. *Quaternary Science Reviews* **19**, 243-254.
- Little, M. G., R.S. Schneider, D. Kroon, B. Price, C.P. Summerhayes, and M. Segl. (1997). Trade wind forcing of upwelling, seasonality, and Heinrich events as a response to Sub-Milankovitch climate variability. *Paleoceanography* **12**, 568-576.
- Liu, L., Chen, J., Ji, J., Chen, Y., and Balsam, W. (2006). Variation of Zr/Rb ratios in the Chinese loess deposits during the past 1.8 Myr and its implications for the change of

- East Asian monsoon intensity. *Geochemistry, Geophysics, Geosystems* **7**,
 doi:10.1029/2005GC001188.
- MacAyeal, D. (1995). Challenging an ice-core paleothermometer. *Science* **270**, 444-445.
- MacAyeal, D. R. (1993). A low-order model of the Heinrich event cycle. *Paleoceanography* **8**, 767-773.
- Martinez, P., Bertrand, P., Bouloubassi, I., Bareille, G., Shimmield, G., Vautravers, B., Grousset, F., Guichard, S., Ternois, Y., and Sicre, M. A. (1996). An integrated view of inorganic and organic biogeochemical indicators of palaeoproductivity changes in a coastal upwelling area. *Organic Geochemistry* **24**, 411-420.
- Martinez, P., Bertrand, P., Shimmield, G., Cochran, K., Jorissen, F. J., Foster, J., and Dignan, M. (1999). Upwelling intensity and ocean productivity changes off Cape Blanc (northwest Africa) during the last 70,000 years: geochemical and micropaleontological evidence. *Marine Geology* **158**, 57-74.
- Martinson, D. G., Pisias, N. G., Hays, J. D., Imbrie, J., Moore, T. C., Jr., and Shackleton, N. J. (1987). Age dating and the orbital theory of the ice ages: development of a high-resolution 0 to 300,000-year chronostratigraphy. *Quaternary Research* **27**, 1-29.
- Martrat, B., Grimalt, J. O., Lopez-Martinez, C., Cacho, I., Sierro, F. J., Flores, J. A., Zahn, R., Canals, M., Curtis, J. H., and Hodell, D. A. (2004). Abrupt Temperature Changes in the Western Mediterranean over the Past 250,000 Years. *Science* **306**, 1762-1765.
- Matthewson, A. P., Shimmield, G. B., and Kroon, D. (1995). A 300 kyr high-resolution aridity record of the North African continent. *Paleoceanography* **10**, 677-692.
- McIntyre, A., and Molino, B. (1996). Forcing of Atlantic Equatorial and Subpolar Millennial Cycles by Precession. *Science* **274**, 1867-1870.
- Meggers, H., Prange, M., Freudenthal, T., Kuhlmann, H., Schulz, M., Hensen, C., and Plewa, K. (*unpublished*). African humid episodes during the last glaciation.
- Meggers, H. and cruise participants (2002). Report and preliminary results of Meteor cruise M 53/1, Limasol - Las Palmas-Mindelo, 30.03 - 03.05.2002. In "Berichte, Fachbereich Geowissenschaften." pp. 81. Universität Bremen, Bremen.
- Mittelstaedt, E. (1991). The ocean boundary along the northwest African coast: Circulation and oceanographic properties at the sea surface. *Progress in Oceanography* **26**, 307-355.
- Moreno, A., Cacho, I., Canals, M., Grimalt, J. O., Sanchez-Goni, M. F., Shackleton, N., and Sierro, F. J. (2005). Links between marine and atmospheric processes oscillating on a millennial time-scale. A multi-proxy study of the last 50,000 yr from the Alboran Sea (Western Mediterranean Sea). *Quaternary Science Reviews* **24**, 1623-1636.
- Moreno, A., Nave, S., Kuhlmann, H., Canals, M., Targarona, J., Freudenthal, T., and Abrantes, F. (2002). Productivity response in the North Canary Basin to climate changes during the last 250,000 yr: a multi-proxy approach. *Earth and Planetary Science Letters* **196**, 147-159.
- Moseley, H. G. J. (1914). The high-frequency spectra of the elements. II. *Philosophical Magazine* **27**, 703-714.
- Müller, P. J., and Schneider, R. (1993). An automated leaching method for the determination of opal in sediments and particulate matter. *Deep-sea Research* **40**, 425-444.
- NGRIP-members. (2004). High-resolution record of Northern Hemisphere climate extending into the last interglacial period. *Nature* **431**, 147-151.
- Nicholson, S. E. (2000). The nature of rainfall variability over Africa on time scales of decades to millenia. *Global and Planetary Change* **26**, 137-158.
- Paillard, D., Labeyrie, L., and Yiou, P. (1996). Macintosh program performs time-series analysis. *Eos Trans. AGU* **77**, 379.

- Pailler, D., and Bard, E. (2002). High frequency paleoceanographic changes during the past 140 000 yr recorded by the organic matter in sediments of the Iberian Margin. *Palaeogeography, Palaeoclimatology, Palaeoecology* **181**, 431-452.
- Parkin, D. W., and Shackleton, N. J. (1973). Trade wind and temperature correlations down a deep-sea core off the Saharan coast. *Nature* **245**, 455-457.
- Peterson, L. C., Haug, G. H., Hughen, K. A., and Rohl, U. (2000). Rapid Changes in the Hydrologic Cycle of the Tropical Atlantic During the Last Glacial. *Science* **290**, 1947-1951.
- Petit, J. R., Jouzel, J., Raynaud, D., Barkov, N. I., Barnola, J. M., Basile, I., Bender, M., Chappellaz, J., Davis, M., Delaygue, G., Delmotte, M., Kotlyakov, V. M., Legrand, M., Lipenkov, V. Y., Lorius, C., Pepin, L., Ritz, C., Saltzman, E., and Stievenard, M. (1999). Climate and atmospheric history of the past 420,000 years from the Vostok ice core, Antarctica. *Nature* **399**, 429-436.
- Petoukhov, V., Ganopolski, A., Brovkin, V., Claussen, M., Eliseev, A., Kubatzki, C., and Rahmstorf, S. (2000). CLIMBER-2: a climate system model of intermediate complexity. Part I: model description and performance for present climate. *Climate Dynamics* **16**, 1-17.
- Pokras, E. M., and Mix, A. C. (1985). Eolian evidence for spatial variability of Late Quaternary climates in Tropical Africa. *Quaternary Research* **24**, 137-149.
- Potts, P. J. (1987). "A handbook of silicate rock analysis." Blackie, Glasgow. pp. 662.
- Prentice, I. C., Jolly, D., and participants, B. (2000). Mid-Holocene and glacial-maximum vegetation geography of the northern continents and Africa. *Journal of Biogeography* **27**, 507.
- Prins, M. A., Postma, G., and Weltje, G. J. (2000). Controls on terrigenous sediment supply to the Arabian Sea during the late Quaternary: the Makran continental slope. *Marine Geology* **169**, 351-371.
- Prins, M. A., and Weltje, G. J. (1999). End-member modeling of siliciclastic grain-size distributions: the Late Quaternary record of eolian and fluvial sediment supply to the Arabian Sea and its paleoclimatic significance. In "Numerical experiments in stratigraphy: Recent advances in stratigraphic and sedimentologic computer simulations. SEPM Special Publication 62." (J. Harbaugh, L. Watney, G. Rankey, R. Slingerland, R. Goldstein, and E. Franseen, Eds.), pp. 91-111. Society for Sedimentary Geology.
- Prospero, J. M., and Lamb, P. J. (2003). African Droughts and Dust Transport to the Caribbean: Climate Change Implications. *Science* **302**, 1024-1027.
- Pye, K. (1987). Aeolian dust and dust deposits. Academic Press, London. pp. 334.
- Rahmstorf, S. (2002). Ocean circulation and climate during the past 120,000 years. *Nature* **419**, 207-214.
- Ramsey, M. H., Potts, P. J., Webb, P. C., Watkins, P., Watson, J. S., and Coles, B. J. (1995). An objective assessment of analytical method precision: comparison of ICP-AES and XRF for the analysis of silicate rocks. *Chemical Geology* **124**, 1-19.
- Ratmeyer, V., Balzer, W., Bergametti, G., Chiapello, I., Fischer, G., and Wyputta, U. (1999a). Seasonal impact of mineral dust on deep-ocean particle flux in the eastern subtropical Atlantic Ocean. *Marine Geology* **159**, 241-252.
- Ratmeyer, V., Fischer, G., and Wefer, G. (1999b). Lithogenic particle fluxes and grain size distributions in the deep ocean off northwest Africa: Implications for seasonal changes of aeolian dust input and downward transport. *Deep Sea Research Part I: Oceanographic Research Papers* **46**, 1289-1337.
- Rea, D. K. (1994). The paleoclimatic record provided by eolian deposition in the deep sea: the geologic history of wind. *Reviews of Geophysics* **32**, 159-195.

- Renssen, H., Brovkin, V., Fichetef, T., and Goosse, H. (2003). Holocene climate instability during the termination of the African Humid Period. *Geophysical Research Letters* **30**, doi:10.1029/2002GL016636.
- Renssen, H., Brovkin, V., Fichetef, T., and Goosse, H. (2006). Simulation of the Holocene climate evolution in Northern Africa: The termination of the African Humid Period. *Quaternary International* **150**, 95-102.
- Richter, T. O., Van der Gaast, S., Koster, B., Vaars, A., Gieles, R., de Stigter, H. C., de Haas, H., and van Weering, T. C. E. (2006). The Avaatech Core Scanner: Technical description and applications to NE Atlantic sediments. In "New ways of looking at sediment core and core data." (R. G. Rothwell, Ed.), pp. 39-50. Geological Society Special Publication, London.
- Roucoux, K. H., de Abreu, L., Shackleton, N. J., and Tzedakis, P. C. (2005). The response of NW Iberian vegetation to North Atlantic climate oscillations during the last 65 kyr. *Quaternary Science Reviews* **24**, 1637-1653.
- Röhl, U., and Abrams, L. J. (2000). High-resolution, downhole, and nondestructive core measurements from Site 999 and 1001 in the Caribbean Sea: Application to the Late Paleocene Thermal Maximum. In "Proceedings of the Ocean Drilling Program, Scientific Results." pp. 191-203.
- Röhl, U., Ogg, J. G., Geib, T. L., and Wefer, G. (2001). Astronomical calibration of the Danian time scale. In "Western North Atlantic Paleogene and Cretaceous Paleooceanography." (R. D. Norris, D. Kroon, and A. Klaus, Eds.), pp. 163-183. Geological Society Special Publication. Geological Society, London.
- Ruddiman, W. F., and Raymo, M. E. (2003). A methane-based time scale for Vostok ice. *Quaternary Science Reviews* **22**, 141-155.
- Sánchez-Goni, M. F., Cacho, I., Turon, J. L., Guiot, J., Sierro, F. J., Peyrouquet, J. P., Grimalt, J. O., and Shackleton, N. J. (2002). Synchronicity between marine and terrestrial responses to millennial scale climatic variability during the last glacial period in the Mediterranean region. *Climate Dynamics* **19**, 95-105.
- Sarnthein, M., and Koopmann, B. (1980). Late Quaternary Deep-Sea Record on Northwest African dust supply and wind circulation. *Palaeoecology of Africa and the Surrounding Islands* **12**, 239-253.
- Sarnthein, M., Tetzlaff, G., Koopmann, B., Wolter, K., and Pflaumann, U. (1981). Glacial and interglacial wind regimes over the eastern subtropical Atlantic and North-West Africa. *Nature* **293**, 193-196.
- Schmidt, M. W., Vautravers, M. J., and Spero, H. J. (2006). Rapid subtropical North Atlantic salinity oscillations across Dansgaard-Oeschger cycles. *Nature* **443**, 561-564.
- Shackleton, N. J., Fairbanks, R. G., Chiu, T.-c., and Parrenin, F. (2004). Absolute calibration of the Greenland time scale: implications for Antarctic time scales and for $\Delta 14C$. *Quaternary Science Reviews* **23**, 1513-1522.
- Shackleton, N. J., Hall, M. A., and Vincent, E. (2000). Phase relationships between millennial-scale events 64,000-24,000 years ago. *Paleoceanography* **15**, 565-569.
- Siedler, G., and Onken, R. (1996). Eastern Recirculation. In "The warmwatersphere of the North Atlantic Ocean." (W. Krauss, Ed.), pp. 339-364. Gebrüder Bornträger, Berlin Stuttgart.
- Skinner, L. C., Shackleton, N. J., and Elderfield, H. (2003). Millennial-scale variability of deep-water temperature and $\delta^{18}O_{dw}$ indicating deep water source variations, 0-34 cal. ka BP. *Geochemistry, Geophysics, Geosystems* **4**, 1098, doi:10.1029/2003GC000585.
- Stabbel, B. (1989). Initial diatom record of sites 657 and 658: On the history of upwelling and continental aridity. In "Proceedings of the Ocean Drilling Program, Scientific Results." (W. Ruddiman, and M. Sarnthein, Eds.), pp. 149-156.

- Stein, R., ten Haven, H. L., Littke, R., Rullkötter, J., and Welte, D. H. (1989). Accumulation of marine and terrigenous organic carbon at upwelling site 658 and nonupwelling sites 657 and 659: Implications for the reconstruction of paleoenvironments in the eastern subtropical Atlantic through late Cenozoic times. *In* "Proceedings of the Ocean Drilling Program, Scientific Results." (W. Ruddiman, and M. Sarnthein, Eds.), pp. 241-261.
- Stocker, T., and Wright, D. G. (1991). Rapid transition of the ocean's deep circulation induced by changes in surface water fluxes. *Nature* **351**, 729-732.
- Stott, L., Poulsen, C., Lund, S., and Thunell, R. (2002). Super ENSO and Global Climate Oscillations at Millennial Time Scales. *Science* **297**, 222-226.
- Street-Perrott, F. A., and Perrott, R. A. (1990). Abrupt climate fluctuations in the tropics: the influence of Atlantic Ocean circulation. *Nature* **343**, 607-612.
- Stuut, J.-B. W., and Lamy, F. (2004). Climate variability at the southern boundaries of the Namib (southwestern Africa) and Atacama (northern Chile) coastal deserts during the last 120,000 yr. *Quaternary Research* **62**, 301-309.
- Stuut, J.-B. W., Prins, M. A., Schneider, R. R., Weltje, G. J., Jansen, J. H. F., and Postma, G. (2002). A 300-kyr record of aridity and wind strength in southwestern Africa: inferences from grain-size distributions of sediments on Walvis Ridge, SE Atlantic. *Marine Geology* **180**, 221-233.
- Stuut, J.-B. W., Zabel, M., Ratzmeyer, V., Helmke, P., Schefuß, E., Lavik, G., and Schneider, R. R. (2005). Provenance of present-day eolian dust collected off NW Africa. *Journal of Geophysical Research* **110**, doi:10.1029/2004JD005161
- Swap, R., Ulanski, S., Cobbett, M., and Garstang, M. (1996). Temporal and spatial characteristics of Saharan dust outbreaks. *Journal of Geophysical Research* **101**, 4205-4220.
- Tetzlaff, G., and Peters, M. (1986). Deep-sea sediments in the eastern equatorial Atlantic off the African coast and meteorological flow patterns over the Sahel. *Geologische Rundschau* **75**, 71-79.
- Tiedemann, R., Sarnthein, M., and Shackleton, N. J. (1994). Astronomic timescale for the Pliocene Atlantic $\delta^{18}\text{O}$ and dust flux records of Ocean Drilling Program site 659. *Paleoceanography* **9**, 619-638.
- Tiedemann, R., Sarnthein, M., and Stein, R. (1989). Climatic changes in the Western Sahara: Aeolo-marine sediment record of the last 8 million years (Sites 657-661). *In* "Proceedings of the Ocean Drilling Program, Scientific Results." (W. Ruddiman, and M. Sarnthein, Eds.), pp. 241-278.
- Timmermann, A., Krebs, U., Justino, F., Goosse, H., and Ivanochko, T. (2005). Mechanisms for millennial-scale global synchronization during the last glacial period. *Paleoceanography* **20**, PA4008, doi:10.1029/2004PA001090.
- Tjallingii, R., Röhl, U., Kölling, M., and Bickert, T. (2007). Influence of the water content on X-ray fluorescence core scanning measurements in soft marine sediments. *Geochemistry, Geophysics, Geosystems*. doi: 10.1029/2006GC001393.
- Turney, C. S. M., Kershaw, A. P., Clemens, S. C., Branch, N., Moss, P. T., and Keith Fifield, L. (2004). Millennial and orbital variations of El Niño/Southern Oscillation and high-latitude climate in the last glacial period. *Nature* **428**, 306-310.
- Tzedakis, P. C., Frogley, M. R., and Heaton, T. H. E. (2003). Last Interglacial conditions in southern Europe: evidence from Ioannina, northwest Greece. *Global and Planetary Change* **36**, 157-170.
- Vidal, L., Labeyrie, L., Cortijo, E., Arnold, M., Duplessy, J. C., Michel, E., Becque, S., and van Weering, T. C. E. (1997). Evidence for changes in the North Atlantic Deep Water linked to meltwater surges during the Heinrich events. *Earth and Planetary Science Letters* **146**, 13-27.

- Voelker, A. H. L. (2002). Global distribution of centennial-scale records for Marine Isotope Stage (MIS) 3: a database. *Quaternary Science Reviews* **21**, 1185-1212.
- Vörösmarty, C. J., Fekete, B. M., Maybeck, M., and Lammers, R. B. (2000). Global system of rivers: Its role in organizing continental land mass and defining land-to-ocean linkage. *Global Biogeochemical Cycles* **14**, 599-621.
- Waelbroeck, C., Labeyrie, L., Michel, E., Duplessy, J. C., McManus, J. F., Lambeck, K., Balbon, E., and Labracherie, M. (2002). Sea-level and deep water temperature changes derived from benthic foraminifera isotopic records. *Quaternary Science Reviews* **21**, 295-305.
- Weber, M. E., Niessen, F., Kuhn, G., and Wiedicke, M. (1997). Calibration and application of marine sedimentary physical properties using a multi-sensor core logger. *Marine Geology* **136**, 151-172.
- Wefer, G., and Fischer, G. (1993). Seasonal patterns of vertical particle flux in equatorial and coastal upwelling areas of the eastern Atlantic. *Deep Sea Research Part I: Oceanographic Research Papers* **40**, 1613-1645.
- Weltje, G. (1997). End-member modelling of compositional data: Numerical-statistical algorithms for solving the explicit mixing problem. *Journal of Mathematical Geology* **29**, 503-549.
- Weltje, G. J., and Prins, M. A. (2003). Muddled or mixed? Inferring palaeoclimate from size distributions of deep-sea clastics. *Sedimentary Geology* **162**, 39-62.
- Westerhold, T. (2003). "The Middle Miocene Carbonate Crash: Relation to Neogene Changes in Ocean Circulation and Global Climate." Dissertation Thesis, Universität Bremen, pp. 151.
- Westerhold, T., Bickert, T., and Röhl, U. (2005). Middle to late Miocene oxygen isotope stratigraphy of ODP site 1085 (SE Atlantic): new constraints on Miocene climate variability and sea-level fluctuations. *Palaeogeography, Palaeoclimatology, Palaeoecology* **217**, 205-222.
- Wien, K., Holz, C., Kölling, M., and Schulz, H. D. (2006). Age models for pelagites and turbidites from the Cap Timiris Canyon off Mauritania. *Marine and Petroleum Geology* **23**, 337-352.
- Wien, K., Wissmann, D., Kölling, M., and Schulz, H. D. (2005). Fast application of X-ray fluorescence spectrometry aboard ship: how good is the new portable Spectro Xepos analyzer. *Geo-Marine Letters* **25**, 248-264.
- Zhao, M., Beveridge, N. A. S., Shackleton, N. J., Sarnthein, M., and Eglinton, G. (1995). Molecular stratigraphy of cores off north-west Africa: Sea surface temperatures history over the last 80 ka. *Paleoceanography* **10**, 661-675.
- Zhao, M., Mercer, J. L., Eglinton, G., Higginson, M. J., and Huang, C.-Y. (2006). Comparative molecular biomarker assessment of phytoplankton paleoproductivity for the last 160 kyr off Cap Blanc, NW Africa. *Organic Geochemistry* **37**, 72-97.